

Universität  
Rostock



Traditio et Innovatio

# Analysis of the Role of Quantum Effects in Coherent Diffractive Imaging

Dissertation zur Erlangung des akademischen Grades  
*doctor rerum naturalium*  
der Mathematisch-Naturwissenschaftlichen Fakultät  
der Universität Rostock

vorgelegt von

Björn Thorben Kruse  
geb. am 29. Dezember 1991 in Kiel

Februar 2024

Betreuer: Prof. Dr. Thomas Fennel, Universität Rostock

Gutachter: Prof. Dr. Thomas Fennel, Universität Rostock  
Prof. Dr. Thomas Brabec, University of Ottawa

Eingereicht: 19.02.2024  
Verteidigung: 24.05.2024

# Abstract

Single-shot coherent diffractive imaging (CDI) has proven to be a successful tool for analyzing the structure of individual free nanoparticles and tracking their light-induced dynamics with exceptional spatial and temporal resolution. To reconstruct the shape and orientation of nanoparticles, CDI experiments have so far been analyzed in terms of a classical linear response description, neglecting nonlinear quantum effects. However, these effects are particularly important in the context of resonant excitation and high intensities. This is especially relevant for the recently successfully demonstrated CDI of isolated helium nanodroplets with a laboratory-based high-harmonic generation (HHG) source operating in the vicinity of the  $1s^2$ - $1s2p$  transition of helium.

In this work, a density matrix-based scattering model was developed in order to include such quantum effects in the local medium response and explore the transition from linear to nonlinear CDI for the scattering from Helium nanodroplets. It is found that even when only a single transition is included, the scattering patterns differ substantially from the linear response case for pulse parameters that are achievable at free-electron lasers or in HHG light sources.

As a next step in this approach, additional energy levels were incorporated in the model to study the implications of multiple transitions on the scattering patterns. The analysis begins by investigating the influence of additional non-resonant p-levels. The results show that including these states opens up new channels for population dynamics and leads to a reduced overall relevance of the previously solely considered  $1s^2$ - $1s2p$  resonance. Further, the previously unknown influence of transient energy levels shifts due to light-induced coupling by a long-wavelength pump laser is investigated. The associated change in the electromagnetic response has a substantial impact on the scattering pattern, highlighting the importance of considering quantum effects in the analysis of CDI experiments.



# Kurzzusammenfassung:

Die kohärente diffraktive Einzelschuss-Bildgebung (*Single-shot Coherent Diffractive Imaging*, CDI) hat sich als erfolgreiches Instrument zur Analyse der Struktur einzelner freier Nanopartikel und zur Verfolgung ihrer lichtinduzierten Dynamik mit außergewöhnlicher räumlicher und zeitlicher Auflösung erwiesen. Um die Form und Orientierung von Nanopartikeln zu rekonstruieren, wurden CDI-Experimente bisher anhand einer klassischen linearen Antwortbeschreibung analysiert, wobei nichtlineare Quanteneffekte vernachlässigt wurden. Diese Effekte sind jedoch im Zusammenhang mit resonanter Anregung und hohen Intensitäten besonders wichtig. Dies gilt insbesondere für die kürzlich erfolgreich demonstrierte Aufnahme von Streubildern von isolierten Helium-Nanotröpfchen mit einer laborgestützten Quelle für die Erzeugung hoher Harmonischer (HHG), die Licht mit Frequenzen in der Nähe des  $1s^2$ - $1s2p$  Übergangs von Helium erzeugt.

In dieser Arbeit wurde ein auf einer Dichtematrix basierendes Streumodell entwickelt, um solche Quanteneffekte in die lokale Medienantwort einzubeziehen und den Übergang von linearem zu nichtlinearem CDI für die Streuung von Helium-Nanotröpfchen zu untersuchen. Es wurde herausgefunden, dass selbst wenn nur ein einziger Übergang berücksichtigt wird, sich die Streubilder für Pulsparameter, die an Freie-Elektronen-Lasern oder in HHG-Lichtquellen erreichbar sind, erheblich von denen unterscheiden, bei denen eine lineare Materialantwort angenommen wird.

Als nächster Schritt in diesem Ansatz wurden zusätzliche Energieniveaus in das Modell einbezogen, um die Auswirkungen mehrerer Übergänge auf die Streubilder zu untersuchen. Zunächst wird der Einfluss zusätzlicher nicht-resonanter p-Niveaus auf die Streuung untersucht. Die Ergebnisse zeigen, dass die Berücksichtigung dieser Zustände neue Kanäle für die Populationsdynamik eröffnet und zu einer geringeren Gesamtrelevanz der bisher ausschließlich betrachteten  $1s^2$ - $1s2p$ -Resonanz führt. Des Weiteren wird der bisher unbekannte Einfluss von transienten Energieniveaushiftungen aufgrund von lichtinduzierter Kopplung durch einen langwelligen Pumplaser untersucht. Die damit verbundene Veränderung der elektromagnetischen Antwort hat einen erheblichen Einfluss auf das Streubild, was die Bedeutung der Berücksichtigung von Quanteneffekten bei der Analyse von CDI-Experimenten unterstreicht.



# List of Publications and Conference Proceedings

- [BK1] A. Mermillod-Blondin, P. Jürgens, B. Liewehr, [B. Kruse](#), C. Peltz, T. Witting, A. Husakou, M. Ivanov, T. Fennel and M. J. Vrakking, *Study of plasma formation in solid dielectrics with the help of low-order harmonic emission*, [Laser Applications in Microelectronic and Optoelectronic Manufacturing \(LAMOM\) XXIV](#) **10905**, 64–69 (2019).
- [BK2] [B. Kruse](#), B. Liewehr, C. Peltz and T. Fennel, *Quantum coherent diffractive imaging*, [Journal of Physics: Photonics](#) **2**, 024007 (2020).
- [BK3] P. Jürgens, B. Liewehr, [B. Kruse](#), C. Peltz, D. Engel, A. Husakou, T. Witting, M. Ivanov, M. Vrakking, T. Fennel et al., *Origin of strong-field-induced low-order harmonic generation in amorphous quartz*, [Nature Physics](#) **16**, 1035–1039 (2020).
- [BK4] A. Colombo, J. Zimmermann, B. Langbehn, T. Möller, C. Peltz, K. Sander, [B. Kruse](#), P. Tümmler, I. Barke, D. Rupp et al., *The Scatman: an approximate method for fast wide-angle scattering simulations*, [Journal of Applied Crystallography](#) **55**, (2022).
- [BK5] P. Jürgens, B. Liewehr, [B. Kruse](#), C. Peltz, T. Witting, A. Husakou, A. Rouzée, M. Ivanov, T. Fennel, M. J. J. Vrakking and A. Mermillod-Blondin, *Characterization of Laser-Induced Ionization Dynamics in Solid Dielectrics*, [ACS Photonics](#) **9**, 233–240 (2022).
- [BK6] P. Jürgens, B. Liewehr, [B. Kruse](#), C. Peltz, T. Witting, A. Husakou, A. Rouzée, M. Ivanov, T. Fennel, M. J. Vrakking et al., *Reconstruction of Strong-Field-Driven Carrier Generation Dynamics from Injection Harmonics in Solid Dielectrics*, , [Tu4A–14](#) (2022).
- [BK7] T. Paschen, R. Roussel, L. Seiffert, [B. Kruse](#), C. Heide, P. Dienstbier, J. Mann, J. Rosenzweig, T. Fennel and P. Hommelhoff, *Ultrafast Strong-Field Electron Emission and Collective Effects at a One-Dimensional Nanostructure*, [ACS Photonics](#) **10**, 447–455 (2023).

- [BK8] A. Colombo, S. Dold, P. Kolb, N. Bernhardt, P. Behrens, J. Correa, S. Düsterer, B. Erk, L. Hecht, A. Heilrath, R. Irsig, N. Iwe, J. Jordan, [B. Kruse](#), B. Langbehn, B. Manschwetus, F. Martinez, K.-H. Meiwes-Broer, K. Oldenburg, C. Passow, C. Peltz, M. Sauppe, F. Seel, R. M. P. Tanyag, R. Treusch, A. Ulmer, S. Walz, T. Fennel, I. Barke, T. Möller, B. von Issendorff and D. Rupp, *Three-dimensional femtosecond snapshots of isolated faceted nanostructures*, [Science Advances](#) **9**, (2023).
- [BK9] S. Dold, T. Reichenbach, A. Colombo, J. Jordan, I. Barke, P. Behrens, N. Bernhardt, J. Correa, S. Düsterer, B. Erk, T. Fennel, L. Hecht, A. Heilrath, R. Irsig, N. Iwe, P. Kolb, [B. Kruse](#), B. Langbehn, B. Manschwetus, P. Marienhagen, F. Martinez, K.-H. M. Broer, K. Oldenburg, C. Passow, C. Peltz, M. Sauppe, F. Seel, R. M. P. Tanyag, R. Treusch, A. Ulmer, S. Walz, M. Moseler, T. Möller, D. Rupp and B. von Issendorff, *Melting, bubble-like expansion and explosion of superheated plasmonic nanoparticles*, submitted and on arXiv: [arXiv:2309.00433](#), (2023).
- [BK10] A. Ulmer, A. Heilrath, B. Senfftleben, S. M. O’Connell-Lopez, [B. Kruse](#), L. Seiffert, K. Kolatzki, B. Langbehn, A. Hoffmann, T. M. Baumann, R. Boll, A. S. Chatterley, A. D. Fanis, B. Erk, S. Erukala, A. J. Feinberg, T. Fennel, P. Grychtol, R. Hartmann, M. Ilchen, M. Izquierdo, B. Krebs, M. Kuster, T. Mazza, J. Montaña, G. Noffz, D. E. Rivas, D. Schlosser, F. Seel, H. Stapelfeldt, L. Strüder, J. Tiggesbäumker, H. Yousef, M. Zabel, P. Ziolkowski, M. Meyer, Y. Ovcharenko, A. F. Vilesov, T. Möller, D. Rupp and R. M. P. Tanyag, *Generation of Large Vortex-Free Superfluid Helium Nanodroplets*, [Physical Review Letters](#) **131**, 076002 (2023).

# List of Presentations

## Talks:

- 28.02.2017 Graduate School Workshop, Güstrow  
*Signatures of Rabi cycling and excited state population in single-shot coherent diffractive imaging*
- 09.03.2017 DPG Spring Meeting (SAMOP), Mainz  
*Signatures of Rabi cycling and excited state population in single-shot coherent diffractive imaging*
- 04.01.2018 Graduate School Seminar, Rostock  
*Signatures of Rabi cycling and excited state population in single-shot coherent diffractive imaging*
- 06.03.2018 DPG Spring Meeting (SAMOP), Erlangen  
*Signatures of Rabi cycling and excited state population dynamics in single-shot coherent diffractive imaging*
- 16.06.2019 Gordon Research Seminar on Clusters and Nanostructures, Les Diablerets  
*Coherent diffractive imaging of population dynamics in a helium droplet*
- 30.07.2020 Cappuscienza (Group Seminar AG Rupp), Zürich (digital)  
*Quantum Coherent Diffractive Imaging*
- 20.01.2021 NEISS Research Seminar, Rostock  
*Quantum Coherent Diffractive Imaging*
- 04.08.2021 NEISS Status Seminar, Rostock  
*Partial contribution to Work package 1: Strukturen und Symmetrien in Zustandsräumen*
- 20.10.2021 Symposium on Optics & its applications 2021, Rostock  
*Quantum Coherent Diffractive Imaging*
- 16.03.2022 DPG Spring Meeting (SAMOP), Erlangen (digital)  
*Influence of multiple transitions for Quantum Coherent Diffractive imaging*

- 04.10.2022 Clustertreffen, Feldberg  
*Influence of multiple transitions for Quantum Coherent Diffractive imaging*
- 23.08.2022 NEISS Final Seminar, Rostock  
*Partial contribution to Work package 1: Strukturen und Symmetrien in Zustandsräumen*

**Posters:**

8. - 13.05.2016 WE-Heraeus Workshop: Ultrafast Phenomena at Nanostructures, Les Houches  
*FDTD calculations of near and far fields of laser-driven nanostructures*
- 26.08.2016 Workshop Ultrafast Cluster Dynamics, Berlin  
*Classical and quantum mechanical description of single-shot diffractive imaging*
- 16.06.2017 SFB 652 Abschlusskolloquium, Rostock  
*Controlling the plasma formation in clusters by seeded avalanching*
- 26.09.2017 Clustertreffen, Bacharach  
*Signatures of Rabi cycling in single-shot coherent diffractive imaging*
- 20.02.2018 Graduate School Workshop, Güstrow  
*Controlling the plasma formation in clusters by seeded avalanching*
04. - 07.12.2018 QUTIF Young Researcher Meeting 2018, Berlin  
*Coherent diffractive imaging of population dynamics in a helium droplet*
- 02.09.2019 Dynamic Days, Rostock  
*Coherent diffractive imaging of population dynamics in a helium droplet*
- 13.03.2019 DPG Spring Meeting (SAMOP), Rostock  
*Coherent diffractive imaging of population dynamics in a helium droplet*
16. - 21.06.2019 Gordon Research Conference on Clusters and Nanostructures , Les Diablerets  
*Coherent diffractive imaging of population dynamics in a helium droplet*
- 27.09.2019 Praktikumsleitertagung, Rostock  
*Research Lab Course: Light Propagation in Dielectric Materials*
- 21.09.2021 DPG Autumn Meeting (SAMOP), digital  
*Quantum Coherent Diffractive Imaging*
02. - 07.10.2022 Clustertreffen, Feldberg  
*Influence of multiple transitions for Quantum Coherent Diffractive imaging*
- 23.08.2022 NEISS Closing Seminar, Rostock  
*Digital Poster presentation together with Paul Tümmler: Unterstützung von Strahlzeiten an FELs*



# Contents

<b>List of Publications and Conference Proceedings</b>	<b>vii</b>
<b>List of Presentations</b>	<b>ix</b>
<b>List of Figures</b>	<b>xvii</b>
<b>List of Tables</b>	<b>xix</b>
<b>1. Introduction</b>	<b>1</b>
1.1. Single-shot CDI - scattering regimes and modeling/reconstruction . . . . .	2
1.2. Bound Atomic States in intense fields . . . . .	6
1.2.1. Additional spectral features . . . . .	7
1.2.2. Shift of spectral lines: Stark effect . . . . .	8
1.3. Goal and Structure of the thesis . . . . .	9
<b>2. Methods - Few-level Density Matrix Finite Difference Time Domain</b>	<b>11</b>
2.1. Propagation of electromagnetic fields - the FDTD method . . . . .	11
2.1.1. Field discretization . . . . .	12
2.1.2. Absorbing boundary conditions and field source . . . . .	14
2.2. Material response . . . . .	16
2.2.1. Linear polarization . . . . .	16
2.2.2. Nonlinear bound electron dynamics . . . . .	18
2.2.3. Few level system, usage and weak-field limit . . . . .	24
2.3. Near field to far field transformation . . . . .	27
2.4. Numerical implementation . . . . .	29
<b>3. Quantum Coherent Diffractive Imaging - Single Active Transition</b>	<b>31</b>
3.1. Simulation setup and linear response benchmark . . . . .	31
3.2. Population dynamics and electric fields for nonlinear excitation . . . . .	36
3.3. Nonlinear QCDI . . . . .	38
3.3.1. Saturation . . . . .	40
3.3.2. Change of fringe spacing . . . . .	40
3.3.3. Blurring of ring structure . . . . .	40
<b>4. Quantum Coherent Diffractive Imaging - Multiple Active Transitions</b>	<b>45</b>
4.1. Stability analysis of the FLDM FDTD implementation . . . . .	45
4.1.1. Instability example from full calculations . . . . .	45
4.1.2. Analytical stability analysis . . . . .	48

4.1.3. Circumventing the instabilities - 2 physically relevant scenarios . . .	53
4.2. Influence of multiple transitions for Quantum Coherent Diffractive Imaging	55
4.2.1. Implications of additional p-levels (Scenario 1: Strong XUV pulse)	56
4.2.2. Transient modification of optical parameters by an NIR pulse (Scenario 2: Weak XUV pulse, Strong NIR pulse) . . . . .	59
4.3. Omitted effects . . . . .	65
<b>5. Origin of Strong-Field Induced Low-Order Harmonic Generation in Amorphous Solids</b>	<b>67</b>
5.1. Harmonic generation in solids . . . . .	67
5.2. Time-resolved measurement of low-order two-color harmonics . . . . .	69
5.3. Identification of the injection current as the dominant wave-mixing process	74
5.3.1. Effective order of nonlinearity . . . . .	74
5.3.2. Ionization induced nonlinearity . . . . .	76
5.4. Conclusion . . . . .	79
<b>6. Temporal Control of Cluster Ionization in Strong Fields</b>	<b>81</b>
6.1. Atomic clusters in strong fields . . . . .	81
6.2. Methods . . . . .	83
6.2.1. Experimental setup . . . . .	83
6.2.2. Semiclassical molecular dynamics simulations . . . . .	83
6.3. Temporal control of NIR cluster ionization . . . . .	85
6.4. Influence of atom mass, ionization potential and laser polarization on electron impact avalanching . . . . .	89
6.5. Conclusion . . . . .	92
<b>7. Conclusions and Outlook</b>	<b>93</b>
<b>Appendix</b>	<b>97</b>
A. Definition: Fourier transformation . . . . .	97
B. Derivation of the EOM for the expectation value of the dipole moment of a two-level system . . . . .	98
C. Detailed derivation of the near field to far field transformation . . . . .	100
C.1. Field continuity relations for currents and magnetization on a surface	100
C.2. Equivalent source theorem . . . . .	103
C.3. Fields from electric and magnetic sources . . . . .	104
C.4. Evaluation of the far field . . . . .	108
D. Additional calculation for the magnetization-based vector potential . . .	111
E. Atomic polarizability vs. susceptibility . . . . .	112
<b>Bibliography</b>	<b>113</b>
<b>Academic Curriculum Vitae</b>	<b>127</b>
<b>Statement of Authorship</b>	<b>129</b>

Acknowledgement – Danksagung

133



# List of Figures

1.1. Basic CDI setup . . . . .	2
1.2. Small and large angle scattering . . . . .	3
1.3. ATAS example . . . . .	6
1.4. Sketch: LIS . . . . .	7
1.5. Sketch: FWM . . . . .	7
1.6. Sketch: DC Stark effect (linear) . . . . .	8
1.7. Sketch: DC Stark effect (quadratic) . . . . .	8
1.8. Sketch: over-resonant (ponderomotive) . . . . .	8
1.9. Sketch: Autler-Townes splitting . . . . .	9
2.1. Yee grid . . . . .	14
2.2. Minimalistic sketch of equivalent source theorem . . . . .	27
3.1. Schematic sketch 2(4)LS . . . . .	32
3.2. Sketch 1s-2p Resonance in Helium . . . . .	33
3.3. Sketch scattering setup and benchmark 2LS . . . . .	35
3.4. Population and polarization dynamics 2LS . . . . .	37
3.5. Scattering patterns Intensity dependence . . . . .	39
3.6. Scattering intensity in Born approximation . . . . .	41
3.7. Spectra of electric field inside the Helium nanodroplet and the incident field and the resulting absorption peak . . . . .	43
3.8. Asymmetry of Rabi satellites for detuned excitation . . . . .	44
4.1. Instability example . . . . .	47
4.2. Local and global field sketch . . . . .	49

4.3. Population and scattering for additional p-levels . . . . .	56
4.4. Effective refractive index from ATAS . . . . .	60
4.5. Simulated intensity dependent effective refractive index . . . . .	61
4.6. Transiently modified scattering patterns . . . . .	62
4.7. Total scattering intensity . . . . .	63
4.8. Effect of effective refractive index on scattering patterns . . . . .	64
5.1. Schematic description and sketch of harmonic generation in solids . . . . .	68
5.2. Experimental setup: Time-resolved measurement of low-order two-color harmonics . . . . .	69
5.3. Delay-dependent harmonic spectrum . . . . .	70
5.4. Temporal signature of the harmonics . . . . .	71
5.5. Plasma diagnostics . . . . .	72
5.6. Experiments in crystalline quartz (c-SiO <sub>2</sub> ) . . . . .	73
5.7. Characterization of the effective nonlinearity $m$ underlying the harmonic emission (for the order $n=1$ ) as a function of the pump intensity in a-SiO <sub>2</sub> . . . . .	75
5.8. Effective nonlinearity as function of the bandgap . . . . .	79
6.1. Measured delay dependent charge state distributions of Xe Clusters . . . . .	86
6.2. Simulated delay dependent charge state distributions of Xe Clusters . . . . .	88
6.3. Simulated inner ionization for Ar and Xe Clusters . . . . .	89
6.4. Polarization dependence of Ar Cluster ionization . . . . .	91
C.1. Sketch of surface current integration . . . . .	101
C.2. Sketch of equivalent source theorem . . . . .	103

# List of Tables

4.1. Stable and unstable cases for the FLDM-FDTD model. . . . .	52
4.2. Helium transitions . . . . .	55



# 1. Introduction

A firm understanding of the chemical and physical properties of nanoparticles requires the detailed knowledge of their microscopic structure and shape. A striking example for this logic goes back to about 1953, when Rosalinde Franklin and Raymond Gosling [1] recorded X-ray diffraction patterns of DNA molecules deposited on a substrate, revealing its double helix structure consisting of basis pairs, which was vital for revealing biological information storage [2]. To explore biologically or medically relevant targets, like viruses, bacteria or molecules, singular isolated targets with spatial dimensions down to nanometers and dynamics taking place on the order of a few hundred attoseconds have to be investigated in free flight to avoid interaction with their surroundings.

The imaging method for recording diffraction patterns of single particles could with a single short and intense laser pulse is called 'single-shot coherent diffractive imaging' (CDI). The prerequisites to provide such pulses were met through the development of free electron lasers [3, 4, 5, 6, 7, 8]. The current long-term goal is to achieve atomic spatial and ultrashort temporal resolution in order to study both the structure and the function of molecules and thus to record a 'molecular movie' [9]. On the way there, many fundamental questions still have to be clarified and experimental methods need to be optimized. The imaging process itself requires ultra-short and intense short-wavelength laser pulses to ensure sufficient temporal and spatial resolution, as well as enough detector signal. Importantly, the pulse being very short is essential to image the target before it is inevitably destroyed (*diffraction before destruction* [10, 11]), enabling for example X-ray crystallography on a single-shot and single-crystal basis [12]. However, even for very short pulses, transient modifications can even happen on the femtosecond timescale, such that the scattering images contain information on the transient modification of the electronic structure by the developing nanoplasma [13, 14].

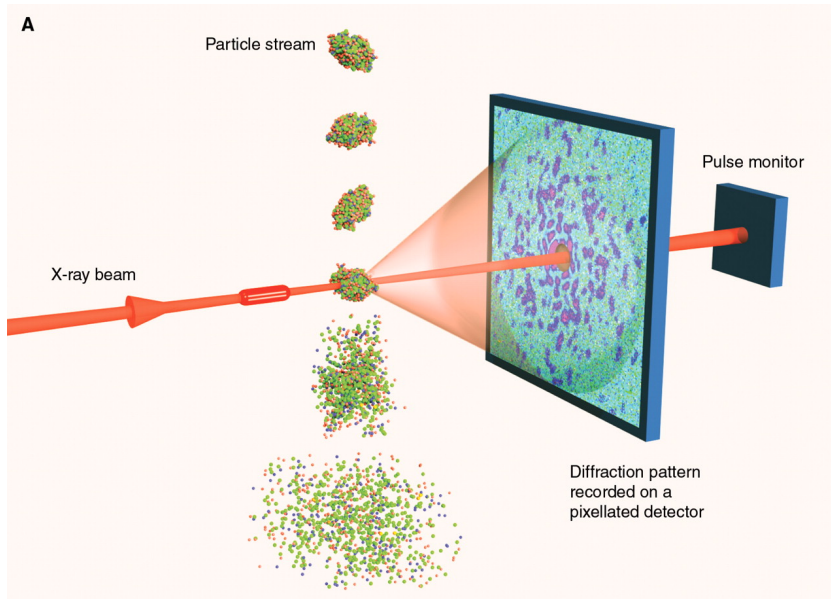


**Figure 1.1.:** Basic setting of a single-shot coherent diffractive imaging setup. The particle beam overlaps with the FEL beam from which the scattered light is recorded on a detector. From [10]

Figure 1.1 shows the basic setup of a CDI experiment, where a single FEL shot hits a single particle and its scattering pattern is recorded on a detector. The interpretation of the recorded scattering images, i.e. the linking of the observed scattering image with the properties of the scattering object, is generally still a highly complex task.

## 1.1. Single-shot CDI - scattering regimes and modeling/reconstruction

The crucial point for deciding what is observed structurally in the scattering image is the wavelength of the incident light. Typically, a distinction is made between two scattering regimes: small-angle and wide-angle scattering.

The resolution of scattering images is limited by the minimal distance that can be resolved by the light within the scattering object. This diffraction limit is described by the Abbe limit [15]

$$d = \frac{\lambda}{2n \sin \alpha} \quad (1.1)$$

which connects the minimal resolvable distance  $d$  to the refractive index  $n$ , the wavelength  $\lambda$  and the angle of incidence  $\alpha$ . Consequently, for optimal spatial resolution of the diffraction image, short wavelengths (high photon energies) pulses are required. This leads to the **small-angle** scattering regime, because at high photon energies, the scattering image containing the structural information of the nanoparticle is confined to a

small angular range. This is due to the fact that the scattered intensity drops with  $\propto q^{-4}$  (Porod's law [16]), where the momentum transfer  $q$  is dependent of the wavelength  $\lambda$  and the scattering angle  $\theta$ :

$$q = \frac{4\pi}{\lambda} \sin(\theta/2). \quad (1.2)$$

Due to the high photon energies, absorption and refraction of the incident light are very small, such that the scattering problem can be described in first Born approximation, which does not account for multiple scattered photons. In this case, the scattering image shows a Fourier transformation of the projected density of the target (Fig. 1.2 (a)), which is obtainable via inverse Fourier transformation.

To recover the phase of the scattered light that is lost when using standard detection methods, well-established iterative phase retrieval algorithms can be used to reconstruct the phase of the scattering image [17, 18, 19, 20]. This method was used for example to characterize the shape of the mimivirus [21] or to observe quantum vortices in spinning superfluid helium nanodroplets [22, 23, BK10]. Another elegant solution is the use of a reproducible reference scatterer to overcome the phase problem via holography [24]. To obtain the complete structural information of the scattering target, reproducible targets would have to be imaged randomly oriented in space and the obtained projections in Fourier space would have to be reassembled. Without reproducible targets or for rare events, this ansatz would not even work.

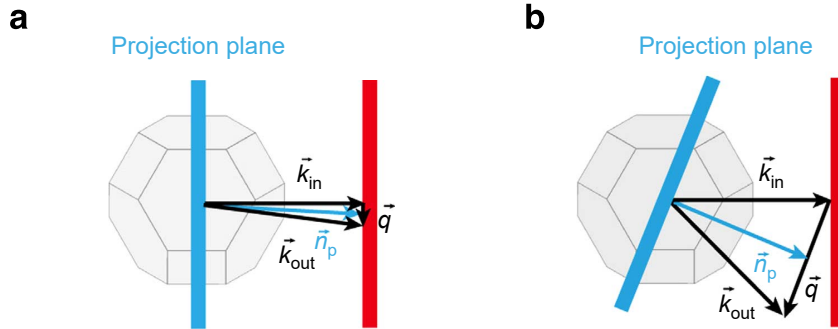


**Figure 1.2.:** In the small-angle scattering regime (a), the momentum transfer  $\mathbf{q} = \mathbf{k}_{\text{out}} - \mathbf{k}_{\text{in}}$ , where the  $\mathbf{k}$ -vectors indicate the outgoing and incident wave vectors, is nearly perpendicular to the incident beam, such that the resulting scattering image only depends on the 2D projection of the particle density (projection plane indicated by the blue bar). For large scattering angles (b), projection planes that are not perpendicular to the incident beam, contribute to the scattering images, which is then influenced by orientation dependent 3D properties of the particle. From [25]

To characterize non-reproducible targets [26], the major advantage of **wide-angle** scattering can be exploited. Using lower photon energies (XUV or soft X-Rays), larger scattering angles are observable in the scattering image. For larger scattering angles, the projection plane of the density is no longer parallel to the moment transfer, mean-

ing that the total image contains scattering signal from multiple projection planes (c.f. Fig. 1.2 (b), for a detailed derivation see [25]). Consequently, valuable information on the three-dimensional structure of the scattering target is imprinted in a single shot. For these wide-angle scattering images, the interpretation of the results of phase retrieval methods is more challenging. Those algorithms provide the exit field of the scattering object and for wide-angle scattering images, they are in fact not trivially connected to the projected density of the scatterer [20, BK4, BK9]. Moreover, absorption and refraction can not be neglected in this wavelength regime.

To take these changes into account, forward calculations have to be performed. To draw conclusions about the scattering nanoparticle, the scattering image of an imaginable candidate has to be calculated and compared to the original image. For spherical particles, Mie theory [27] provides a fast and analytical solution. For non-spherical targets, discrete dipole approximation (DDA [28] or complex scaling DDA [29]) or finite difference time domain (FDTD [30]) are more advanced, but computationally more demanding methods. Recently, more efficient analyses have been made possible by the use of deep neural networks [31] or forward-fitting optimization [BK8] using the multi slice fourier transform method [BK4]. In all these methods, the classical single particle scattering process is typically modeled in linear response.

Small-angle CDI using hard X-rays for maximum spatial resolution is expected to be dominated by XFELs, but nowadays, laboratory based light-sources have become bright enough to provide high-intensity, short wavelength XUV radiation to perform CDI. With a tabletop high-harmonic generation (HHG) source [32] single-shot CDI on Helium nanodroplets was performed, making the method generally more accessible and enhancing the method of CDI by the excellent temporal control of optical laser systems and flexible multi-color scenarios, where the optical properties of the targets could be characterized on a single-shot basis. Even though the HHG source has an intensity two orders of magnitude below a FEL, scattering patterns could be recorded because the imaging pulse contained photon energies close to the  $1s^2$ - $1s2p$  resonance of Helium, where the electronic response is very strong. Near atomic resonances, the excitation with a strong laser field can lead to population transfer and depletion can no longer be neglected. In the context of CDI however, the implications of Rabi-cycling [33, 34], stimulated emission or induced transparency [35] are so far unknown.

To study those effects, the analysis based on classical scattering using a linear medium response is no longer valid. Nonlinear phenomena and transient changes in the optical response caused by ionization have been incorporated before, for instance, by introducing an effective reduction in atomic form factors due to damage [36], or by employing explicit classical models to describe the ensuing microscopic plasma motion [37]. Recent investigations into the possibilities of incoherent scattering through fluorescence and Compton scattering [38, 39], as well as the study of super-fluorescence in the saturation phase [40], suggest that there is promise in investigating quantum effects within the context of CDI scenarios.

A thorough understanding of the impact of spatiotemporal coherent bound-state dynamics is of paramount importance to, on the one hand validate the applicability of established CDI reconstruction methods employing linear scattering and on the other hand to identify scenarios that enable the monitoring of associated nonlinear processes, including the prospect of tracking spatiotemporal excitation transport in extended quantum systems. This not only involves the response of the imaging XUV pulse though. In the context of attosecond transient absorption spectroscopy (ATAS), previous studies on Helium have shown transient modifications of the electronic response from an additional infrared (IR) pump pulse [41, 42], which are consequently expected to change the scattering significantly.

## 1.2. Bound Atomic States in intense fields

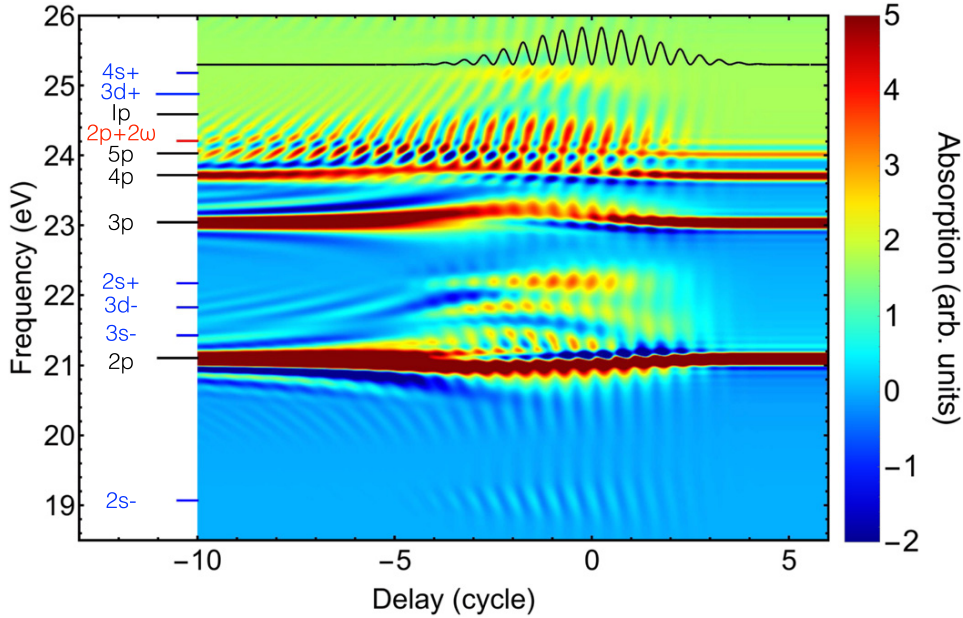


**Figure 1.3.:** Typical delay-dependent ATA spectrum which was calculated for helium with an intense attosecond XUV pulse (photon energy of 25 eV) and a NIR pulse (Intensity  $I = 3 \text{ TW/cm}^2$  and wavelength  $\lambda = 800 \text{ nm}$ ; instantaneous intensity indicated as a black line at the top) modifying XUV absorption. Negative delays correspond to the XUV coming before the NIR. On the left, states with dipole allowed transitions from the ground state are indicated in black, transitions involving NIR photons in blue ( $\pm 1$  NIR photon) and red ( $+ 2$  NIR photons). From [42]

The transient modification of bound atomic states by strong laser fields has been studied by the method of attosecond transient absorption spectroscopy [42], where the absorption of a sub-femtosecond XUV pulse is measured as function of delay to a long near-IR (NIR) pulse, enabling the precise study of the light-matter interaction of the two-color photons. Even though transient bound state dynamics like for example Rabi-cycling could be measured before on atomic targets by the detection of the Mollow-Triplet [43, 44, 45, 46, 47], ATAS allows for investigation with unprecedented temporal precision [48, 49].

In a typical calculated absorption spectrum in Fig. 1.3 we observe for both large negative and positive delays (i.e. XUV only), that the dipole allowed transitions from the ground state show distinct spectral lines. When the NIR pulse is overlapping with the XUV, pronounced new signatures occur. The spectral lines shift, new spectral lines appear and we notice sub-cycle modulation on the order of a few femtoseconds. The most common modifications to absorption spectrum in the presence of another intense field stem from light-induced states, four-wave mixing and from the Stark effect (in all its forms). The following is a brief overview of all these features.

### 1.2.1. Additional spectral features

**Light-induced state:** Light-induced structures are associated with two-photon processes that transfer the population from the ground state to the nondipole coupled ('dark') s and d states [50]. As the transition using a single XUV photon is forbidden, an additional NIR photon is absorbed or emitted in this process, leading to additional lines in the spectrum (c.f.  $2s_{\pm}$  on the left side in Fig. 1.3 for the transition from the groundstate to the 2s state with the emission/absorption of an NIR photon). These virtual intermediate states are then called light-induced states (LIS).

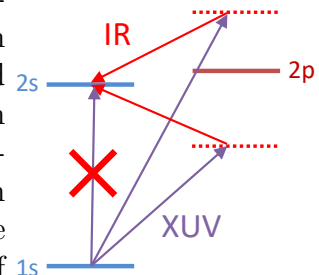


Figure 1.4.: LIS

**Four-wave mixing:** Nonlinear coupling can lead to the emission and absorption of additional frequencies [51]. In the case of four-wave mixing, a fourth frequency photon is generated by sum or difference frequency generation. The incident frequencies can contribute multiple times, leading to degenerate four-wave mixing. In the case of XUV and NIR ATAS, the XUV photon can, for example, be absorbed in a dipole allowed transition and two subsequent NIR photons either be absorbed or emitted, yielding spectral line two NIR photon energies away from the initial spectral feature (c.f. dotted violet lines in sketch 1.5 and  $2p+2\omega$  on the left side in Fig. 1.3).

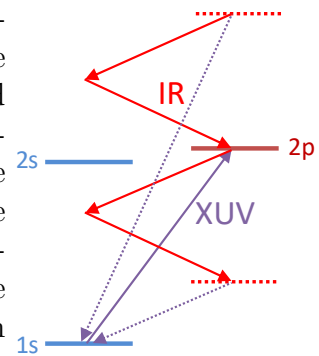
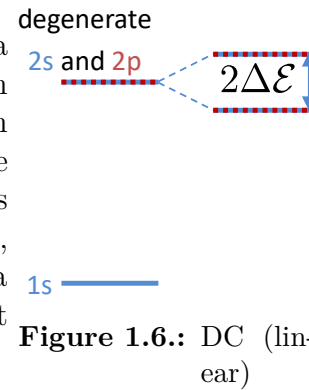


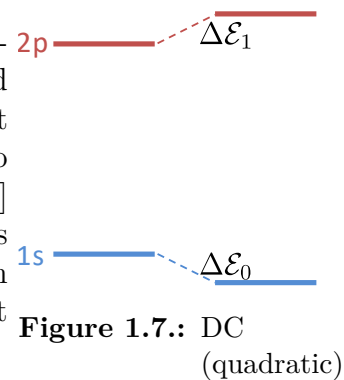
Figure 1.5.: FWM

### 1.2.2. Shift of spectral lines: Stark effect

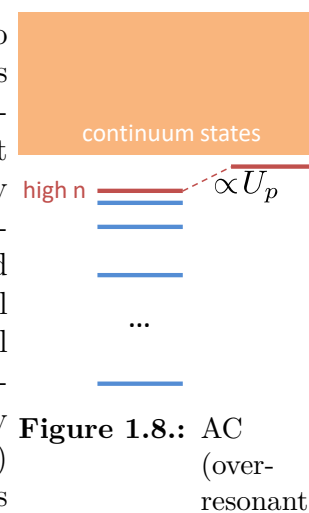
**DC Stark effect (linear):** If atoms or molecules have a permanent electric dipole moment, energy levels split in an applied constant electric field (DC), analogous to the Zeeman effect in the magnetic field [52, 53]. It occurs for degenerate atomic states, e.g. in hydrogen [54] and hydrogen like atoms such as  $\text{He}^+$ ,  $\text{Li}^{2+}$  or  $\text{Be}^{3+}$ . It can also occur in molecules, where the states are very close together [55, Ch. 2] or have a permanent electric dipole moment [56, Ch. 10.3.2]. This shift in a DC field is linear to the applied electric field strength.



**DC Stark effect (quadratic):** In systems without a permanent electric dipole moment, a strong applied electric field can induce a dipole moment which then leads to a Stark shift [56, Ch. 10.3.2][57]. The corresponding shift is quadratic to the applied field. It was measured in Rydberg atoms [58] where the large distance of the electron to the core enables very large induced electric dipole moments. More common however is the shift in a long-wavelength laser field (see next point, under-resonant AC Stark effect).



**Off-resonant AC Stark effect (quadratic):** The Stark effect in an alternating electric field (AC) can be divided into three cases, i.e. where the frequency of the applied field is (i) nearly resonant, (ii) far under-resonant or (iii) far over-resonant to the atomic resonance [59]. In the under-resonant case, the atomic states follow the laser field adiabatically and the level shift is equal to the quadratic DC Stark effect (c.f. sketch 1.7). In the case where the electric field oscillates faster than the resonance frequency, the additional energy to the bound electron is its ponderomotive potential  $U_p$  [60, 61] (comparable to a free electron in an oscillating electric field). This ponderomotive effect happens predominantly for weakly bound electrons (high principle quantum number) and decreases for stronger bound states. The energy shift is quadratically proportional to the electric field strength.



**Resonant AC Stark effect (linear, Autler-Townes splitting):**

If the electric field is (nearly) resonant to the atomic transition, Rabi-cycling between the two states will occur. Therefore, the involved states are dressed to the electric field [62] [51, Ch. 6.5] and split up into two levels each, linearly proportional to the electric field amplitude and the Rabi frequency  $\Omega$  (Autler-Townes effect [33]) leading to a the so-called Mollow-Triplet [34] in the spectrum, where the spectral line is accompanied by two satellites, separated by the Rabi-frequency.

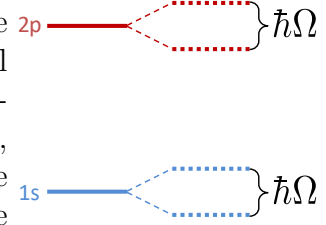


**Figure 1.9.:** AC (resonant)

### 1.3. Goal and Structure of the thesis

The existence and significance of light-induced states and Stark shifts are well known for atoms. The goal of this thesis is to investigate the implications and the associated signatures of spatiotemporal coherent bound-state electron dynamics in extended finite systems for wide-angle single-shot coherent diffractive imaging where their impact is so far unclear. However, it is of major importance to know when the established CDI reconstruction methods based on linear scattering are applicable and when they fail. Since today's HHG light sources (and naturally FELs) already reach high enough intensities with photon energies near bound-state transitions, it is an open question if and how potential nonlinear processes manifest itself in scattering images.

To this end, a consistent semi-classical model for the electromagnetic field propagation in conjunction with quantum coherent bound state dynamics was developed. Maxwell's equations are solved in time domain and the quantum mechanical local polarization response is incorporated using a few-level density matrix model. Therefore, the chapters of this work are structured as follows.

Chapter 2 describes the semi-classical scattering model including propagation via the finite difference time domain (FDTD) method and evaluation of the far-field using the method of equivalent sources. Moreover, the theoretical framework of the few-level density matrix (FLDM) model and its derivation is discussed in detail.

Chapter 3 presents the influence of nonlinear bound-state electron dynamics on CDI of helium nanodroplets and its substantial changes compared to linear CDI. An analysis on the influence of population dynamics on resonant scattering when just incorporating two bound states is provided, demonstrating substantial differences in the scattering patterns, which opens up the way for quantum coherent diffractive imaging.

The implications of additional levels is discussed in chapter 4. First, the Numerical (in)stability of the FLDM-FDTD model is analyzed in section 4.1, discussing possible ways to ensure stability. Two physically relevant scenarios are developed to circumvent the previously discussed instability.

In the first scenario (section 4.2.1) the previous resonant scattering scenario is extended

by two additional p-levels, which enables a subsequent absorption of the nonlinearly scattered light.

The second scenario (section 4.2.2) further extends the FLDM by many more levels and investigates the NIR pulse induced transient modifications of the optical parameters of liquid helium by probing its properties with a weak XUV pulse via CDI.

In addition to the development of the FLDM-FDTD model and its applications, further research on strong and short light-matter interaction was done in my doctoral period, which is not linked directly to nonlinear coherent diffractive imaging, but nevertheless deals with strong-field light-matter interaction.

Chapter 5 presents the main findings of a study on the origin of strong-field induced low order harmonic generation in bulk SiO<sub>2</sub>. With the model of the local nonlinear strong-field ionization response, it was shown, that the injection current, which appears when electrons are promoted to the conduction band, is the dominant contribution to low-order harmonics over conventional Kerr-type four-wave mixing or Brunel-type harmonic generation. The simulations supported the experimentally measured harmonic yields and allowed the convenient determination of the effective nonlinearity as a function of incident intensity.

In chapter 6, the results of NIR pump and XUV probe measurements on rare-gas (i.e. Xenon and Argon) clusters are presented, which yielded time dependent charge state distributions of the ionized clusters. With the help of molecular dynamics calculations, measured delay-dependent ion charge distributions were investigated, allowing to control the ionization by igniting the ionization by a moderately intense XUV pulse at well-defined times during the NIR pulse.

## 2. Methods - Few-level Density Matrix Finite Difference Time Domain

To model the light matter interaction at the nanometer scale with NIR to XUV light, the description of the light propagation and the material properties is required. The technique of choice to solve Maxwell's equations on a grid is the finite difference time domain (FDTD) algorithm [63], which will be described in section 2.1. The material properties resulting from bound-electron dynamics are described linearly by the classical Drude-Lorentz model (subsection 2.2.1) and nonlinearly by a quantum-mechanical few-level description (subsection 2.2.2). To arrive at scattering images, a near field to far field transformation which allows to easily evaluate the far field by using only free-space propagators will be used (see section 2.3).

### 2.1. Propagation of electromagnetic fields - the FDTD method

The basis of our semi-classical scattering model is the explicit propagation of Maxwell's macroscopic curl equations (i.e. considering the averaging over microscopic scales, for both matter and fields) in the absence of free charges and for non-magnetic materials

$$\nabla \times \mathbf{E} = -\dot{\mathbf{B}} \quad (2.1)$$

$$\nabla \times \mathbf{B} = \mu_0 (\mathbf{j} + \varepsilon_0 \dot{\mathbf{E}}), \quad (2.2)$$

with the spatially averaged electric field  $\mathbf{E}$  and magnetic field  $\mathbf{B}$  (continuum picture), the vacuum permeability  $\mu_0$  and permittivity  $\varepsilon_0$  as well as the electric current density  $\mathbf{j} = \dot{\mathbf{P}}$  which is the temporal derivative of the polarization (or dipole density)  $\mathbf{P} = n_0 \mathbf{d}$  with  $\mathbf{d}$  being the electric dipole moment and  $n_0$  the dipole number density. The polarization has to be propagated self-consistently with the fields and contains the full medium response (discussed in section 2.2), being only non-zero inside the material. The FDTD method is then employed to propagate Maxwell's equations in 3D self-consistently along with the solution of the electronic polarization response.

### 2.1.1. Field discretization

Maxwell's curl equations form a system of six coupled first order differential equations

$$\frac{\partial B_x}{\partial t} = \left[ \frac{\partial E_y}{\partial z} - \frac{\partial E_z}{\partial y} \right] \quad (2.3)$$

$$\frac{\partial B_y}{\partial t} = \left[ \frac{\partial E_z}{\partial x} - \frac{\partial E_x}{\partial z} \right] \quad (2.4)$$

$$\frac{\partial B_z}{\partial t} = \left[ \frac{\partial E_x}{\partial y} - \frac{\partial E_y}{\partial x} \right] \quad (2.5)$$

$$\frac{\partial E_x}{\partial t} = \frac{1}{\varepsilon_0 \mu_0} \left[ \frac{\partial B_z}{\partial y} - \frac{\partial B_y}{\partial z} \right] - \frac{1}{\varepsilon_0} j_x \quad (2.6)$$

$$\frac{\partial E_y}{\partial t} = \frac{1}{\varepsilon_0 \mu_0} \left[ \frac{\partial B_x}{\partial z} - \frac{\partial B_z}{\partial x} \right] - \frac{1}{\varepsilon_0} j_y \quad (2.7)$$

$$\frac{\partial E_z}{\partial t} = \frac{1}{\varepsilon_0 \mu_0} \left[ \frac{\partial B_y}{\partial x} - \frac{\partial B_x}{\partial y} \right] - \frac{1}{\varepsilon_0} j_z. \quad (2.8)$$

The basic idea to solve these equations self-consistently was proposed by Kane Yee in 1966 [30]. It is based on a spatiotemporal staggering of electric and magnetic field components such that their position in space and time matches the central finite differences for the spatial and temporal derivatives. The resulting grid is sketched in Fig. 2.1. The central differences are constructed such that the derivative is evaluated at a full steps (temporal or spatial), resulting in fields components being sampled at half steps. For a scalar function this results in a derivative of the form

$$\frac{\partial f}{\partial x}(x) \approx \frac{f(x + \frac{\Delta x}{2}) - f(x - \frac{\Delta x}{2})}{\Delta x} + O[(\Delta x)^2]. \quad (2.9)$$

If we apply this stencil exemplary for Eq. 2.6, we identify a temporal derivative of the electric field and two spatial derivatives of the magnetic fields (in  $y$  and  $z$ ). Following the rule above, the differential equation should then be evaluated at a full time step, and full  $y$  and  $z$  steps. This in turn means that the electric field is evaluated at half time steps and the magnetic fields at half spatial steps that match the direction in which the derivative is computed (e.g. shifted by  $\Delta y$  for the derivative  $\frac{\partial}{\partial y}$ ). Note the absence of the derivative in  $x$  direction here, but to be consistent with the other equations, the evaluation is shifted by  $\frac{\Delta x}{2}$ . For the sake of convenience the notation

$$f(i\Delta x, j\Delta y, k\Delta z, n\Delta t) = f_{i,j,k}^n \quad (2.10)$$

will be used from now on.

The discretized equation 2.6 consequently reads

$$\begin{aligned} \frac{E_x|_{i+\frac{1}{2},j,k}^{n+\frac{1}{2}} - E_x|_{i+\frac{1}{2},j,k}^{n-\frac{1}{2}}}{\Delta t} &= \frac{1}{\varepsilon_0\mu_0} \left[ \frac{B_z|_{i+\frac{1}{2},j+\frac{1}{2},k}^n - B_z|_{i+\frac{1}{2},j-\frac{1}{2},k}^n}{\Delta y} - \frac{B_y|_{i+\frac{1}{2},j,k+\frac{1}{2}}^n - B_y|_{i+\frac{1}{2},j,k-\frac{1}{2}}^n}{\Delta z} \right] \\ &\quad - \frac{1}{\varepsilon_0} j_x|_{i+\frac{1}{2},j,k}^n. \end{aligned} \quad (2.11)$$

Rearranging leads to an explicit expression for the propagation of  $E_x$

$$\begin{aligned} E_x|_{i+\frac{1}{2},j,k}^{n+\frac{1}{2}} &= E_x|_{i+\frac{1}{2},j,k}^{n-\frac{1}{2}} \\ &\quad + \frac{\Delta t}{\varepsilon_0\mu_0} \left[ \frac{B_z|_{i+\frac{1}{2},j+\frac{1}{2},k}^n - B_z|_{i+\frac{1}{2},j-\frac{1}{2},k}^n}{\Delta y} - \frac{B_y|_{i+\frac{1}{2},j,k+\frac{1}{2}}^n - B_y|_{i+\frac{1}{2},j,k-\frac{1}{2}}^n}{\Delta z} \right] \\ &\quad - \frac{\Delta t}{\varepsilon_0} j_x|_{i+\frac{1}{2},j,k}^n. \end{aligned} \quad (2.12)$$

The right side of this equation only depends on field components from the past, allowing for an explicit propagation. Analogous expressions can be found for the remaining differential equations. The shift of the indices (e.g.  $\frac{\Delta x}{2}$  for  $E_x$ ) is chosen such, that the six resulting propagation equations match the Yee-staggering in Fig. 2.1 perfectly. Additionally, electric and magnetic field components are staggered in time (full time steps for  $B$ , half time steps for  $E$ ), resulting in alternating field updates, completing the numerical scheme for the solution of Maxwell's equations.

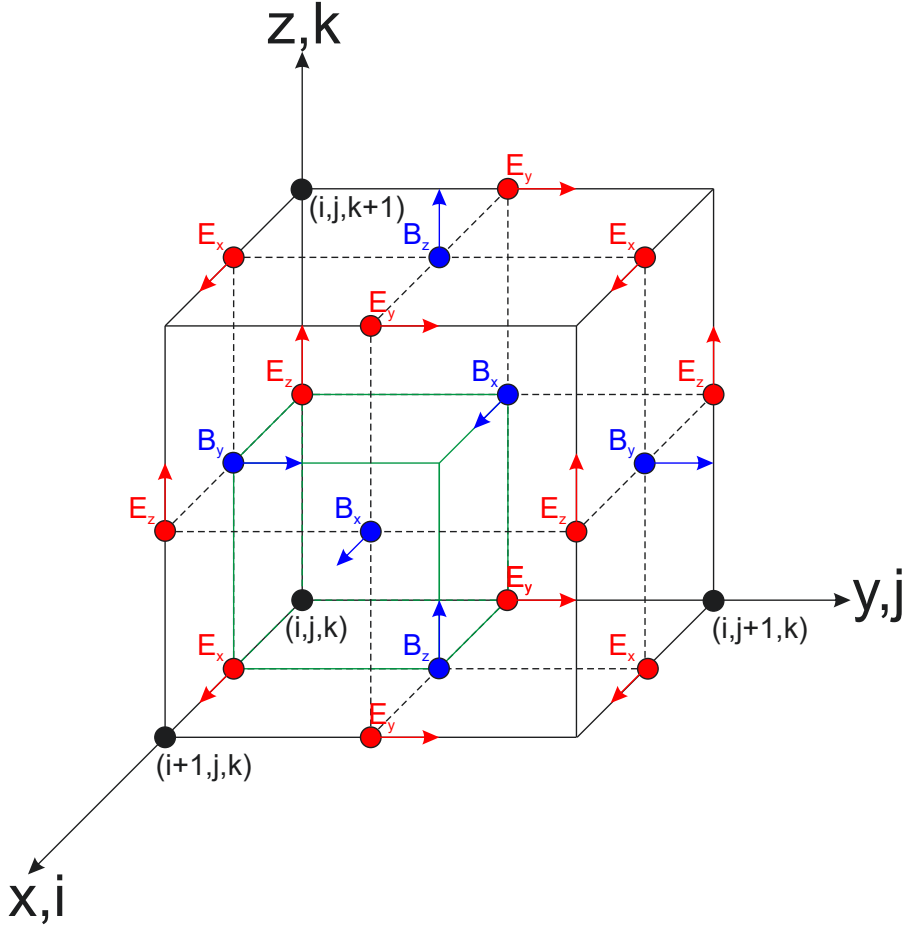


**Figure 2.1.:** Sketch of the Yee staggering [30]; the positions of the electric and magnetic field components are chosen such that they exactly match the centered finite difference discretization of Maxwell's curl equations. The green box marks the subset of fields that are only a halfstep away from  $(i, j, k)$ . From [64]

### 2.1.2. Absorbing boundary conditions and field source

To confine the simulation volume to a finite size, boundary conditions have to be applied. In this work, the most important boundary conditions are the periodic boundary condition (PBC) and the absorbing boundary condition (ABC). The former describes a periodic continuation of the simulation domain, the latter emulates an infinite extension of the grid. The basic idea of the chosen ABC is that the simulation volume is enclosed by a highly absorbing, non-reflecting medium layer. Most importantly, this artificial medium must not reflect for arbitrary incident angles. One solution to this problem was proposed by Stephen Gedney in 1996 [65] with the so called Uniaxial-Perfectly-Matched-Layer (UPML). The basic concept behind the UPML is to achieve no reflection at the interface (i.e. 'perfect matching') via an uniaxial anisotropic absorption layer. In the implementation for this work, the UPML has a thickness of ten grid cells, where the material parameters are ramped with a fourth-order polynomial from zero their maximum

(details can be found in [63]). The UPML layer is terminated with a periodic boundary condition. Fields that reach the end of the UPML are already strongly damped and are then mapped on the opposite side of the computational box, where they are further damped on their second way through the UPML layer.

In addition to absorbing boundary conditions, the so-called 'total field - scattered field' scheme can be used in FDTD for the input and output of electromagnetic fields. This ansatz is based on the linearity of Maxwell's equation, which allows the decomposition of the total electromagnetic fields into an incident and scattered part:

$$\mathbf{E}_{\text{tot}} = \mathbf{E}_{\text{inc}} + \mathbf{E}_{\text{scatt}} \quad (2.13)$$

$$\mathbf{B}_{\text{tot}} = \mathbf{B}_{\text{inc}} + \mathbf{B}_{\text{scatt}}. \quad (2.14)$$

The incident fields  $\mathbf{E}_{\text{inc}}$  and  $\mathbf{B}_{\text{inc}}$  are the fields that would exist in vacuum and the scattered fields  $\mathbf{E}_{\text{scatt}}$ ,  $\mathbf{B}_{\text{scatt}}$  are the fields resulting from the interaction with the material. In this work, only plane wave incident fields were implemented, allowing the propagation of the incident fields on a one-dimensional auxiliary grid. Consequently, the incident fields are known everywhere at any time during the simulation. This allows for a splitting of the simulation box into a center region, where the total fields are propagated and interact with the material, and a surrounding scattered field region as a layer around the main grid, where only the scattered fields are propagated. On the edge of the scattered field region to the total field region, the incident fields can be added or subtracted, providing a plane wave source. The knowledge of the scattered fields is vital for scattering simulations in FDTD as the scattered fields on the edge of the simulation box are recorded and transformed into the far field (see section 2.3).

## 2.2. Material response

Two possibilities for describing the bound-electron response of matter and their interaction with an electric field will be discussed. First, the classical, linear Drude-Lorentz model is presented (section 2.2.1), followed by a quantum mechanical few level description of the polarization dynamics using a density matrix formulation in the interaction picture (section 2.2.2). By matching the nonlinear system to the Drude-Lorentz oscillator, quantum mechanical system with the same linear response can be reconstructed (section 2.2.3).

### 2.2.1. Linear polarization

The classical Drude-Lorentz model (DLM) is a phenomenological model to describe the classical bound electron response of matter to electromagnetic fields [66, 67]. The optical properties and the dispersion are modeled by classical oscillators in time domain which yield the correct spectral response. Originally, Lorentz described the atom-field-interaction using an atom as a heavy mass (core) and the electrons with smaller mass, all connected by springs. The electrons are then set into motion by the electric field as it interacts with their charges. The force  $\mathbf{F}$  between electron and core is described by Hook's law ( $\mathbf{F} = -k\mathbf{r}$ , where  $k$  is the spring constant and  $\mathbf{r}$  the position). Without loss of generality, we define the electric field and thus the motion of electrons to follow the x-coordinate. If friction is also incorporated, the equation of motion (EOM) of a damped and driven harmonic oscillators follows as

$$\ddot{x} = -\nu\dot{x}(t) - \underbrace{\frac{k}{m}}_{\omega_0^2} x(t) + \frac{q}{m_e} E(t), \quad (2.15)$$

where  $x$  denotes the deviation from rest position,  $\nu$  the damping constant (the collision frequency),  $\omega_0$  the undamped eigenfrequency and  $m_e$  the electron mass. Recalling that the polarization density is given by  $P = n_0 d = n_0 q x$ , we get the equation of motion of the polarization density

$$\left[ \partial_t^2 + \nu \partial_t + \omega_0^2 \right] P(t) = n_0 \frac{q_e^2}{m_e} E(t). \quad (2.16)$$

In Fourier domain (for the definition of the sign convention for the Fourier transform see Appendix A), this equation of motion reads

$$\left[ \omega_0^2 - \omega^2 - i\omega\nu \right] P(\omega) = n_0 \frac{q_e^2}{m_e} E(\omega), \quad (2.17)$$

which leads to the spectral representation of the dipole response

$$P(\omega) = n_0 \frac{q_e^2}{m_e} \left[ \frac{1}{\omega_0^2 - \omega^2 - i\omega\nu} \right] E(\omega). \quad (2.18)$$

Using the definition of the susceptibility  $P(\omega) = \varepsilon_0 \chi(\omega) E(\omega)$  we thus find

$$\chi(\omega) = \frac{\omega_p^2}{\omega_0^2 - \omega^2 - i\omega\nu} \quad \text{with the plasma frequency} \quad \omega_p = \sqrt{\frac{n_0 q_e^2}{\varepsilon_0 m_e}}. \quad (2.19)$$

If we now combine  $N$  effective oscillators, each having its own susceptibility  $\chi_i(\omega)$ , the dispersion of an arbitrary linear physical medium (with multiple resonance frequencies) can be expressed as their sum

$$\chi(\omega) = \sum_i^N \chi_i(\omega) \quad \text{with} \quad \chi_i(\omega) = \frac{f_i \omega_p^2}{\omega_{0,i}^2 - \omega^2 - i\omega\nu_i}, \quad (2.20)$$

with the oscillator strength  $f_i$  describing the relative contribution of an individual oscillator to the total susceptibility. As each oscillator now has its respective susceptibility, they can also be considered separately. The equation for the polarization density in frequency domain reads for the  $i^{\text{th}}$  oscillator

$$\left[ \omega_{0,i}^2 - \omega^2 - i\omega\nu_i \right] P_i(\omega) = f_i \varepsilon_0 \omega_p^2 E(\omega). \quad (2.21)$$

Transforming back to time domain leads to the equation of motion of the polarization of one individual oscillator

$$\left[ \partial_t^2 + \nu_i \partial_t + \omega_{0,i}^2 \right] P_i(t) = f_i \varepsilon_0 \omega_p^2 E(t) = n_0 f_i \frac{q_e^2}{m_e} E(t). \quad (2.22)$$

To couple the polarization to Maxwell's equations in FDTD, the total polarization  $P(t) = \sum_i^N P_i(t)$  has to be evaluated. The parameters  $\nu_i$ ,  $\omega_{0,i}$  and  $f_i$  can be used as fit-parameters to approximate experimentally determined dielectric functions. They are usually determined for a specific frequency range (e.g. [68] for gold or [69, 70] for liquid helium). The advantage of this explicit temporal description is that we can describe the dispersion of an arbitrary linear medium in time domain over a wide frequency range by considering a sufficient number of oscillators. This translation of the spectral response to the time domain via oscillator differential equations is an indispensable tool in the FDTD method as the Fourier spectrum in each timestep is unknown. Another advantage of the Drude-Lorentz model for FDTD is that it is possible to describe negative relative permittivities. Implementing a negative relative permittivity directly into the FDTD propagators is numerically unconditionally unstable [63].

### 2.2.2. Nonlinear bound electron dynamics

In the previous section, the modeling of linear bound electron dynamics and the resulting electromagnetic response was discussed. There have been extensions of the Drude-Lorentz model to incorporate higher order susceptibilities [63, 71], where the latter paper bases the nonlinear Lorentz model on the analytical solution of a two-level system. The goal of this section is a local description of the induced nonlinear polarization dynamics originating from transitions between a set of relevant bound states. Instead of extending the oscillator model however, the evolution of the quantum system will be propagated directly.

To couple the quantum mechanical properties to the classical Maxwell equations 2.6 - 2.8, it is needed to evaluate the expectation value the dipole moment operator. To this end, we require knowledge of the state evolution, i.e. the evolution of the density matrix.

#### Single quantum system - Schrödinger picture and Interaction picture

As a starting point, we depart from the fully coherent dynamics of an individual quantum system, described by the time dependent Schrödinger equation (TDSE)

$$i\hbar \frac{\partial}{\partial t} |\Psi^S(t)\rangle = \hat{H}^S |\Psi^S(t)\rangle, \quad (2.23)$$

where  $|\Psi(t)\rangle$  is the state vector of the quantum system and  $\hat{H}$  the Hamiltonian.

Here the superscript  $S$  denotes the Schrödinger picture, where operators are fixed and states are time dependent. The TDSE is formally solved by the unitary time evolution

$$|\Psi^S(t)\rangle = \hat{U}(t) |\Psi(0)\rangle \quad (2.24)$$

$$\text{with } \hat{U}(t) = \mathcal{T} \exp \left[ -\frac{i}{\hbar} \int_0^t \hat{H}^S(t') dt' \right]. \quad (2.25)$$

where  $\hat{U}(t)$  is known as the Dyson series [72, Ch. 2.1] with the time-ordering operator  $\mathcal{T}$  [73, Ch. 5]. We see that the whole time evolution is governed by the full Hamiltonian. If we are only interested in the interaction of the quantum system with an external laser field and not in the 'trivial' evolution of the unperturbed system it is often beneficial to split the Hamiltonian into an unperturbed, time independent part, connected to the unperturbed orthogonal eigenstates  $|\Psi_j\rangle$  and eigenenergies  $\mathcal{E}_j$ , and a time dependent part describing the perturbation (or interaction)

$$\hat{H}^S(t) = \hat{H}_0^S + \hat{H}_{\text{int}}^S(t) \quad (2.26)$$

$$\text{with } \hat{H}_0^S |\Psi_j\rangle = \mathcal{E}_j |\Psi_j\rangle. \quad (2.27)$$

Inserting this splitting into the time evolution of the state allows us to pull out the unperturbed time evolution from the state

$$|\Psi^S(t)\rangle = e^{-\frac{i}{\hbar}\hat{H}_0^S t} \underbrace{\mathcal{T} \exp \left[ -\frac{i}{\hbar} \int_0^t \hat{H}_{\text{int}}^S(t') dt' \right]}_{:=|\Psi^I(t)\rangle} |\Psi(0)\rangle. \quad (2.28)$$

The latter part is the definition of a state in the so called interaction picture (superscript  $I$ ) where the states evolve in time due to the perturbation only. The definition above allows us to transform a state from one picture to the other with a unitary transformation

$$|\Psi^I(t)\rangle = \hat{U}_0^\dagger(t) |\Psi^S(t)\rangle \quad (2.29)$$

$$|\Psi^S(t)\rangle = \hat{U}_0(t) |\Psi^I(t)\rangle \quad (2.30)$$

$$\text{with } \hat{U}_0(t) = e^{-\frac{i}{\hbar}\hat{H}_0^S t}. \quad (2.31)$$

In the Schrödinger picture, observables ( $\hat{A}^S$ ) are time-independent and the time-dependence of their expectation value depends on the time evolution of the states

$$\langle \hat{A}^S \rangle = \langle \Psi^S(t) | \hat{A}^S | \Psi^S(t) \rangle. \quad (2.32)$$

The measured physical quantity (expectation value) should not depend on the picture we are in, so the expectation value in both pictures is the same, but the observable itself is time-dependent in the interaction picture

$$\langle \hat{A}^I \rangle = \langle \Psi^I(t) | \hat{A}^I(t) | \Psi^I(t) \rangle \quad (2.33)$$

$$= \langle \Psi^S(t) | \hat{U}_0(t) \hat{A}^I(t) \hat{U}_0^\dagger(t) | \Psi^S(t) \rangle \quad (2.34)$$

$$= \langle \Psi^S(t) | \hat{A}^S | \Psi^S(t) \rangle = \langle \hat{A}^S \rangle. \quad (2.35)$$

With this knowledge we can now also transform observables from one picture to the other

$$\hat{A}^I(t) = \hat{U}_0(t)^\dagger \hat{A}^S \hat{U}_0(t) \quad (2.36)$$

$$\hat{A}^S = \hat{U}_0(t) \hat{A}^I(t) \hat{U}_0(t)^\dagger. \quad (2.37)$$

As the Hamiltonian  $\hat{H}^I = \hat{H}_0^I + \hat{H}_{\text{int}}^I$  is also an operator, we get for the unperturbed Hamiltonian in the interaction picture

$$\hat{H}_0^I = \hat{U}_0^\dagger \hat{H}_0^S \hat{U}_0 = e^{\frac{i}{\hbar}\hat{H}_0^S t} \hat{H}_0^S e^{-\frac{i}{\hbar}\hat{H}_0^S t} = \hat{H}_0^S. \quad (2.38)$$

Because the Hamiltonian commutes with itself. For the interaction Hamiltonian we get

$$\begin{aligned} \hat{H}_{\text{int}}^I(t) &= \hat{U}_0(t)^\dagger \hat{H}_{\text{int}}^S(t) \hat{U}_0(t) \\ &= e^{\frac{i}{\hbar}\hat{H}_0^S t} \hat{H}_{\text{int}}^S(t) e^{-\frac{i}{\hbar}\hat{H}_0^S t}. \end{aligned} \quad (2.39)$$

Meaning that the unperturbed Hamiltonians are the same but the interaction Hamiltonian in the Schrödinger picture and the interaction picture are indeed different.

In the end, we are interested in the temporal dynamics of the quantum system described by the Schrödinger equation. By inserting the transformation of the states 2.30 and the Hamiltonian (equations 2.38, 2.39) into the Schrödinger equation 2.23, we arrive at the Schrödinger equation in the interaction picture

$$i\hbar\frac{\partial}{\partial t}|\Psi^I(t)\rangle = \hat{H}_{\text{int}}^I(t)|\Psi^I(t)\rangle, \quad (2.40)$$

meaning that the state in the interaction picture does indeed evolve by the interaction part of the Hamiltonian. In the following, most calculation will only be done in the interaction picture. It is however often more intuitive to define observables in the Schrödinger picture and express their expectation values in terms of states in the interaction picture.

### Time dependent perturbation theory

A common way to solve the the Schrödinger equation for the time dependent wavefunction is to expand the wavefunction into a superposition of eigenstates of the unperturbed Hamiltonian (Eq. 2.27)

$$|\Psi^I(t)\rangle = \sum_j c_j^I(t) |\Psi_j\rangle. \quad (2.41)$$

The time-dependent coefficients  $c_j^I(t)$  (probability amplitudes) then contain all time-dependence of the state, so this approximation is valid if the eigenstates do not change in time (e.g. due to ionization). Employing the state expression 2.41 for the evaluation of the expectation value of  $A = \langle \hat{A} \rangle$

$$\langle \hat{A} \rangle = \langle \Psi^I(t) | \hat{A}^I(t) | \Psi^I(t) \rangle = \sum_{n,m} \underbrace{\langle \Psi_n | \hat{A}^I(t) | \Psi_m \rangle}_{A_{nm}^I(t)} c_n^{I*}(t) c_m^I(t) \quad (2.42)$$

$$= \sum_{n,m} \langle \Psi_n | e^{\frac{i}{\hbar} \hat{H}_0^S t} \hat{A}^S e^{-\frac{i}{\hbar} \hat{H}_0^S t} | \Psi_m \rangle c_n^{I*}(t) c_m^I(t) \quad (2.43)$$

$$= \sum_{n,m} \langle \Psi_n | e^{\frac{i}{\hbar} \mathcal{E}_n t} \hat{A}^S e^{-\frac{i}{\hbar} \mathcal{E}_m t} | \Psi_m \rangle c_n^{I*}(t) c_m^I(t) \quad (2.44)$$

$$= \sum_{n,m} \underbrace{\langle \Psi_n | \hat{A}^S | \Psi_m \rangle}_{A_{nm}^S} e^{i\omega_{nm} t} c_n^{I*}(t) c_m^I(t), \quad (2.45)$$

with the matrix elements  $A_{nm}^{I/S}$  of the observable and the transition frequency  $\omega_{nm} = \frac{\mathcal{E}_n - \mathcal{E}_m}{\hbar}$ . Where we transformed the observable back to the Schrödinger picture (Eq. 2.37). The main takeaway of this expression is that matrix elements of an observable transform by multiplying with a factor only containing the transition energy and time

$$A_{nm}^I(t) = A_{nm}^S e^{i\omega_{nm} t}, \quad (2.46)$$

which corresponds to the trivial rotation of observables in time. A physical analogon would be the the transformation to a rotating frame (rotating with frequency  $\omega_{nm}$ ) in classical mechanics. To eventually evaluate the expectation value, we are interested in the evolution of the probability amplitudes as they are governing what we are ultimately measuring (or coupling to our classical Maxwell's equations). Inserting the expansion 2.41 into the TDSE in the interaction picture 2.40

$$i\hbar \frac{\partial}{\partial t} \sum_j c_j^I(t) |\Psi_j\rangle = \sum_j \hat{H}_{\text{int}}^I(t) c_j^I(t) |\Psi_j\rangle \quad (2.47)$$

and multiplying with  $\langle \Psi_k |$  gives us the equation of motion of the coefficients

$$i\hbar \dot{c}_k^I(t) = \sum_j c_j^I(t) \underbrace{\langle \Psi_k | \hat{H}_{\text{int}}^I(t) | \Psi_j \rangle}_{H_{\text{int},kj}^I}. \quad (2.48)$$

Here  $H_{\text{int},kj}^I$  are the matrix elements of the interaction Hamiltonian in the interaction picture. If we recall that usually the external perturbation is given in the Schrödinger picture (i.e. by an external electric field which does not rotate with the eigenstates of the quantum system), it is beneficial to express the interaction Hamiltonian again via the Schrödinger picture

$$i\hbar\dot{c}_k^I(t) = \sum_j c_j^I(t) \langle \Psi_k | \hat{U}_0^\dagger(t) \hat{H}_{\text{int}}^S \hat{U}_0(t) | \Psi_j \rangle \quad (2.49)$$

$$= \sum_j c_j^I(t) \langle \Psi_k | e^{\frac{i}{\hbar}\mathcal{E}_k t} \hat{H}_{\text{int}}^S e^{-\frac{i}{\hbar}\mathcal{E}_j t} | \Psi_j \rangle \quad (2.50)$$

$$= \sum_j c_j^I(t) \underbrace{\langle \Psi_k | \hat{H}_{\text{int}}^S | \Psi_j \rangle}_{H_{\text{int},kj}^S} e^{i\omega_{kj}t}. \quad (2.51)$$

With the matrix elements of the interaction Hamiltonian in the Schrödinger picture. The above equation of motion illustrates that the trivial rotation of the transitions is pulled out, while the dynamics of the probability amplitudes depends on the matrix elements of the interaction Hamiltonian in the Schrödinger picture. If now the matrix elements of the Hamiltonian and the observables are known, the propagation of the considered individual quantum system according to the EOM and the corresponding time-evolution of observables are fixed.

### Density matrix formulation

In the single quantum system case a fully coherent mixture of states was used to describe a so-called pure state (Eq. 2.41), which corresponds to a quantum superposition (like an amplitude superposition in wave optics). Considering a statistical mixture (ensemble; indicated with index  $M$ ) of pure states

$$|\Psi^{IM}(t)\rangle = \sum_j c_j^{IM}(t) |\Psi_j\rangle, \quad \text{which is realized with probability } p_M, \quad (2.52)$$

we can describe an incoherent mixture (c.f. in ray optics).

In order to evaluate an observable in such a mixed state, it is now necessary to additionally sum over the possible configurations  $M$  (we are still using the interaction picture)

$$\langle \hat{A}^I \rangle = \sum_M p_M \langle \Psi^{IM}(t) | \hat{A}^I(t) | \Psi^{IM}(t) \rangle \quad (2.53)$$

$$= \sum_M \sum_{n,m} p_M A_{nm}^I c_n^{IM*}(t) c_m^{IM}(t). \quad (2.54)$$

With the definition of the density matrix

$$\rho_{mn}^I = \sum_M p_M c_n^{IM*}(t) c_m^{IM}(t) \quad \text{in the interaction picture} \quad (2.55)$$

$$\rho_{mn}^S = \rho_{mn}^I e^{-i\omega_{mn}t} \quad \text{in the Schrödinger picture} \quad (2.56)$$

we can express the expectation value as

$$\langle \hat{A}^I \rangle = \sum_{n,m} A_{nm}^I \rho_{mn}^I = \sum_{n,m} A_{nm}^S \underbrace{e^{i\omega_{nm}t} e^{i\omega_{mn}t}}_{=1} \rho_{mn}^S \quad (2.57)$$

$$= \text{Tr}(\hat{A}^I \hat{\rho}^I) = \text{Tr}(\hat{A}^S \hat{\rho}^S), \quad (2.58)$$

where we used the associated density operator  $\hat{\rho}^I$

$$\hat{\rho}^I = \sum_M p_M |\Psi^{IM}\rangle \langle \Psi^{IM}|. \quad (2.59)$$

This enables the elegant representation of the expectation value of an observable in a statistical mixture as the trace of a matrix product with the density operator (see Eqs. 2.58). Also note that both expressions in Eq. 2.57 show in a very compact form how the observables do not rotate in the Schrödinger picture in contrast to the interaction picture. The diagonal elements of the density matrix describe *occupations*, while the off-diagonal elements describe *coherences*.

To couple the time evolution of the quantum system to the fields, we are interested in the state dynamics of the mixed state. To this end, we consider the time evolution of the density matrix (Eq. 2.55)

$$\frac{\partial}{\partial t} \rho_{mn}^I = \sum_M \left[ \dot{p}_M c_n^{IM*}(t) c_m^{IM}(t) + p_M \dot{c}_n^{IM*}(t) c_m^{IM}(t) + p_M c_n^{IM*}(t) \dot{c}_m^{IM}(t) \right]. \quad (2.60)$$

As long as interactions beyond those contained in the interaction Hamiltonian are neglected (e.g. no relaxation or cross-talk between ensemble members due to collisions), the term  $\dot{p}_M$  vanishes. Inserting the evolution of the probability amplitude (Eq. 2.48) from the previous section and rearranging we find

$$\frac{\partial}{\partial t} \rho_{mn}^I = \sum_M p_M \frac{1}{i\hbar} \sum_j \left[ -c_j^{IM*}(t) H_{\text{int},nj}^I c_m^{IM}(t) + c_n^{IM*}(t) c_j^{IM}(t) H_{\text{int},jm}^I \right] \quad (2.61)$$

$$= -\frac{i}{\hbar} \sum_j \left[ -\sum_M p_M c_j^{IM*}(t) c_m^{IM}(t) H_{\text{int},nj}^I + H_{\text{int},jm}^I \sum_M p_M c_n^{IM*}(t) c_j^{IM}(t) \right] \quad (2.62)$$

$$= -\frac{i}{\hbar} \sum_j \left[ H_{\text{int},mj}^I \rho_{jn}^I - \rho_{mj}^I H_{\text{int},jn}^I \right]. \quad (2.63)$$

Both terms in the square bracket have the structure of a matrix product and together form a commutator which in matrix (operator) form leads to the equation of motion for

the density matrix (in the interaction picture)

$$\frac{\partial \hat{\rho}^I}{\partial t} = -\frac{i}{\hbar} [\hat{H}_{\text{int}}^I, \hat{\rho}^I], \quad (2.64)$$

which is called von-Neumann equation [74]. Now it is possible to introduce a phenomenological dissipation term with the rate  $\bar{\gamma}$  to describe (i) decoherence  $\gamma_d$  (i.e. decay of coherences and thus removing the quantum mechanical mixture) and (ii) the relaxation  $\gamma_r$  of population towards an equilibrium state  $\hat{\rho}^{\text{eq}}$  (which we assume to be the fully occupied ground state). For clarity, the dissipation matrix reads for  $N$  bound states

$$\bar{\gamma} = \begin{pmatrix} \sum_{n=1}^N \gamma_{r,nn} & \gamma_{d,12} & \cdots & \gamma_{d,1N} \\ \gamma_{d,21} & \gamma_{r,11} & & \vdots \\ \vdots & & \ddots & \gamma_{d,(N-1)N} \\ \gamma_{d,N1} & \cdots & \gamma_{d,N(N-1)} & \gamma_{r,NN} \end{pmatrix} \quad (2.65)$$

such that the relaxation terms are located at the main diagonal and the decoherences are the off-diagonal elements. This results in the modified von-Neumann equation

$$\frac{\partial \hat{\rho}^I}{\partial t} = -\frac{i}{\hbar} [\hat{H}_{\text{int}}^I, \hat{\rho}^I] - \bar{\gamma} \circ (\hat{\rho}^I - \hat{\rho}^{\text{eq}}) \quad (2.66)$$

where the symbol  $\circ$  denotes an element-wise multiplication. With the expressions for calculating expectation values of observables (Eq. 2.58) and the EOM for the density matrix (Eq. 2.66) we are now able to propagate the time-evolution of an observable if we know the Hamiltonian, the observable and the dissipation rate  $\bar{\gamma}$ . To employ the density matrix model, we will next consider a few-level system (FLS) interacting with an electric field. The observable of interest will be the electric dipole operator, whose expectation value couples back to the electric field according to Maxwell's equations 2.6 - 2.8.

### 2.2.3. Few level system, usage and weak-field limit

For employing the few level density matrix model we consider a helium like system in single active electron approximation with ground state  $|0\rangle$  reflecting the He  $1s^2$  state and multiple excited states  $|j\rangle$  reflecting higher s states like  $1s^1 2s^1$  or p-states  $1s^1 2p_i^1$  with  $i = x, y, z$ . Each of these levels corresponds to an eigenstate of the field-free Hamiltonian and consequently has its corresponding eigenenergy:  $\hat{H}_0^S |\Psi_j\rangle = \mathcal{E}_j |\Psi_j\rangle$ . The system is excited by an external electric field, so the interaction Hamiltonian is described in the dipole approximation in length form in the Schrödinger picture

$$\hat{H}_{\text{int}}^S = -\hat{\mathbf{d}}^S \cdot \mathbf{E}(t). \quad (2.67)$$

The dipole operator has the matrix elements

$$\langle \Psi_n | \hat{\mathbf{d}}^S | \Psi_m \rangle = \boldsymbol{\mu}_{nm}. \quad (2.68)$$

With the transition dipole matrix elements  $\boldsymbol{\mu}_{nm}$ . Note that they have the form of three-dimensional vectors where the direction has the meaning of the spatial direction of the transition (e.g. for a transition  $1s^2 \rightarrow 1s^1 2p_x^1$  the vector would point in  $x$ -direction). The resulting matrix elements of the interaction Hamiltonian follow as

$$H_{\text{int},nm}^S = -\boldsymbol{\mu}_{nm} \cdot \mathbf{E}(t). \quad (2.69)$$

For our application, the most important observable is the dipole moment, which we can express with the density matrix in terms of a trace (Cartesian component-wise)

$$\langle \hat{\mathbf{d}} \rangle = \text{Tr} \left( \hat{\mathbf{d}}^S \hat{\rho}^S \right) = \begin{pmatrix} \text{Tr} \left( \hat{d}_x^S \hat{\rho}^S \right) \\ \text{Tr} \left( \hat{d}_y^S \hat{\rho}^S \right) \\ \text{Tr} \left( \hat{d}_z^S \hat{\rho}^S \right) \end{pmatrix}. \quad (2.70)$$

The resulting polarization density

$$\mathbf{P}_{\text{FLDM}} = n_0 \langle \hat{\mathbf{d}} \rangle \quad (2.71)$$

serves as a feedback for the field propagation, analogously to the Drude-Lorentz model in subsection 2.2.1.

Calculation of the evolution of the dipole moment consequently requires the solution of the EOM of the density matrix. Its time evolution is evaluated in the interaction picture to remove the trivial unperturbed dynamics from the propagation. To this end, we transform the elements of the interaction Hamiltonian and the density matrix to the interaction picture (as in Eq. 2.46), propagate the density matrix using the generalized von-Neumann equation 2.66 and finally calculate the dipole moment (Eq. 2.70) by transforming either operator ( $\hat{d}$  or  $\hat{\rho}$ ) to the picture of the other.

The response of the FLDM to the electric field  $\mathbf{E}(t)$  is determined by the transition energies  $\hbar\omega_{nm} = \mathcal{E}_n - \mathcal{E}_m$ , the magnitude and direction of the transition dipole matrix elements  $\boldsymbol{\mu}_{nm}$  and the relaxation and damping rate  $\bar{\gamma}$ . These parameters can be fixed by matching the linear response behavior of the FLS to the optical parameters of the considered material.

### Two level system: Matching the linear limit of the FLDM model to the DLM oscillator

For matching the FLDM model to the DLM, we must determine the weak-field limit of the FLDM response. It only has to be considered along one axis, e.g. the  $x$ -axis, because of the isotropy of the linear response in our model. For the sake of clarity, we will limit ourselves to one transition and one oscillator respectively. The two-level

system (initialized in ground state  $|0\rangle$ , transition energy  $\hbar\omega_{01}$  to the excited state  $|1\rangle$ , decoherence  $\gamma_d$ , transition dipole moment  $\mu$ ). We further assume that relaxation, e.g. due to radiative decay, is negligible on the time scales of the considered femtosecond scattering dynamics. Under these assumptions the EOM for the expectation value of the dipole moment reads (detailed derivation in appendix B)

$$\langle \ddot{\hat{d}}_x \rangle = i\omega_{10}\mu \left[ -\frac{2i}{\hbar} H_{\text{int},01}^S (\rho_{11}^I - \rho_{00}^I) \right] - 2\gamma_d \langle \dot{\hat{d}}_x \rangle - [\gamma_d^2 + \omega_{10}^2] \langle \hat{d}_x \rangle, \quad (2.72)$$

which is still exact if only two levels are coupled (ideal two level system). In the weak field limit, the ground state will always be populated while the excited state will not ( $\rho_{11}^I = 0, \rho_{00}^I = 1$ )

$$\langle \ddot{\hat{d}}_x \rangle = -[\gamma_d^2 + \omega_{10}^2] \langle \hat{d}_x \rangle - 2\gamma_d \langle \dot{\hat{d}}_x \rangle + \frac{2\omega_{10}\mu^2}{\hbar} E_x(t), \quad (2.73)$$

where we inserted the interaction Hamiltonian in the Schrödinger picture  $H_{\text{int},01}^S = -\mu E_x(t)$ . Separating homogenous and inhomogenous parts results in the EOM of a driven damped harmonic oscillator

$$\langle \ddot{\hat{d}}_x \rangle + 2\gamma_d \langle \dot{\hat{d}}_x \rangle + [\gamma_d^2 + \omega_{10}^2] \langle \hat{d}_x \rangle = \frac{2\omega_{10}\mu^2}{\hbar} E_x(t). \quad (2.74)$$

To compare this equation to one Drude-Lorentz oscillator, we recall the EOM (Eq. 2.22) using  $d = \frac{P}{n_0}$

$$\ddot{d} + \nu \dot{d} + \omega_0^2 d = f \frac{q_e^2}{m_e} E(t). \quad (2.75)$$

Matching the prefactors of expectation values for dipole acceleration, velocity and magnitude to the classical EOM finally yields

$$\gamma_d = \frac{\nu}{2}, \quad \omega_{10} = \sqrt{\omega_0^2 - \frac{\nu^2}{4}}, \quad \text{and} \quad \mu = q_e \sqrt{\frac{f\hbar}{2\omega_{10}m_e}}. \quad (2.76)$$

We see that the resonance frequency  $\omega_0$  has the meaning of the shifted transition frequency  $\omega_{10}$ . Additionally for oscillating cases  $\gamma_d$  has the meaning of a damping constant. Most importantly, the FLDM parameters are now fully matched to the DLM parameters such that we can construct a quantum version with the same linear response as a classical oscillator. Vice versa, fitting the linear response dispersion of quantum mechanical systems is possible.

### 2.3. Near field to far field transformation

To evaluate the electromagnetic fields in the far field (i.e. to obtain scattering images), the fields are propagated using a near field to far field transformation based on the equivalent source theorem and usage of free-space propagators. As the complete derivation is quite lengthy, only the key points are presented here, whereas the details can be found in the appendix C. The derivation is based on [75] and [63] but presented using our notation.

- (i) The electromagnetic fields passing a closed surface  $S$  (with normal vector  $\mathbf{n}$ ) around the scattering object (see Fig. 2.2 (a)) are recorded to construct a so-called *equivalent source* (c.f. section C.2), that produces the same scattered fields outside of the surface ( $\mathbf{B}_1$  and  $\mathbf{E}_1$ ) as the original problem - but without any medium (Fig. 2.2 (b)). The equivalent source consists of surface currents  $\mathbf{J}_S$  and surface magnetization rates  $\dot{\mathbf{M}}_S$  given by

$$\mathbf{n} \times \mathbf{B}_1 = \mu_0 \mathbf{J}_S \quad (2.77)$$

$$\text{and } \mathbf{n} \times \mathbf{E}_1 = -\mu_0 \dot{\mathbf{M}}_S. \quad (2.78)$$

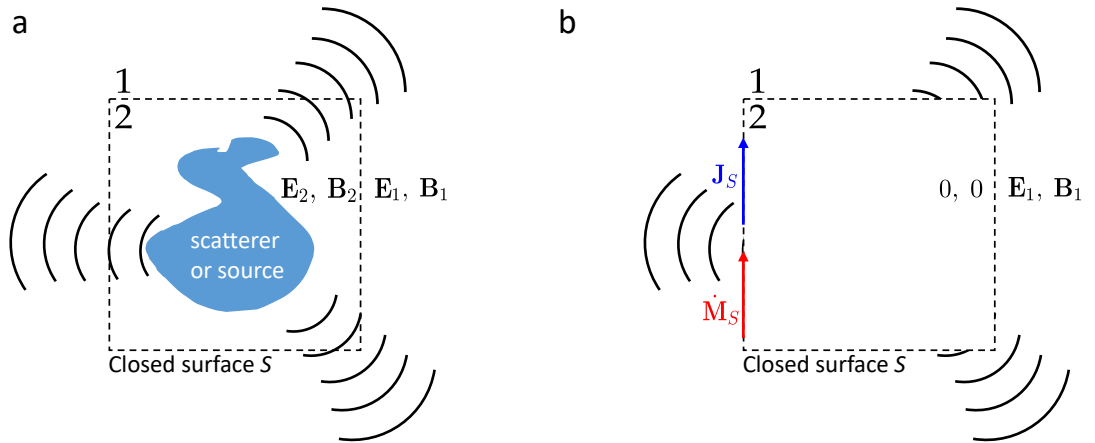


**Figure 2.2.:** (adapted from [75]) Principle of the equivalent source theorem: (a) Original Problem where a scatterer emits the fields  $\mathbf{E}$  and  $\mathbf{B}$ . (b) Equivalent problem without any medium, fields inside the closed surface are set to zero. The equivalent source, i.e.  $\mathbf{J}_S$  and  $\dot{\mathbf{M}}_S$ , yields the same electromagnetic fields  $\mathbf{E}_1, \mathbf{B}_1$  outside of  $S$  as the original problem.

- (ii) The equivalent scenario can be used to calculate the electromagnetic fields using only free-space propagators based on the vector potential resulting from  $\mathbf{J}_S$  and  $\dot{\mathbf{M}}_S$  (c.f. section C.3).
- (iii) The far fields can be evaluated, simplifying the fully general field equations (see section C.4). The end result is the spectrally selective scattered power at a given scattering direction  $\vartheta, \varphi$ , requiring only the equivalent source terms

$$P_{\text{scat}}(\vartheta, \varphi) = \frac{\mu_0 k^2}{32\pi^2 r^2 c} \left( |cL_\vartheta + \dot{N}_\varphi|^2 + |cL_\varphi - \dot{N}_\vartheta|^2 \right) \quad (2.79)$$

with the fields

$$L_{\vartheta/\varphi}(\vartheta, \varphi) = \iint_S \left[ \mathbf{e}_{\vartheta/\varphi} \cdot \mathbf{J}_S(\mathbf{r}') \right] e^{-ikr' \mathbf{e}_r \cdot \mathbf{e}_{r'}} d\mathbf{f}' \quad (2.80)$$

$$\dot{N}_{\vartheta/\varphi}(\vartheta, \varphi) = \iint_S \left[ \mathbf{e}_{\vartheta/\varphi} \cdot \dot{\mathbf{M}}_S(\mathbf{r}') \right] e^{-ikr' \mathbf{e}_r \cdot \mathbf{e}_{r'}} d\mathbf{f}'. \quad (2.81)$$

## 2.4. Numerical implementation

The electromagnetic fields are solved using the FDTD algorithm [63] in C++. The propagation of the von-Neumann equation is solved using Heun's method (Runge-Kutta 2nd order [76]), where the electromagnetic fields need to be predicted once in each step for each grid point, doubling computing time. The numerical computation is parallelized in space using OpenMP, which is a shared memory parallelization. On a single computation node with  $N$  threads, the numerical grid is divided into  $N$  slabs, such that each thread takes care of one slab. In the near field to far field transformation, the surface integration of the surface currents and magnetization rates (Eqs. 2.80, 2.81) is parallelized in the same fashion. Here, the integration over one surface needs to be done for each combination of angles  $\vartheta$ ,  $\varphi$  and also for each frequency, making it nearly as computationally demanding as the full propagation of the problem.

The two major limitations of the shared memory implementation are (1st) that faster parts of the simulation volume have to wait for the slower ones (i.e. material vs. vacuum) and (2nd) that we are limited to a single computation node when using mainframe computers. In the case of this work this means that we can only use 80 threads on our group high-performance computer (*MOLARIS*) or 192 on HLRN 2 (*Norddeutscher Verbund Für Hoch- und Höchstleistungsrechnen; North-German Supercomputing Alliance*), even though we could access hundreds of nodes there. Furthermore, this implementation is limited by the memory of one node, which can be a limiting factor for FDTD given how many different variables are stored in each grid point in the volume (e.g. electric field (3), magnetic field (3), polarization (3), density matrix (2 per allowed transition (coherences) and 1 per level (occupations)) and also at the surface (surface currents for each considered frequency).



# 3. Quantum Coherent Diffractive Imaging - Single Active Transition

In this chapter, we investigate at which point the linear response picture in coherent diffractive imaging of helium nanodroplets breaks down and how quantum effects beyond linear response, e.g. due to population transfer, modify the scattering. To this end, we use the Drude-Lorentz description of the local response as the starting point and extend the description with the nonlinear FLDM model for the  $1s^2$ - $1s2p$  transition. For already experimentally reachable pulse parameters and strong, resonant XUV excitation, we find significant deviations from the linear response case. Our results demonstrate that nonlinear spatiotemporal excitation dynamics give rise to a diverse range of features in the scattering patterns.

Note that the results in this chapter are published in [BK2]. The discussion follows these results, in more detail where appropriate. Especially subsection 3.3.3 gives more insight into the analysis of the spectra of the scattered fields.

## 3.1. Simulation setup and linear response benchmark

In accordance to section 2.2.3 we model the local response using the described few-level density matrix (FLDM) model that is sketched in Fig. 3.1. It is essentially modeling a single transition (two-level system) with the excited states (2p orbitals) being degenerate (energy  $\mathcal{E}_1 = \mathcal{E}_2 = \mathcal{E}_3$ ) in the three orbital quantum numbers along the Cartesian axes, making the setup a four-level system with a common ground state (energy  $E_0$ ) [BK2]. The transition dipole matrix elements  $\mu_{nm} = \mu$  in this case are particularly simple in structure because there are no dipole-allowed transition between the p-states leading to

the dipole operator in the Schrödinger picture

$$\hat{\mathbf{d}}^S = \begin{bmatrix} 0 & \mu \mathbf{e}_x & \mu \mathbf{e}_y & \mu \mathbf{e}_z \\ \mu \mathbf{e}_x & 0 & 0 & 0 \\ \mu \mathbf{e}_y & 0 & 0 & 0 \\ \mu \mathbf{e}_z & 0 & 0 & 0 \end{bmatrix}, \quad (3.1)$$

where the magnitude of the isotropic transition dipole moment is the same for all degenerate transitions and the direction is associated to the three Cartesian coordinates ( $\mathbf{e}_i$  with  $i = x, y, z$ ). As before, we assume the equilibrium state  $\hat{\rho}^{\text{eq}}$  to be the fully occupied ground state. Assuming symmetric relaxation and decoherence between the active transitions, we have the dissipation rate

$$\bar{\gamma} = \begin{bmatrix} \gamma_r & \gamma_d & \gamma_d & \gamma_d \\ \gamma_d & \gamma_r & 0 & 0 \\ \gamma_d & 0 & \gamma_r & 0 \\ \gamma_d & 0 & 0 & \gamma_r \end{bmatrix}, \quad (3.2)$$

where  $\gamma_d$  is the decoherence between ground and excited states and  $\gamma_r$  is the relaxation of population into the ground state. For helium however, the latter is negligible on the timescales of the considered fs scattering dynamics, so we chose  $\gamma_r = 0$ . Moreover the assumed isotropic response and also the degeneracy of excited states requires the decoherence to vanish between them.

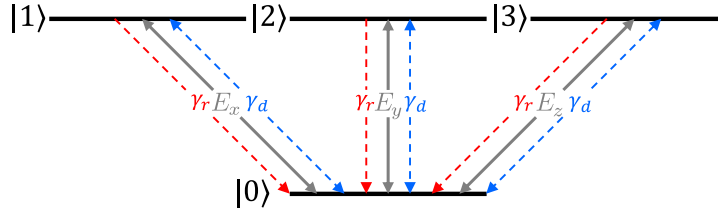


**Figure 3.1.:** Sketch of the active states of the few-level system used to describe the  $1s^2$ - $1s2p$  excitation in Helium.  $|0\rangle$  describes the ground state and  $|1\rangle$ ,  $|2\rangle$ ,  $|3\rangle$  are the degenerate excited state orbitals ( $2p$ ). The solid grey arrows mark the electric field component coupling to the respective transition and dashed red and blue arrows indicate relaxation ( $\gamma_r$ ) and decoherence ( $\gamma_d$ ), respectively. Adapted from [BK2]

This leaves us with three parameters that are left for this particular four-level system. As described in section 2.2.3, we can now match the FLDM parameters to DLM parameters that were fitted to experimental data, measuring the  $1s$ - $2p$  resonance of liquid helium He [70, 69] as seen in Fig. 3.2.

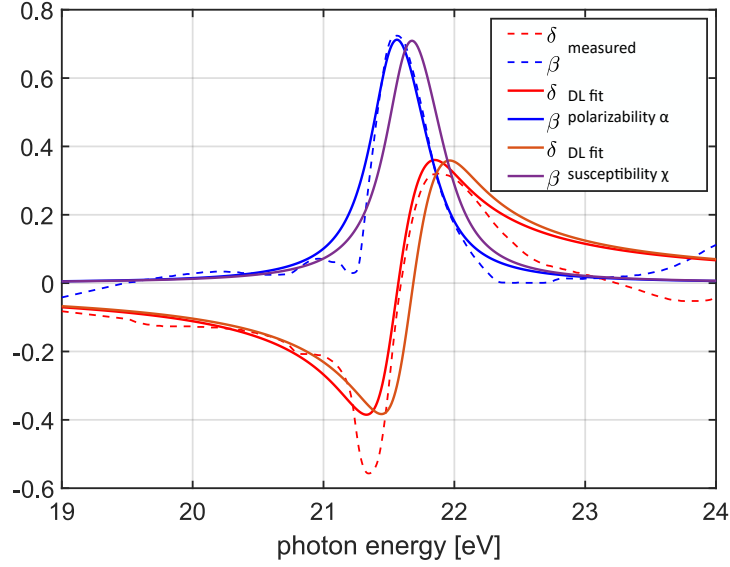


**Figure 3.2.:** Linear response (refractive index  $n = 1 - \delta + i\beta$ ) of liquid helium near the  $1s^2$ - $1s2p$  transition. Measured (dashed) and fitted values (solid lines) using parameters from [70, 69] for fitting the susceptibility  $\chi$  (orange, purple) and for fitting the polarizability  $\alpha$  (red, blue) that are then used to calculate  $n$ . Adapted from [BK2].

In this application, we couple the few-level system to the macroscopic electric field (without the Clausius-Mossotti correction that will be discussed in section 4.1.2) as this makes the benchmark and comparison with the DLM model very straightforward.

In the reference [69], from where the Drude-Lorentz parameters were taken, the experimental data was actually fitted by the atomic polarizability  $\alpha$  (i.e. the response to the local electric field at the position of an atom) and not the susceptibility  $\chi$  (i.e. the response of the medium to the macroscopic field). Using the resulting Drude-Lorentz parameters to calculate the susceptibility  $\chi$  (Eq. 2.19, orange and purple solid lines in Fig. 3.2) or using the same expression (i.e. with  $\alpha$  on the left side in Eq. 2.19 instead of  $\chi$ ) to calculate the atomic polarizability  $\alpha$  and then calculating the refractive index  $n = \sqrt{1 + \chi}$  using Eq. E.6 from appendix E (red and blue lines), result in a shift of the resonance peak.

This shift is so small that it does not influence the following calculations, especially because we want to be consistent within the DLM and FLDM model, such that they both couple to the macroscopic field.

The DLM parameters for an atomic density of  $n_0 = 0.022\text{\AA}^{-3}$  are (c.f. Eq. 2.76):

	resonance	damping	coupling
Drude-Lorentz	$\hbar\omega_0 = 21.61 \text{ eV}$	$\hbar\nu = 0.43 \text{ eV}$	$f = 0.49$
FLDM	$\hbar\omega_{10} = 21.61 \text{ eV}$	$\hbar\gamma_d = 0.215 \text{ eV}$	$\mu = 0.2939 \text{ e\AA} = 1.41 \text{ D}$

At this point, it should be emphasized that, in order to produce trustworthy results, it is of great importance to provide numerical stability for the FDLM-FDTD simulations. For the parameters used in this scenario, stability is ensured for all geometries. Nevertheless, there exist cases in which the model becomes conditionally unstable which will be discussed in section 4.1.

To examine how the nonlinear local polarization response affects the scattering process and final diffraction pattern under realistic conditions, we utilized a spherical Helium droplet with a radius of 300 nm as a model system [BK2]. It is positioned in a computational domain consisting of a  $251 \times 251 \times 251$  cubic grid with a spatial resolution of  $\Delta x = 2.8$  nm, as depicted in Fig. 3.3. The resonant incident pulse is linearly polarized along the  $x$ -axis, with a flat phase front and a central photon energy of  $\hbar\omega_{\text{inc}} = 21.61$  eV. It propagates along the  $z$ -axis and is characterized by a Gaussian temporal envelope with a duration of 8 fs (FWHM). The pulse has to be that short to investigate the coherent dynamics within the dephasing time.

The model used for the integration of the polarization response is either DLM or FLDM. The scattered fields are sampled on a cubic control surface (green in Fig. 3.3), and a discrete Fourier transform is used on the fly to decompose them into spectral components. The electric and magnetic fields' spectral amplitudes and phases on the control surface are employed to create electric and magnetic surface currents that act as an equivalent source (as described in chapter 2.3 and [63]). Scattering in the far-field is then evaluated for each spectral component, resulting in spectrally-resolved scattering images, which cover the scattering in the full solid angle. The final predicted scattering images are obtained by summing up individual spectral contributions in real space. To ensure consistency between polarization models, scattering images were calculated for both DLM and FLDM simulations at low pulse intensity. The obtained scattering images display the typical ring structure for spherical droplets [26]. The comparison of the respective (spectrally integrated) scattering profiles in Fig. 3.3 confirms the agreement in the linear response limit.

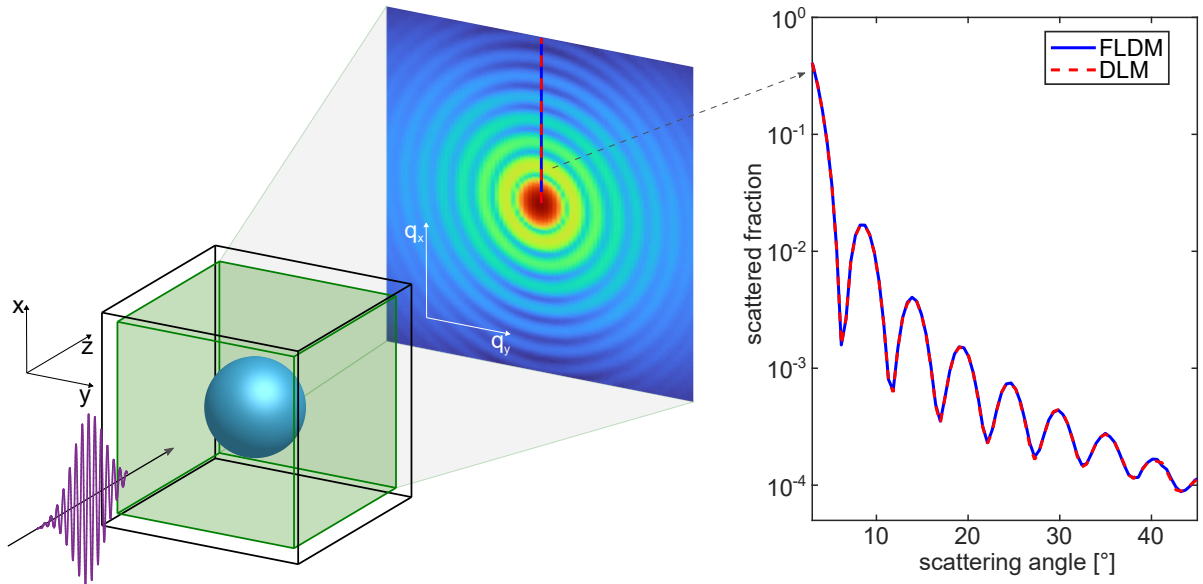


**Figure 3.3.:** Sketch of the scattering simulation setup. A spherical helium nanodroplet ( $R = 300$  nm) is centered inside a cubic arena (black box left). A short incident pulse with a plane wavefront and a temporal Gaussian profile is polarized along the  $x$ -axis and propagates along the  $z$ -axis. The electric fields are sampled on a control surface (green) and propagated into the far-field using the equivalent source method, yielding spectrally resolved scattering images. For  $q_y = 0$ , radial scattering intensity profiles (right) along the  $q_x$  axes for low incident field strength are benchmarked for the FLDM method (blue) and the DLM (red). From [BK2]

## 3.2. Population dynamics and electric fields for nonlinear excitation

Increasing the intensity of the incident pulse, the calculations with the FLDM model show that clear population dynamics take place. In the following, a representative case with  $I = 5 \times 10^{14} \text{ W/cm}^2$  is discussed.

In Fig. 3.4 (a)-(d), snapshots of the ground-state depletion reveal that during the excitation, pronounced moving excitation slabs emerge, their curvature approximately follows the structure of the helium droplet. These excitation waves propagate from left to right through the droplet and are focused at its end. Importantly, the phase fronts of the polarization within the excitation slabs (Fig. 3.4 (e)-(h)) do not show the curved structure, but are flat. Nevertheless, it is still visible as nodes (white areas) of the polarization amplitudes where the population of individual levels is maximal. In these nodes, a phase flip within the polarization occurs, i.e. when populating or depopulating the excited states. When looking at the detailed population evolution in the center of the droplet (Fig. 3.4 (i)), we see clear Rabi-flopping between the ground state  $|0\rangle$  ( $1s^2$ ) and the excited  $1s2p_x$  state  $|1\rangle$  in  $x$ -direction, coupling to the  $x$ -component of the electric field. During the short pulse, multiple Rabi-cycles occur, but their amplitude decreases because of decoherence. This underlines that a short pulse is necessary to realize distinct Rabi-cycling. With a longer pulse and the same pulse energy, the coherence would be gone even before substantial Rabi-flopping appears.

Taking a more detailed look at the polarization in the droplets center (Fig. 3.4 (j)), clear signatures of Rabi-cycling and the associated dressed states can be seen in the form of a signal modulation with the period of the Rabi cycles. This beating structure shows maximal amplitude for equal population of ground and excited state (second green dashed line) and minimal amplitude if one state is dominantly populated. Fourier-transforming the polarization (Fig. 3.4 (k)) shows two distinct spectral peaks that are up- and downshifted from the frequency of the incident field  $\omega_{\text{inc}}$  by the Rabi frequency  $\Omega = \mu E_0$ , where  $E_0$  is the incident field amplitude. These Rabi satellites can be interpreted as a field-induced level splitting (Autler-Townes splitting in sketch 1.9).

Major effects on the scattering images are expected as the polarization directly couples to the scattered electric field. The Rabi-cycling and thus the saturation in addition to the beating, as well as the decoherence are expected to influence the scattered light tremendously. When approaching intensities on the order of  $10^{14} \text{ W cm}^{-2}$ , which are currently already available experimentally (e.g. at FERMI FEL in Trieste), coherent bound state dynamics must be taken into account, at least when the incident frequency is resonant to the transitions.

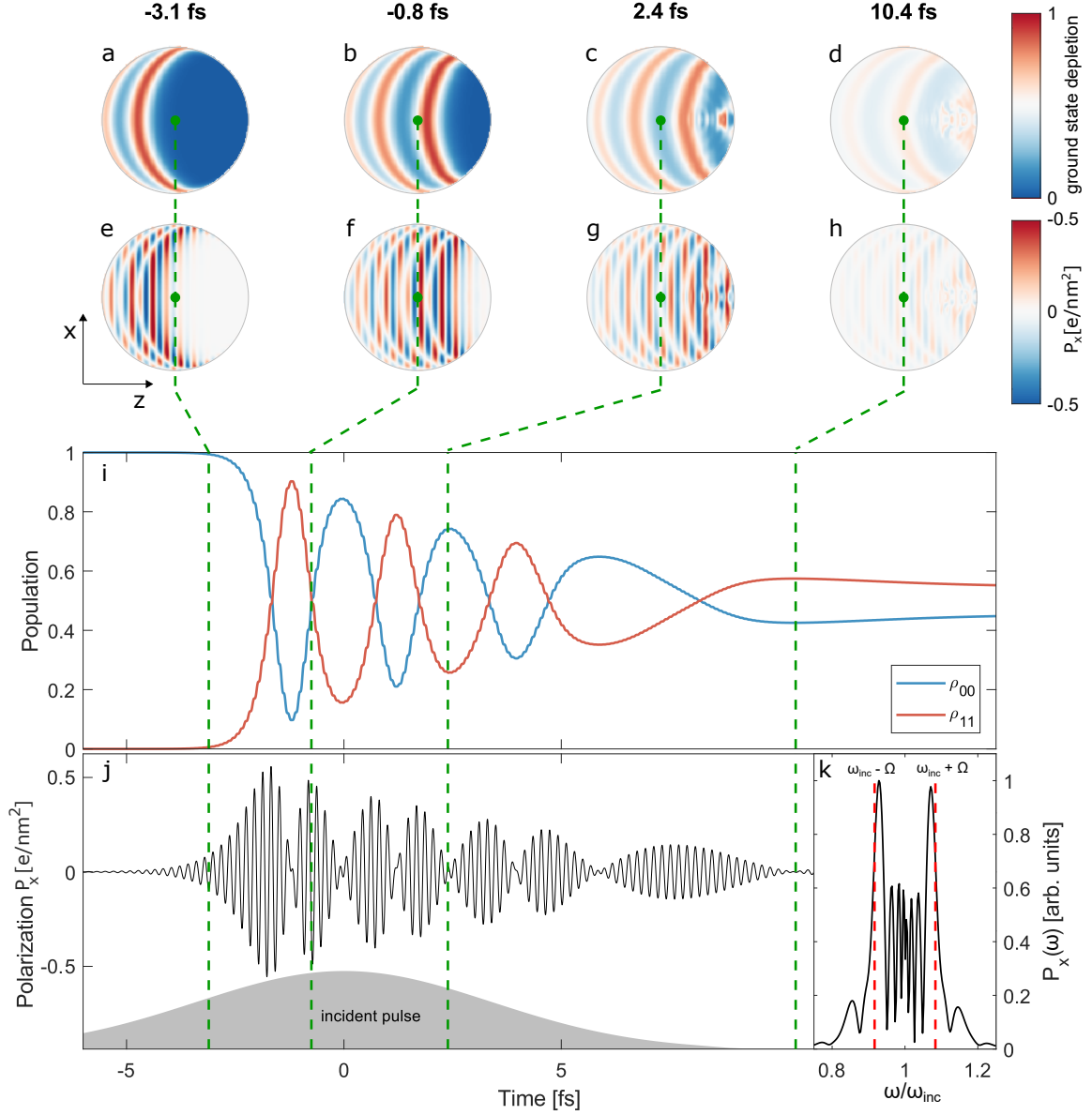


**Figure 3.4.:** Population and polarization dynamics in the He droplet with four bound states ( $1s^2$  and  $1s2p$  levels) when excited with  $5.0 \times 10^{14}$  W/cm<sup>2</sup>. The upper two rows represent cuts in the polarization-propagation plane for four different times during the laser pulse for the population (a)-(d) and the polarization (e)-(h). In the droplets center, the full time evolution of the population (i) and the polarization (j) are taken, where the green dashed lines indicate the position of the snapshots. In the latter plot, the gray shaded area sketches the incident free-space intensity envelope laser pulse at the center. In inset (k), the spectrum from the polarization is depicted, where the spectral splitting can be observed in the form of satellites, shifted up and down from the incident frequency by the Rabi frequency (red dashed lines). From [BK2]

### 3.3. Nonlinear QCDI

In the next step we investigate the structure and evolution of scattering images when transitioning from linear to nonlinear excitation. To this end, three exemplary spectrally integrated scattering patterns are shown in Fig. 3.5 (a)-(c), which exhibit three main features [BK2].

The first feature is a saturation behavior of the total intensity of the scattering images, that can be identified by a decrease of the scattering cross section ( $\propto 1/I$ ) as opposed to a constant cross section for low excitation intensities (see Fig. 3.5 (k)). The intensity, at which this switching occurs (indicated by the dotted lines in (k)), as well as the maximum scattered intensity, depend on the droplets size.

As a second signature, a blurring of the spatial ring structure is identified since their contrast decreases for increasing intensity. Concurrently, Fig. 3.5 (j) depicts how the rings are shifted to larger scattering angles and show a reduced angular decay at high excitation intensities.

Third, the scattered field spectra (see black lines in Figs. 3.5 (g)-(i)) become substantially wider compared to the spectrum when the excitation is linear (i.e. a Gaussian shape). The inelastically scattered radiation components emerging as satellites at  $\omega_{\text{inc}} \pm \Omega$  in the high intensity results correspond to the nonlinear polarization response that was illustrated in Fig. 3.4 (k).

In the following, these three features will be discussed in more detail.

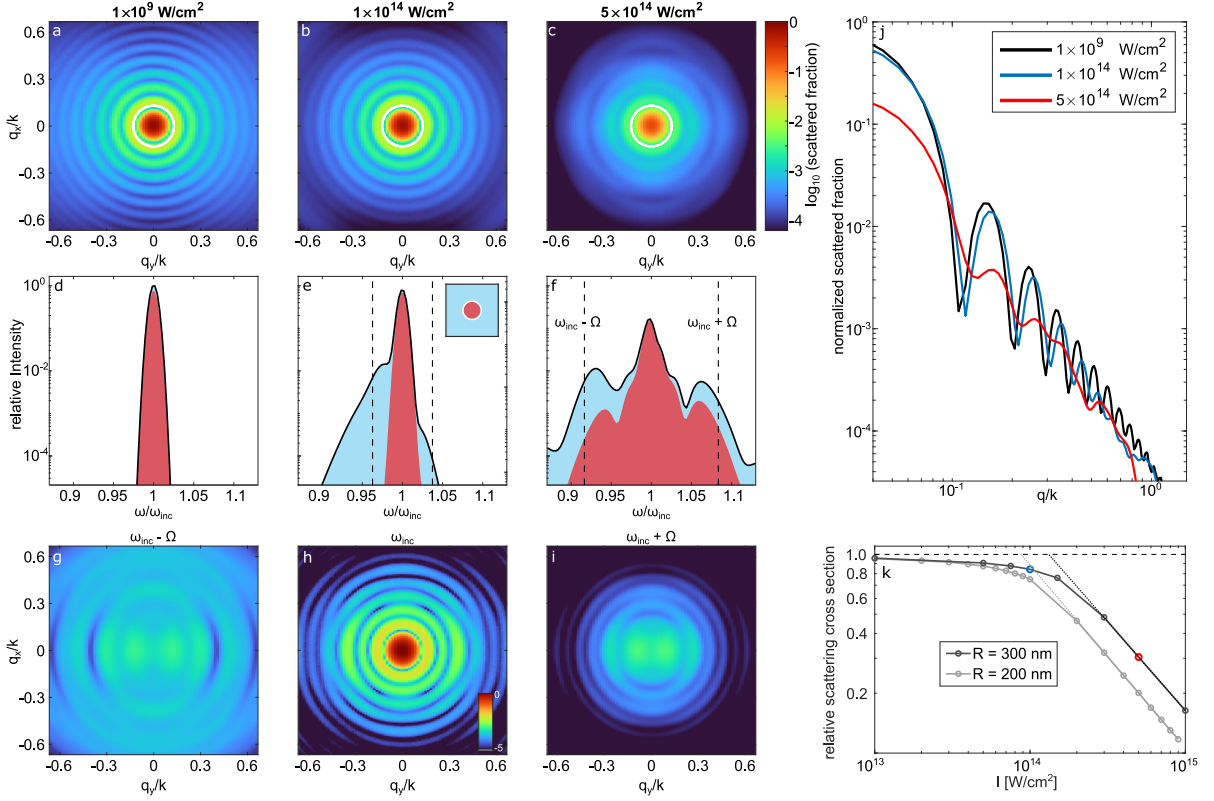


**Figure 3.5.:** Intensity dependence of the scattering patterns for spherical Helium droplets with radius  $R = 300$  nm. Subplots (a-c) display spectrally integrated scattering images for three different XUV intensities, where the scattered fraction was normalized to the center of the linear case (a). Panel (j) shows angular profiles as one-dimensional line-outs along the polarization direction (i.e.  $q_x$  direction,  $q_y = 0$ ). Panels (d-f) show the associated spectra of the scattered fields, where the black solid lines indicate the total spectra and the red/blue shaded areas their respective contribution to small/large angle scattering. The cutoff angle to distinguish between small and large angle scattering is sketched as a white ring in panels (a-c). In panels (g-i) spectrally selected Fourier components of the high intensity pattern of (c) are presented; one at the central frequency  $\omega_{\text{inc}}$  and two at the frequencies of the Rabi satellites  $\omega_{\text{inc}} \mp \Omega$  (g,i). Subplot (k) shows the intensity dependence of the relative scattering cross-section normalized to the linear response result for two different droplet sizes ( $R = 200$  nm and  $R = 300$  nm). Adapted from [BK2]

### 3.3.1. Saturation

In a few-level system, the dipole moment and thus the polarization amplitude has an upper bound. The expectation value of the dipole operator can not exceed the magnitude of the transition dipole matrix element ( $\propto \mu$ ). Consequently the scattered intensity from a laser pulse with a finite temporal width has an upper limit as opposed to the linear scaling from a linear polarization. In terms of relative scattering cross section, this limit can be seen as a reciprocal drop in Fig. 3.5 (k). There we can also identify that the scattering cross section of larger droplet ( $R = 300$  nm) is factor of  $\frac{3}{2}$  larger than from the smaller ( $R = 200$  nm) droplet. This is reasonable because the number of scattering dipoles in the droplet and thus the scattering intensity is proportional to the volume, whereas the cross section (i.e. the scattered fraction) already eliminates the area, leaving only one dimension remaining. The detailed changes in fringe structure, i.e. the change in fringe spacing and a blurring of the scattering image, are less straight forward.

### 3.3.2. Change of fringe spacing

An increase in fringe spacing, which can be seen in Fig. 3.5 (j), is usually connected to a decrease in the spatial dimensions of the scattering object. The dimension of the helium nanodroplets cannot change in the simulations and also not in the very short femtosecond time span of the exciting laser pulse. The reason lies in the nonlinear spatiotemporal change of the optical response of the material. Due to the Rabi-cycling, dressed states are created, which can be considered as an induced transparency. This transparency is strongly linked to the saturation effect discussed before. As the polarization has an upper limit, an increase of the electric field does not increase the response of the medium anymore, so the remaining electric field can just pass through the droplet. Looking at the snapshot of the ground state depletion in Fig. 3.4 (a), the occupation wave just passed around a third of the droplet, making the left side transparent. The remaining part of the droplet (blue area in on the right side) is not yet excited and therefore not transparent. This part is smaller than the total droplet, eventually resulting in a larger fringe spacing in the scattering image.

### 3.3.3. Blurring of ring structure

Two possible contributions can be considered to explain the blurring of the fringe structure. In the linear scattering regime, spectral broadening reduces the fringe contrast in the resulting scattering images [29]. This is due to the fact that the fringe distance (Mie-scattering) scales with the wavelength. Consequently, the mixture of different spectral contributions of the laser pulse yield scattering patterns with varying fringe distance. This mismatch in fringe spacing then leads to a blurring of the total image. With increasing intensity, the nonlinear dynamics induce an increasing spectral broadening (see Fig. 3.5 (d)-(f)), suggesting an increasing blur. However, the relative spectral contribu-

tion of the inelastic signal in Fig. 3.5 (f) is too small (one to two orders of magnitude lower than the central spectral peak) to justify the blurring only by spectral broadening. To this end, a second effect that is related to the structure of the excitation slabs (Fig. 3.5 (a)-(d)) will be analyzed.

To motivate the effect of the excitation slabs, we consider that the droplet is sliced into curved discs with the same thickness and curvature of the excitation slabs. As the train of excitation waves travels through these spatially fixed slices, they emit a Rabi splitted spectrum. If adjacent slices emit incoherently (i.e. without fixed phase relation), the different lateral sizes create differently spaced rings in the scattering pattern, blurring the total image. This argument however requires the inelastically scattered radiation (from the slices) to have a weaker angular decay than the elastic (volume) contribution. Generally, disc-like objects show a weaker angular decay in the scattering intensity than a sphere. Or in other words, the sphere scatters mostly in forward direction, while the disk scatters more into the wide-angle regime. This can be visualized in the limit of the Born approximation [77], where the scattering profiles decay with  $q^{-4}$  for the sphere and only with  $q^{-3}$  for the disc (see Fig. 3.6). In the presence of absorption, these values are of course modified, but the trend should remain, nevertheless.

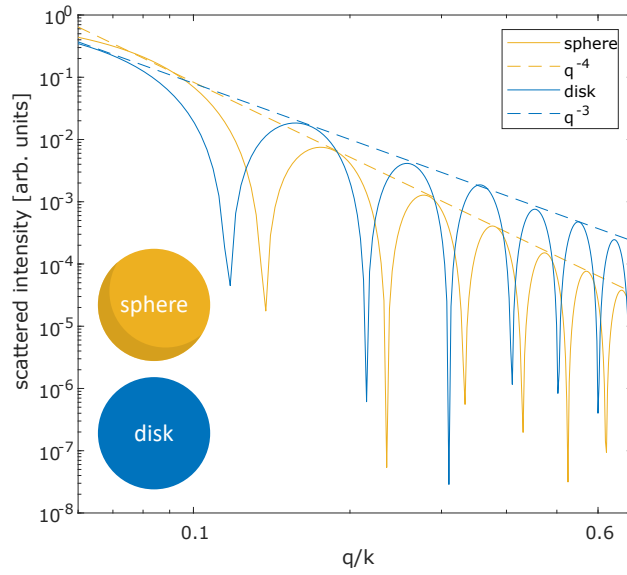


**Figure 3.6.:** Geometry-dependent scattering intensity. In Born approximation, disk-like objects (blue) show a weaker angular decay ( $\propto q^{-3}$ ) than a sphere (yellow), which follows Porod's law [16] ( $\propto q^{-4}$ ).

The integrated scattering signals in Fig. 3.5 (e),(f) show that the scattering images contain both elastic (i.e. central peak) and inelastic contributions (i.e. signal aside from the central peak). The colored areas show the respective contributions to small angle (red) and large angle (blue) scattering. For small scattering angles (forward scattering, red area), the signal is dominated by elastically scattered light. At large scattering angles (blue area), the inelastic contributions are dominant. This is confirmed by the scattering

images associated with the scattered radiation at the central frequency Fig. 3.5 (h), showing a strong signal in forward direction compared to the scattering images at the Rabi satellites (Fig. 3.5 (g),(i)), which display a wide-angle scattering image without that forward peak.

Moreover, there is a spectral asymmetry in the inelastic contribution to the spectrum. At high incident intensity in Fig. 3.5 (f), the low-frequency Rabi satellite is dominant over the high-frequency one. This asymmetry is different for large scattering angles (blue area) than for small scattering angles (red area). One possible explanation could lie in a collective blue shift of the resonance frequency inside the helium droplet - in analogy to the plasmonic shift [27]. Indeed, already the low intensity calculations show that the electric field inside the droplet (see Fig. 3.7 (a)) is absorbed at a higher frequency than the resonance frequency, resulting in an effective absorption peak (Fig. 3.7 b). This absorption peak is located at

$$\omega_{\text{eff}}^2 = \omega_0^2 + f \frac{q_e^2 n_0}{3\epsilon_0 m_e} \quad (3.3)$$

$$= \omega_0^2 + f \frac{\omega_{\text{plasma}}^2}{3} \quad (3.4)$$

where  $\omega_{\text{plasma}}$  is the plasma frequency. This analytical value (dotted line in (b)) matches simulated value very well.

A blue-shifted absorption peak translates into a red-shift of the spectrum of the scattered light as the high frequency components are absorbed and the remaining part of the pulse can scatter. This is confirmed by zooming into the central peak in the high intensity spectrum in Fig. 3.5 (f) where we see that the total scattered light is shifted to a lower frequency (sketched in Fig. 3.7 (c)).

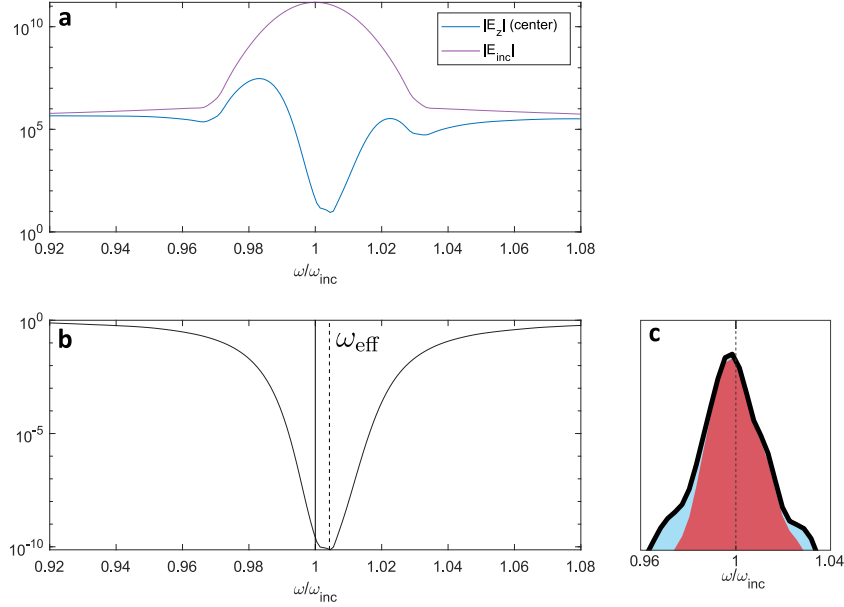


**Figure 3.7.:** Absorption in the helium droplet: Panel (a) displays the spectrum of the electric field in the droplet’s center (blue line) and the corresponding incident electric field (purple line) for the low intensity case (i.e.  $1.0 \times 10^9$  W/cm<sup>2</sup>). Panel (b) shows the ratio of these two fields, where the dashed line indicates the effective resonance frequency  $\omega_{\text{eff}}$ , which is different than the resonance frequency at  $\omega/\omega_{\text{inc}} = 1$  (vertical black line). Panel (c) shows a zoomed in part of the spectrum of the scattering image of the high intensity case (see Fig. 3.5 (f)).

This collective shift of the resonance frequency could be interpreted as a detuning of the resonance frequency to the incident frequency. A detuning during Rabi-cycling translates into a slightly larger Rabi frequency, but most importantly to different heights of the Rabi satellites (c.f. [51], p. 310), i.e. the amplitude of the dipole moment at the frequency of the Rabi satellites

$$\mu_{\text{Amp}\pm} = \frac{\Omega}{2\Omega'} \left( \frac{\Omega' \pm \Delta}{\Omega' \mp \Delta} \right)^{1/2}, \quad (3.5)$$

where  $\mu_{\text{Amp}-}$  indicates the low-frequency peak and  $\mu_{\text{Amp}+}$  the high-frequency peak.  $\Omega' = \sqrt{(\mu\mathcal{E}_0)^2 + \Delta^2}$  is the Rabi frequency and  $\Delta$  the detuning of the incident field to the resonance frequency. A sketch of this behavior is displayed in Fig. 3.8, where a detuning of the incident frequency leads to a larger Rabi frequency and to a higher blue-shifted Rabi satellite, when the incident field is red shifted (c) and vice-versa (a), when the incident light is blue-shifted. The analytical expression from from Eq. 3.5, predict a difference of  $\sim 12\%$  of the Rabi satellites for the dipole moment, when using the detuning from Eq. 3.4.

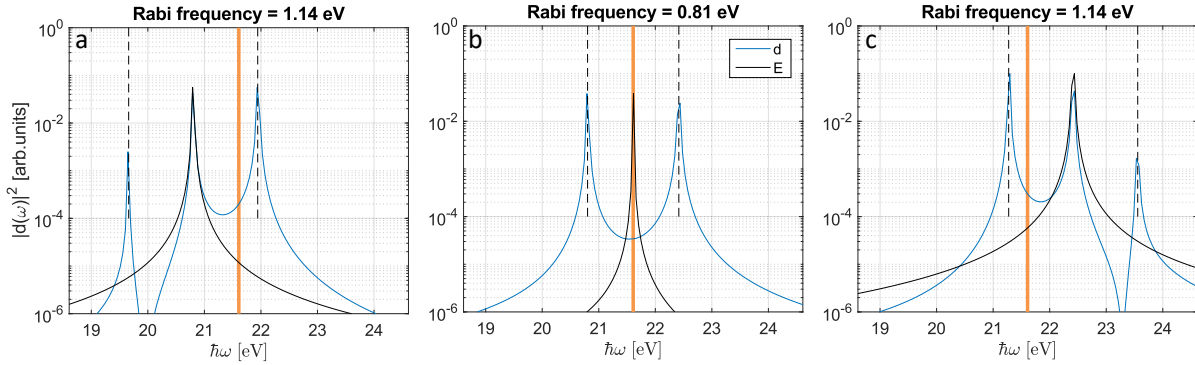


**Figure 3.8.:** 0 dimensional FLDM calculations of the Helium 1s-2p transition ( $\Delta E = 21.6$  eV, indicated by the orange line) for incident electric fields (CW,  $I = 1 \times 10^{14}$  W/cm<sup>2</sup>, indicated by black lines) that are resonant (b) or red-/blue-shifted (a,c) and their resulting induced dipole moment (blue lines). The dashed lines indicate the theoretical Rabi frequency  $\Omega'$ .

However, in the full FDTD calculations for high intensities in Fig. 3.4 (k), the Rabi satellites of the polarization  $P(\omega)$  are nearly evenly high. On the other hand, in the spectrum of the scattering images in Fig. 3.5 (f), the red-shifted peak is around twice as high as the blue shifted peak. Both of these trends do not match the predictions from the analytical considerations. From this we conclude, that it is not the collective shift that leads to an asymmetry in the spectrum, but an interplay of numerous spatiotemporal propagation and interference effects, that have not been analyzed in detail in this work.

Finally, we can conclude that this spectrally selective analysis of the scattering images provides rich information about the underlying spatiotemporal excitation dynamics. Even for this strongly simplified case of a single active transition, the interplay between field propagation and quantum dynamics is challenging to disentangle. The individual patterns, even the elastic one in Fig. 3.5 (h), differ substantially from the linear response result and highlight the importance to include the nonlinear response in the analysis of scattering data. The individual patterns and their fundamental structural differences show that the nonlinear response leaves a pronounced spectral fingerprint in the scattering images.

# 4. Quantum Coherent Diffractive Imaging - Multiple Active Transitions

In the previous chapter 3, substantial differences between the linear and the nonlinear single-transition FLDM simulation could already be observed for a single active bound-electron transition. A logical next step is the incorporation of additional energy levels into the few-level density matrix model and the study of their implications on scattering. To this end, the requirements to extend the model by additional energy levels will be discussed first, followed by the analysis of two scattering scenarios where multiple active transitions play an important role.

## 4.1. Stability analysis of the FLDM FDTD implementation

Technically, the model and how it was derived in chapter 2.2.2 provides everything required to include multiple additional transitions. However, as soon as material equations are coupled to the electromagnetic fields, special attention must be paid to numerical stability and physical consistency. The implementation of linear polarization via the classical Drude-Lorentz model is well established and thus its tabulated parameters are usually in a stable regime (e.g. in [68]). In the FLDM model however, physically unreasonable behavior can be observed under certain circumstances that will be discussed in the following.

### 4.1.1. Instability example from full calculations

To provide a meaningful example of the physically unreasonable behavior, a small cube (2x2x2 grid points) is a convenient choice of geometry. It is small enough to pinpoint the origin of the instability, but large enough that we have enough material to see the instability. Given the layout of the Yee-grid and the spatial averaging needed to evaluate the fields, the fields in a single grid point (1x1x1 cube) do not experience any feedback

from the material polarization. The polarization is modeled by liquid Helium-like few-level systems describing  $1s^2$ ,  $1s2p$  and  $1s2s$  levels and the target is irradiated with a laser pulse resonant to the  $1s^2$ - $1s2p$  transition (21.6 eV). Only the coupling to the polarization direction (here:  $z$ ) is allowed.

During the laser pulse we observe Rabi-cycling in Fig. 4.1 (a) between the ground state and the  $1s2p_z$  level (discussed in chapter 3). Additionally, population is transferred to the  $1s2s$  state via the p-level. After around 22.5 fs the pulse is over and no additional population transfer should take place. However, we observe a population transfer between the  $1s2s$  and  $1s2p_z$  state with the transition frequency of 0.6 eV until both levels are evenly populated. In conjunction with this population transfer, the polarization shows a strong deviation from zero in Fig. 4.1 (b) and zooming in into the polarization after 22.5 fs (c) reveals an exponential increase. This behavior is not physical because the few-level system is driving its own population dynamics with the emitted electric field as the incident pulse is already over. For the stability analysis, a strongly simplified scenario will be considered that gives insight into the origin of the instability, giving us the possibility to quantify the exponential increase of polarization in (c) (gray dashed line). Moreover, possible solutions or workarounds will be discussed.

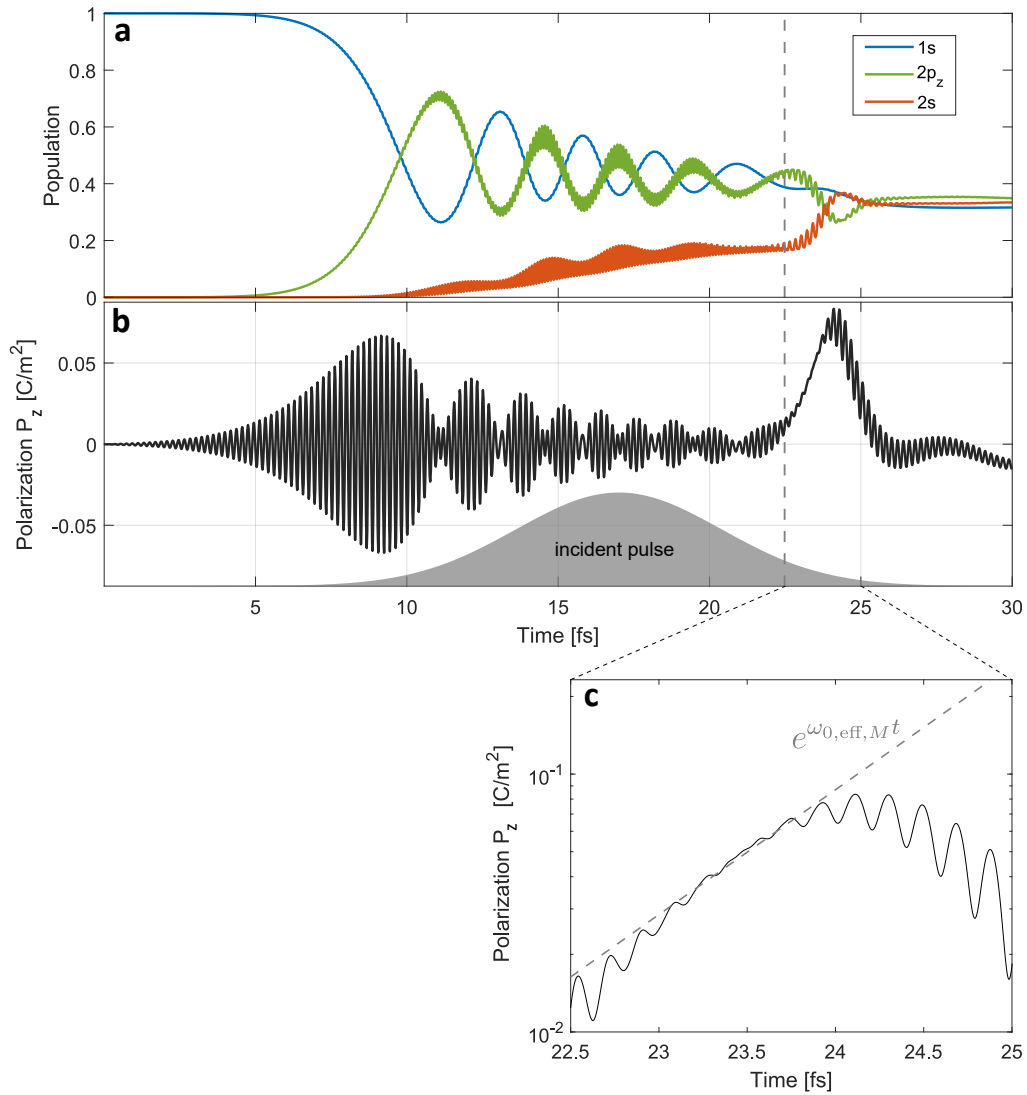


**Figure 4.1.:** Example of numerical instability observed in the FLDM-FDTD simulations. A  $2 \times 2 \times 2$  cube with cells consisting of few-level systems  $1s^2$ ,  $1s2p$  and  $1s2s$  levels is excited with a laser pulse resonant to the  $1s^2$ - $1s2p$  transition. (a) Population of the active states; at 22.5 fs a rapid change in population of the  $1s2s$  and the  $1s2p$  states is observed. (b) The polarization of the few-level system (black line) with the incident pulse intensity (gray shaded area). (c) a zoom of the polarization (black line, semi-logarithmic scale) after 22.5 fs, together with the analytically derived instability (gray dashed line).

### 4.1.2. Analytical stability analysis

As the instability occurs in the 1s2p - 1s2s transition, we focus on a model medium with the density  $n_0$  consisting of two-level systems with a transition frequency  $\omega_{10}$  a dephasing rate  $\gamma_d$  and oscillator strength  $f$ . We start with a simplification of the coupled differential equations (i.e the equations for the polarization and the feedback from the fields).

#### Simplification of full problem

To simplify the analysis, we recall the EOM for the expectation value of the dipole moment (without loss of generality in  $z$ -direction) for a two-level system (Eq. 2.72), where the population behavior is incorporated in the population difference  $w = \rho_{11}^I - \rho_{00}^I$

$$\langle \ddot{\hat{d}}_z \rangle + 2\gamma_d \langle \dot{\hat{d}}_z \rangle + [\gamma_d^2 + \omega_{10}^2] \langle \hat{d}_z \rangle = -w \underbrace{\frac{2\omega_{10}\mu^2}{\hbar}}_{f \frac{q_e^2}{m_e}} E_z(t) \quad (4.1)$$

and for the polarization density  $P_z = n_0 \langle \hat{d}_z \rangle$

$$\ddot{P}_z + \underbrace{2\gamma_d}_{\nu} \dot{P}_z + \underbrace{[\gamma_d^2 + \omega_{10}^2]}_{\omega_0^2} P_z = -w n_0 \underbrace{f \frac{q_e^2}{m_e}}_{:=A} E_z(t). \quad (4.2)$$

For the sake of brevity, the damping constant  $\nu$  and the resonance frequency  $\omega_0$  are substituted. Additionally, a constant  $A$  is introduced which is an indicator for the coupling strength of the polarization to the electric field (i.e. the higher the density or the oscillator strength, the stronger the polarization resulting from an electric field). Moreover, the coupling to the electric field is maximal when either the ground state or the excited state is fully populated ( $w = \pm 1$ ).

To continue with the stability analysis, it is practical to think about the meaning of the field acting on the modeled response. In the classical case of the Drude-Lorentz model, the electric field driving the polarization describes the macroscopic homogeneous field averaged over the volume of the homogeneous material, i.e. the field following from Maxwell's equations and resulting from the FDTD propagation in our application. The external field  $E_{\text{ex}}$  creates a polarization which itself creates a polarization field  $E_P$ , the sum is the macroscopic field  $E_M = E_P + E_{\text{ex}}$ . Another valid interpretation would be to think of the electric field as the microscopic local field  $E_{\text{loc}}$  that generates the force on a single dipole or atom, for example, in TDSE solvers.

In the case of the density-matrix calculations, this question is not as easy to answer. When a single atom is modeled and the response of the valence electron to the applied field is of interest, the field acting on the atom would obviously be the local electric field, meaning that the comparison of the dipole moment from the TDSE calculation to the applied field would lead the atomic polarizability  $\alpha$ . In the FLDM case in this

work, both definitions are eligible: On the one hand, the density matrix formulation was fitted to the macroscopic response of helium and one grid point describes a density of atoms as apposed to a single atom. On the other hand, the evaluated dipole moment is derived from the Schrödinger equation, where the electric fields are the fields acting on the atomic states, which would support the interpretation of the response as the atomic polarizability.

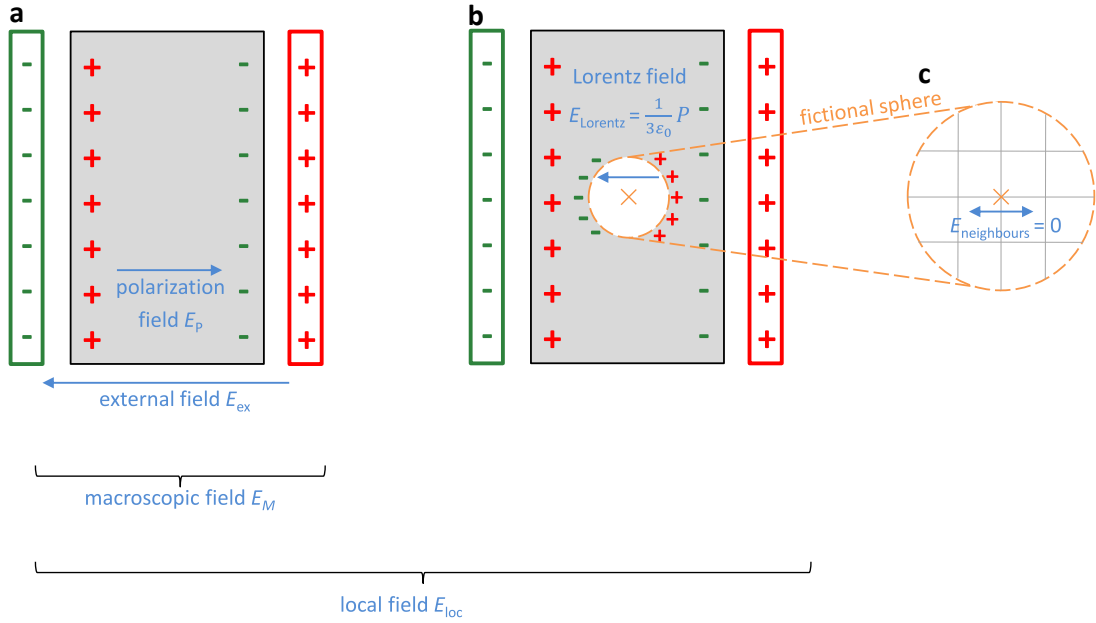


**Figure 4.2.:** Sketch of the contributions to the local electric field in a dielectric. (a) An external field  $E_{\text{ex}}$  is applied to a dielectric (gray area), which induces polarization charges on its surface, leading to the polarization field  $E_P$ , which are together referred to as the macroscopic field  $E_M$ . (b) To investigate the local field  $E_{\text{loc}}$  at a test atom (orange cross), a sphere around it is cut out, leading to the so called Lorentz-field inside the remaining hole (because of polarization charges on the hole's surface). (c) The fields of the neighboring atoms acting on the test atom average out  $E_{\text{neighbours}} = 0$ . Figure adapted from [56] and [78].

We will continue with the case where the local field couples to the material response, because the macroscopic field case can easily be reproduced in this analysis. The definition of the electric fields is sketched in Fig. 4.2. In panel (a), the external field leads to a polarization field, which are together the macroscopic field.

The trick to find the local field at the location of a single test atom, is to cut out a fictional small sphere containing a few ten atoms. Because of the linearity of Maxwell's equations, the field of the the small sphere in (c) and the remaining hole in (b) must add up to the total local field acting on the test atom. The field  $E_{\text{neighbours}}$  describing the fields of the neighboring atoms and ions inside the sphere (c) is usually very small; for cubic crystals or amorphous materials it is actually zero because they average out [56]. The field inside the hollow sphere is given by the field of all other atoms of the material remaining, i.e. the field induced by the polarization charges of the hole. This field is

called the Lorentz-field and has to be added to the macroscopic field

$$\text{and } E_{\text{loc}} = E_M + E_{\text{Lorentz}}. \quad (4.3)$$

The magnitude of the Lorentz-field is the polarization field of a hollow sphere with  $\varepsilon_r = 1$ .

The polarization field is the feedback from the considered geometry and its material response. To simplify the analysis, we consider the electrostatic case, where the polarization field is the field from polarization charges inside a dielectric of a given shape between the parallel plates of a capacitor, i.e.

$$E_P = E_{\text{dielectric}} = -\frac{N_{P,\text{target}}}{\varepsilon_0} P. \quad (4.4)$$

Here,  $N_P$  is the depolarization factor which is dependent on the geometry and describes the deviation of the case where the dielectric would fill the space between the capacitor plates completely. In the case of the hollow sphere we have  $N_{P,\text{Lorentz}} = -\frac{1}{3}$  but noticeably with a negative sign because the hollow sphere is already located inside the polarized material (see sketch 4.2)

$$E_{\text{Lorentz}} = -\frac{N_{P,\text{Lorentz}}}{\varepsilon_0} P = \frac{1}{3\varepsilon_0} P, \quad (4.5)$$

leading to the final local field:

$$E_{\text{loc}} = -\frac{N_{P,\text{target}}}{\varepsilon_0} P + \frac{1}{3\varepsilon_0} P + E_{\text{ex}}. \quad (4.6)$$

Note that this Lorentz-field is directly connected to the so called 'Lorentz-Lorenz-equation' or 'Clausius-Mossotti relation' [79] which both connect the atomic response to the local electric field (i.e. the atomic polarizability  $\alpha$ ) to the macroscopic optical parameters  $n$  (refractive index) or  $\chi$  (the susceptibility), respectively. A comparison is given in Appendix E.

This leaves us with the differential equation where the polarization density is driven by the local field

$$\ddot{P}_z + \nu\dot{P}_z + \omega_0^2 P_z = -wA E_{\text{loc},z} \quad (4.7)$$

$$= -wA [E_{\text{neighbors}} + E_{\text{Lorentz},z} + E_{\text{ex},z} + E_{P,z}] \quad (4.8)$$

$$= -wA \left[ 0 + \frac{1}{3\varepsilon_0} P_z + E_{\text{ex},z} - \frac{N_{P,z,\text{target}}}{\varepsilon_0} P_z \right]. \quad (4.9)$$

Rearranging all polarization terms to the left side leads to

$$\ddot{P}_z + \nu\dot{P}_z + \underbrace{\left[ \omega_0^2 + wA\frac{1}{3\varepsilon_0} - wA\frac{N_{P,z,\text{target}}}{\varepsilon_0} \right]}_{\omega_{0,\text{eff}}^2} P_z = -wAE_{\text{ex},z}, \quad (4.10)$$

where we identified the brackets as an effective resonance frequency  $\omega_{0,\text{eff}}^2$ . For the EOM to have oscillating solution, the frequency needs to be real, i.e.  $\omega_{0,\text{eff}}^2 > 0$ . If this is not the case, we effectively have a negative spring constant leading to an exponentially increasing polarization making the simulation unstable. In the example in Fig. 4.1, the two-level system is coupled to the macroscopic field, such that the second summand in the brackets of Eq. 4.10 vanishes

$$\omega_{0,\text{eff},M}^2 = \omega_0^2 - wA\frac{N_{P,z,\text{target}}}{\varepsilon_0}. \quad (4.11)$$

The simulated polarization in subplot (c) matches the predicted polarization (dashed line)

$$|P| \propto e^{\omega_{0,\text{eff},M}t}, \quad (4.12)$$

with  $w = 0.24$  (the population inversion at 22.5 fs indicated by the gray dashed vertical line in (a)) and  $N_{P,z,\text{target}} = \frac{1}{3}$  (i.e. for a cube). The good agreement with the analytically and the numerically calculated increase of the polarization is a strong indication to the applicability of this analytical stability analysis.

In the particular example of a cube ( $N_{P,z,\text{target}} = \frac{1}{3}$ ) and an incident wavelength which is way larger (factor 10) than the geometry, the local field correction would repair the instability because of the opposite sign (i.e.  $N_{P,z,\text{Lorentz}} = -\frac{1}{3}$ ). For applications outside of this benchmark scenario however, other geometries have a polarization factor that is different from  $\frac{1}{3}$ , even spheres, because in FDTD they are built of cubes, thus not having a perfectly round shape. Additionally, propagation effects will yield a different geometry response as the simplification of a uniform electric field would not be valid anymore. To this end, we have to distinguish stable and unstable cases based on geometry and level population.

### Stable and unstable cases

As the stability criterion for the two-level system when coupling to the macroscopic field (not considering the Lorentz-field) we identified



$$\omega_0^2 - \frac{wA}{\varepsilon_0} N_{P,z,\text{target}} > 0 \quad (4.13)$$

and when coupling to the local field (considering the Lorentz field)

$$\omega_0^2 - \frac{wA}{\varepsilon_0} \left( N_{P,z,\text{target}} - \frac{1}{3} \right) > 0 \quad (4.14)$$

$$\left( \omega_{10}^2 + \gamma_d^2 \right) - wn_0 f \frac{q_e^2}{m_e \varepsilon_0} \left( N_{P,z,\text{target}} - \frac{1}{3} \right) > 0. \quad (4.15)$$

In this expression, the resonance frequency  $\omega_0$  as well as the oscillator strength  $f$  inside the coupling strength  $A$  are dependent on the quantum-mechanical properties of the material.  $A$  is also dependent on the density of the considered material  $n_0$ , the depolarization factor  $N_{P,z,\text{target}}$  depends on the geometry. In the FDTD simulation, the quantum-mechanical material parameter and the density are material specific constants and cannot be changed. This leaves the population inversion  $w$  and the depolarization factor as variables. With this we can identify four cases if we consider the Lorentz field, and two if not:

	$w = +1$ 	$w = -1$ 
With Lorentz-field; $N_{P,z,\text{target}} < \frac{1}{3}$	stable	conditionally unstable
With Lorentz-field; $N_{P,z,\text{target}} > \frac{1}{3}$	conditionally unstable	stable
Without Lorentz field	conditionally unstable	stable

**Table 4.1.:** Stable and unstable cases for the FLDM-FDTD model.

The cases when considering the Lorentz-field show that for a given geometry, for example with  $N_{P,z,\text{target}} < \frac{1}{3}$  (vice-versa for  $N_{P,z,\text{target}} > \frac{1}{3}$ ), the simulation is either unconditionally stable when the electron is in the excited state or conditionally stable, when the electron is in the ground state. For high intensities, both cases will occur or even alternate (Rabi-oscillations). Stability in the conditionally stable cases occurs when the resonance frequency  $\omega_0$  is sufficiently large or the coupling  $A$  (i.e. the oscillator strength  $f$  and the density  $n_0$ ) is sufficiently weak.

Note that these conditionally unstable cases are inherent to the model itself and not to the numerical implementation of the von Neumann equation or its incorporation into the FDTD model. When the Lorentz field is not considered, similar conditionally unstable and stable cases occur, based on the electron population.

As a remark, in the normal Drude-Lorentz-oscillator model the polarization is also only driven by the macroscopic field. For linear cases, the electron is considered to be in

the ground state  $w = -1$  which leads to this stability criterion for the Drude-Lorentz-oscillator

$$\omega_0^2 + A \frac{N_{P,z,\text{target}}}{\varepsilon_0} > 0, \quad (4.16)$$

which is unconditionally stable and verifies the robustness of this well-established model.

Coming back to the example in the previous section 4.1.1, where we assumed helium of density  $n_0 = 0.022 \text{\AA}^{-3}$  and where the 1s2s - 1s2p transition has a frequency of 0.6 eV with an oscillator strength of  $f = 0.39$  we find a coupling constant of  $\frac{\hbar^2}{\varepsilon_0} A = 11.83 \text{ eV}^2$ . This shows that even with large dephasing rates (which are related to the spectral line width) in the order of magnitude of the transition frequency, the stability can never be reached if the levels are that close together and the electron is in the excited state. This is especially problematic because with higher principal quantum number, the states tend to be closer together.

In the analytical derivation of the stability criterion, the depolarization factor was introduced as a tool to estimate the feedback of the electric field. For its application to real simulation scenarios one should keep in mind that it only applies to constant fields thus neglects all propagation and edge effects. Nevertheless, the factor should realistically only be between zero (infinitesimal small needle) and one (plate capacitor).

As a first step in chapter 3, we already considered a helium droplet where the 1s<sup>2</sup> and 1s2p states were active and coupled to the macroscopic field. Because of the large transition frequency and oscillator strength, this scenario was always stable (coupling strength was always smaller than the resonance frequency  $\frac{\hbar^2}{\varepsilon_0} A = 14.86 \text{ eV}^2 < \hbar^2 \omega_{1s^2-1s2p}^2$ ). As soon as there are other transitions active, the possible instability has to be accounted for thoroughly. The considerations on the stability make it clear that, in order to proceed further without heavily adjusting the model, it is essential to find scenarios that are always stable but still physically relevant.

### 4.1.3. Circumventing the instabilities - 2 physically relevant scenarios

For the first scenario, we consider a setup similar to the one in chapter 3, but now with additional p-levels, namely 1s3p and 1s4p, while far off-resonant transitions with small frequencies are neglected (e.g. 1s2s - 1s2p). As the 1s3p and 1s4p state are energetically even further away from the ground-state than the 1s2p state and the oscillator strengths of the transitions to the ground state are also smaller, the simulation will be stable. We expect large population transfers because of high intensity resonant excitation of the system (population inversion between  $-1 \leq w \leq +1$  will be realized). We also apply the Clausius-Mosotti correction as we consider it to be the physically more correct description. The physical relevance of this scenario is given by the fact that there have not yet been any studies of the influence of multilevel transitions on coherent diffractive

imaging. In our model, this is the only way we can access this problem with resonant high intensity excitation.

As a second scenario, we consider a comparatively weak excitation with an XUV pulse, whereby no population dynamics take place. Meanwhile, the target is pumped by a strong NIR pulse, modifying the electronic transitions of the system, just as in attosecond transient absorption spectroscopy [42]. To ensure numerical stability for all geometries, the Clausius-Mosotti correction is neglected (i.e. Lorentz field is neglected). Since the excitation intensity is so small, there is no population inversion, which means that the calculation is always numerically stable - no matter how small the transition energies are. In table 4.1, this corresponds to the scenario in the last line (no Lorentz field) and right column ( $w = -1$ ). This scenario is physically relevant because experiments on helium nanodroplets have already been carried out by our collaborators Daniela Rupp and others in a tabletop HHG CDI experiment where the XUV intensities are around two orders of magnitudes lower than on free-electron lasers [32]. With an NIR laser, transient modifications of the electronic states will influence the scattering images substantially.

## 4.2. Influence of multiple transitions for Quantum Coherent Diffractive Imaging

As discussed in the previous section 4.1.3, we will consider two distinct scenarios to investigate the influence of multiple transitions in helium nanodroplets on QCDI. For the first scenario, we will repeat the calculations of the previous section (large population transfers) but with additional p states while neglecting far off-resonant transitions. Additionally, we now also apply the Clausius-Mosotti correction. In the second scenario, we consider a relatively weak XUV pulse for imaging, that is not able to introduce population dynamics, while the system is electronically modified by a strong NIR pulse. We will however not apply the local field correction to avoid instabilities in the model because the states are so close together.

For the following calculations, the parameters that have been used to describe the electronic structure of liquid helium can be found in table 4.2.

	$\Delta E[\text{eV}]$	$f$	$\mu[\text{D}]$
1s-2p	21.6089 (chapter 3, [BK2] and scenario 1)	0.490	1.412
	21.2216 (scenario 2)	0.259	1.036
1s-3p	23.0910	0.071	0.521
1s-4p	23.7460	0.0312	0.340
2s-2p	0.6022	0.390	7.545
2s-3p	2.4716	0.160	2.386
2s-4p	3.1266	0.051	1.197
3s-2p	-1.7023	0.143	0.143
3s-3p	0.1665	0.625	18.165
3s-4p	0.8218	0.134	3.786

**Table 4.2.:** Helium transitions that were used in this work. Values from [70, 69] (first line) and [80, 81] (others).

In the first scenario, we stick with the energy and oscillator strength values for the 1s-2p transition from [70, 69] that were fitted to measurements on liquid helium to enable a better comparison of the single-transition calculations from chapter 3.

For the second scenario we will use the tabulated values from [80, 81] that provide a self-contained set of parameters.

### 4.2.1. Implications of additional p-levels (Scenario 1: Strong XUV pulse)

The calculations of the high intensity case  $I = 5.0 \times 10^{14}$  W/cm<sup>2</sup> in chapter 3 are repeated, but the 1s-3p and 1s-4p transitions from table 4.2 are now included in the FLDM model.

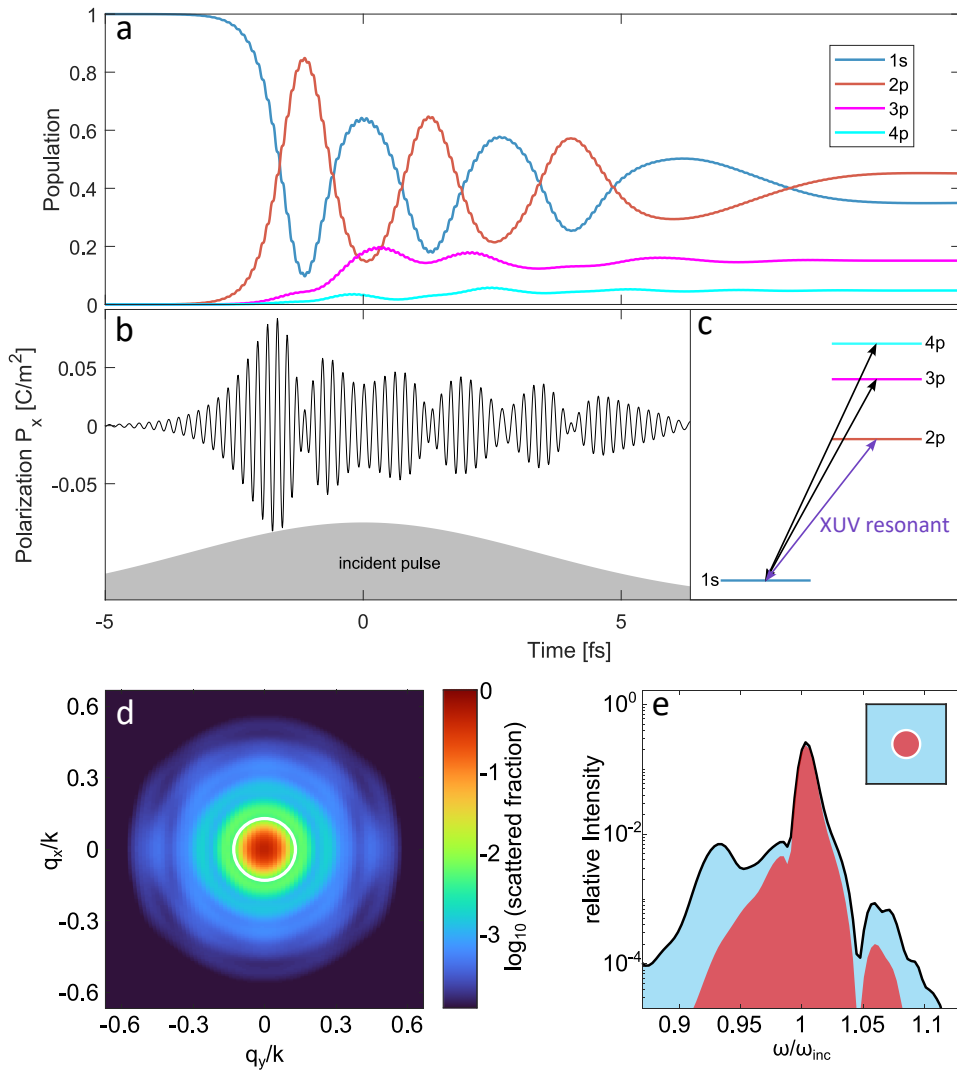


**Figure 4.3.:** Panels (a,b) show the Population and polarization dynamics in a Helium droplet for  $I = 5.0 \times 10^{14}$  W/cm<sup>2</sup> and three active p-states (as indicated in the inset (c)), where the incident light is resonant to the 1s-3p transition. Panel (d) depicts the resulting scattering image and (e) shows the associated spectrum of the scattered fields (black line) and their contribution to small (red area) and large angle scattering (blue area).

The interpretation of the simulated data will follow the comparison with the calculations done with one active transition, i.e. the 1s-2p transition. First, we will look at the population dynamics and consequently the polarization. Second, the changes scattering image in conjunction with the spectral analysis of the scattered light will be compared.

In Fig. 4.3 (a) the population of the ground state 1s and the excited p-states in the doplet's center is shown, where Rabi-cycling between 1s and 2p is once again observed, just as in Fig. 3.4 (i), because this transition is exactly resonant to the incident light. A key difference to the previous calculations however, is the population transfer to the 3p and 4p level, where the former is populated more than the latter. The 3p population changes particularly, when the 1s and 2p state are populated evenly.

Recalling from the previous chapter, this is when the polarization from the FLS is strongest (and with this, the emitted electric field). This is confirmed in Fig. 4.3 (b) where we can observe again the beating structure from the Rabi-cycling in the polarization resulting from the resonantly XUV-driven 1s-2p transition. In frequency space, the spectrum of the scattered light (see Fig. 4.3 (e)) reveals a notch at around  $\omega/\omega_{\text{inc}} \approx 1.05$ , which results from the 1s-3p transition (and also 1s-4p) resonantly driving a part of the blue-shifted scattered light. This creates an imbalance in the blue- and red-shifted parts of the scattered light spectrum.

The scattering image in Fig. 4.3 (d) looks very similar to the two-level case in Fig. 3.5 (c). The main difference can be seen in the relative scattered fraction (i.e. scattered intensity), which is higher by a factor of 1.6. Because the total dipole moment of the few-level system is increased, this leads to a larger scattered intensity which is proportional to the potential energy of the dipole in the field (i.e. the interaction  $H_{\text{int},nm}^S = -\boldsymbol{\mu}_{nm} \cdot \mathbf{E}(t)$ )

$$\frac{\mu_{1s2p} + \mu_{1s3p} + \mu_{1s4p}}{\mu_{1s2p}} = \frac{1.412 + 0.521 + 0.340}{1.412} \approx 1.6. \quad (4.17)$$

Moreover, the contrast in the scattering image is slightly sharper with more levels. We can understand this change from the spectrum (Fig. 4.3 (e)) of the scattered light to explain this trend. The central peak of the spectrum is larger than in Fig. 3.5 (f) and also its relative height compared to the other peaks, suggesting that the non-resonantly driven transitions scatter mostly elastically.

Furthermore, the red-shifted Rabi satellite of the forward scattered light (red area in the spectrum) is less prominent, not even visible as a peak, because the relative contribution of the 1s-2p transition to the scattering image is lower when incorporating additional p-states. This underlines the simplification of the single-transition model in the previous study, where the effects were very prominent, both spatially and spectrally, due to the single possible channel the population could take. Understandably, additional channels wash out the previously isolated features.

The argument that the relative importance of the 1s-2p transition is lowered can be underlined by looking at the population after the incident pulse is over. As can be seen in Fig. 4.3 (a), the population of the 1s and the 2p state at the end of the simulation

are nearly equal again (i.e. around  $\approx 0.4$ ). Due to dephasing, the population transfer cannot be driven coherently anymore, which leads to a convergence towards a uniformly distributed population. As the pulse is only a few femtoseconds long, the pulse is over before the levels are equally populated. This holds if more levels are included in the model and are thus populated over the course of the pulse, effectively reducing the population of the other levels.

### 4.2.2. Transient modification of optical parameters by an NIR pulse (Scenario 2: Weak XUV pulse, Strong NIR pulse)

In this scenario, the Helium nanodroplet is pumped by a strong near-infrared pulse (NIR) and imaged using a weak XUV pulse. Because of the comparably weak XUV pulse, no population transfer to excited states is expected and the response to the XUV field should be linear. However, the strong NIR pulse transiently heavily modifies the optical parameters of the material due to laser dressing, resulting in the shifting of states (Stark effect [33, 82], dynamical Franz-Keldysh effect [83] and light-induced states (LIS [50, 41])). All these effects are incorporated in the density matrix theory for the FLDM-FDTD model.

To analyze the transient modifications of the material properties from the NIR pulse, the common method '*attosecond transient absorption spectroscopy*' (ATAS [84, 42]) is often used. The transient modifications are visible as changes of the absorption spectrum, that reflects a NIR-modified refractive index. This effective refractive index helps the interpretation of the data and can further be used to calculate scattering images analytically (Mie solution [27]) for comparison with the results from the FLDM-FDTD model.

#### Attosecond transient absorption spectroscopy

The general idea to obtain attosecond transient absorption spectra is sketched in Fig. 4.4. The NIR pulse ( $\Delta t = 10.0$  fs,  $\lambda = 800$  nm) excites the helium, which in our case is modeled by a 0-dimensional few-level system with the active transitions noted in table 4.2, except the ones containing the 4p state. A weak and very short ( $I_{\text{XUV}} = 1$  TW/cm<sup>2</sup>,  $\Delta t = 330$  as,  $E_{\text{ph}} = 20.9$  eV) XUV pulse induces a dipole moment  $d(t)$  which decays because of decoherence at the rate of  $\hbar\gamma_d = 0.215$  eV for each transition. Fourier transforming the dipole moment and the local electric field yields the response of the system. To compare the ATAS results to the full FDTD results, the dipole responds to the total electric field  $E(\omega)$ , thus the electric response is the susceptibility (usually one might interpret the electric field impeding on the system as the local field, yielding the atomic polarizability  $\alpha$ , see appendix E)

$$\chi(\omega) = \frac{d(\omega)}{E(\omega)}, \quad (4.18)$$

which can then be used to carry out further calculations.

In this case, scattering patterns are calculated using Mie theory [27] to compare the results to the full calculations. Note, that the very short XUV pulse duration for calculating the effective refractive index is actually unrealistically short for these kinds of experiments. In the simulation however, the short pulse duration enables the calculation of a very broad spectrum in only one calculation. For the actual imaging calculation, the pulse is a little longer (1 fs).

Moreover, the CEP can play a very important role in ATAS studies as transient modifications of the the optical parameters often depend on the instantaneous field strength and also to *which-way interferences* [41] which lead to half-cycle modulations (cf. Fig. 1.3). As this is not the focus of this work we just stay at a fixed CEP and delay for now (i.e. the NIR field is a cosine).

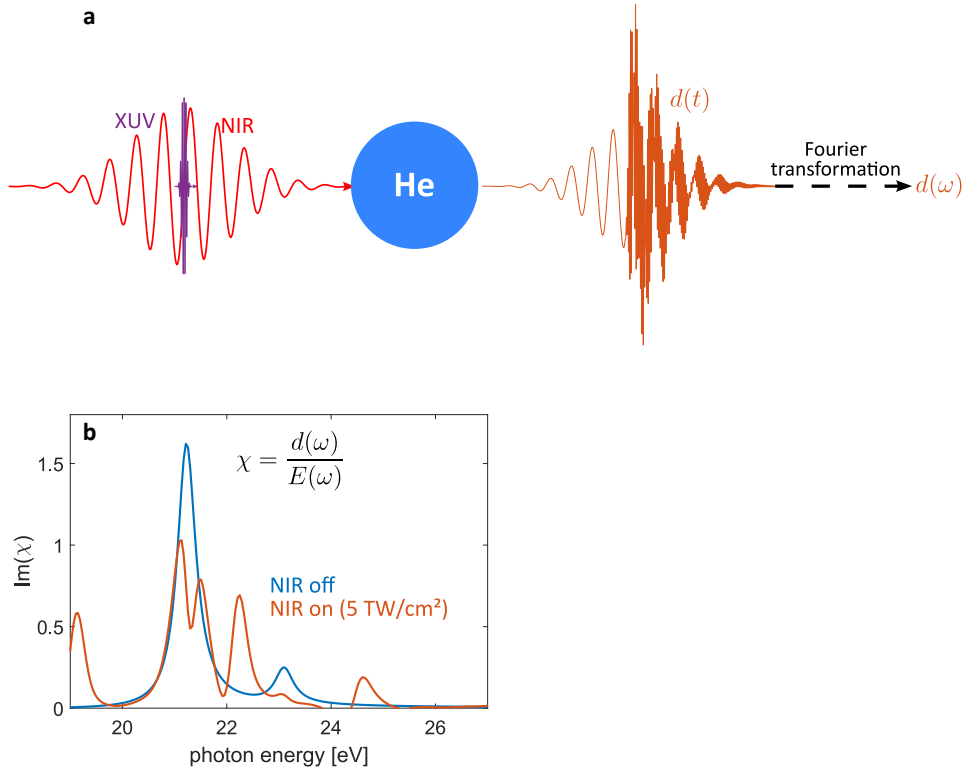


**Figure 4.4.:** Sketch on how to obtain effective optical parameters from a 0D FLDM calculation: (a) The Helium few-level system is excited by a NIR pulse ( $\lambda = 800$  nm;  $\Delta t = 10$  fs) and probed with a very short XUV pulse ( $E_{\text{ph}} = 20.9$  eV;  $\Delta t = 330$  as;  $I_{\text{XUV}} = 1$  TW/cm<sup>2</sup>). The induced dipole moment  $d(t)$  is Fourier-transformed to obtain the spectral response (b), i.e. the susceptibility  $\chi(\omega)$ . If the dipole interacts with the local electric field, one obtains the atomic polarizability  $\alpha(\omega)$  instead.

The effective optical parameters were calculated for NIR Intensities up to 10 TW/cm<sup>2</sup>. Due to the very short XUV pulse, one calculation is performed for each NIR intensity at a fixed carrier envelope phase (CEP) of the NIR, leading to map of NIR-intensity and XUV-frequency dependent refractive indices  $n = 1 - \delta + i\beta$  in Fig. 4.5 (a,b). For NIR only (i.e. 0 TW/cm<sup>2</sup>) the dipole allowed transitions transitions are visible in the spectrum (1s-2p and 1s-3p) as pronounced peaks.

With increasing NIR intensity we observe several new spectral features:

- new spectral lines, e.g. an absorption line slightly above 22 eV
- shifts of spectral line position, e.g. a downshift of the 1s-2p absorption line at 21.6 eV down to around 21 eV
- change in line strength, e.g. a decrease of the 1s-3p absorption line at 23.1 eV.

In our chosen imaging setup, the second effect, happening just below the the 1s-2p absorption line due to the Stark effect is of most significance as the imaging XUV pulse is located at this spectral position (20.9 eV, white dashed line in Fig. 4.5 (a,b)). The NIR intensity dependent refractive index at 20.9 eV is sketched in Fig. 4.5 (c) where a strong increase of the imaginary part together with a slight increase of  $\delta$  is observed. This NIR intensity dependent refractive index will now be used to calculate scattering images using Mie theory to compare them to the results directly from the FDLM-FDTD simulation.

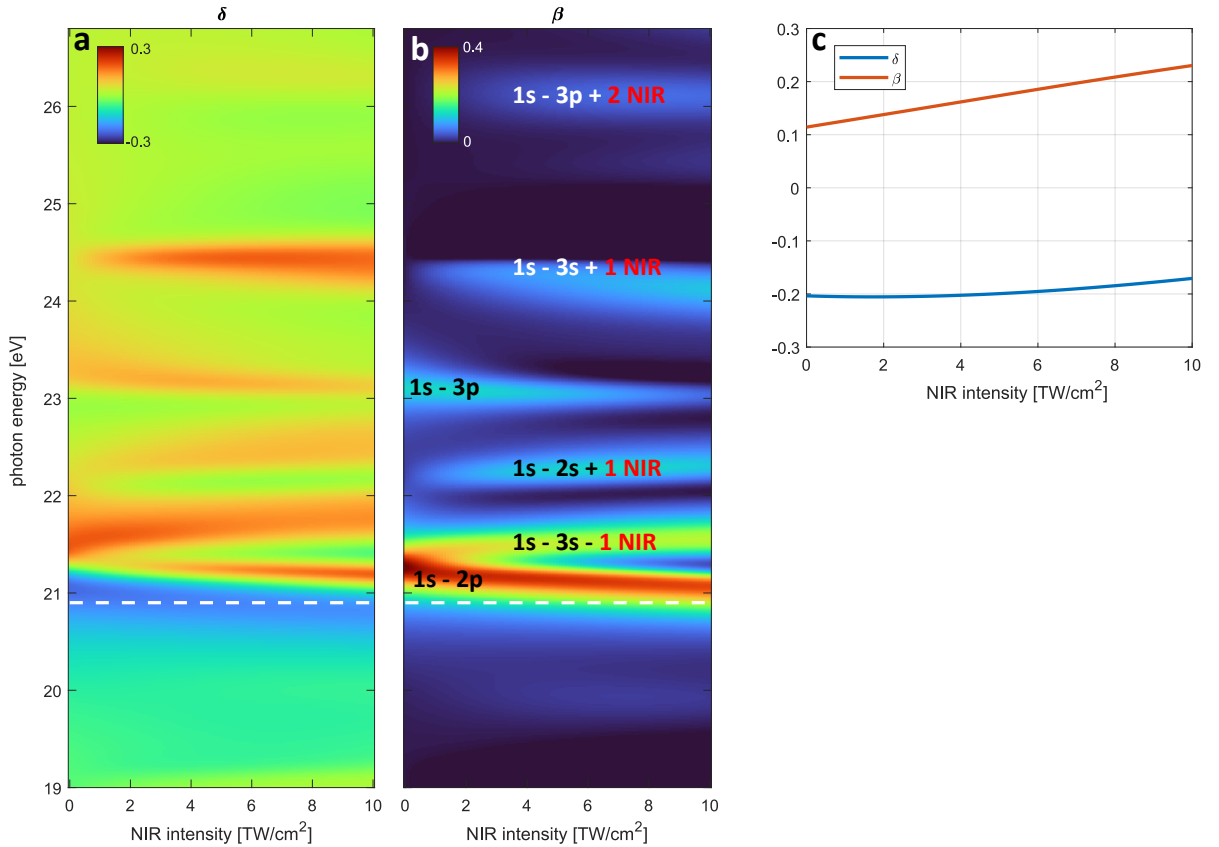


**Figure 4.5.:** NIR Intensity dependent refractive index of helium  $n = 1 - \delta + i\beta$ ; (a)  $\delta$  and (b)  $\beta$ , simulated using the FLDM method sketched in Fig. 4.4. Significant features are labeled by the name of the electronic transition (e.g. 1s-2p resonance) and the involved NIR photons contributing to the spectral line (e.g. 1s-2s + 1 NIR: light-induced state, only reachable with the absorption of one NIR photon). Panel (c) shows the effective refractive index at 20.9 eV resulting from a cut through the spectral map (dashed white lines in (a,b)).

### Scattering images of transiently modified Helium droplets

Scattering images were calculated for small ( $R = 100$  nm) Helium nanodroplets with the full FLDM-FDTD method, using a slightly longer XUV pulse ( $\Delta t = 1$  fs) to limit the dispersion of the imaging pulse near the resonance while still having a short enough pulse to have a nearly constant NIR field strength when overlapping both pulses. The scattering image was then evaluated at a single frequency (i.e. 20.9 eV) to limit the influence of spectral modifications to one frequency. For comparison, Mie calculations were performed for the same XUV photon energy using the effective refractive index from the previous section (c.f.  $\delta$  and  $\beta$  from Fig. 4.5 (c)). The resulting scattering images from both methods are displayed in Fig. 4.6.

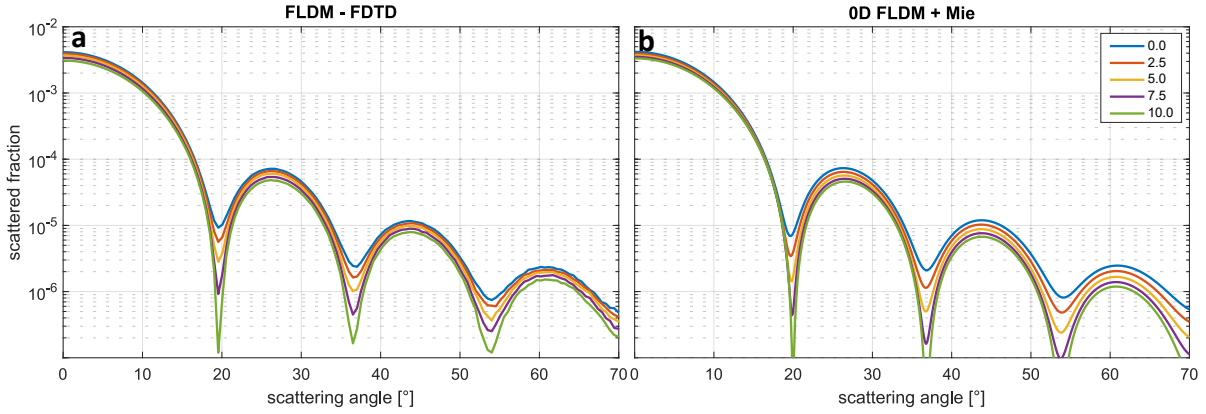


**Figure 4.6.:** Cuts in polarization direction of scattering images of helium nanodroplets ( $R = 100$  nm), in dependence of NIR pulse intensity (as indicated in the legend in  $\text{TW}/\text{cm}^2$ ) using (a) the full FLDM-FDTD method and (b) the effective refractive index from a 0D FLDM ATA calculation and Mie theory

They show pronounced minima and maxima stemming from the ring-like structure typical for spherical scatterers. With increased NIR intensity, the total scattered fraction decreases (as sketched in Fig. 4.7) and the ring contrast (i.e. the difference between maxima and their neighboring minima in Fig. 4.6) increases. Qualitatively, this holds true for the full calculation (a) and also for the Mie calculation (b), while the decrease in scattering intensity is stronger for the latter. The very good qualitative agreement between the two models confirm the applicability of our full model.

Differences can possibly originate from the temporal structure of the XUV pulse in the FLDM-FDTD calculation. As the photon energy is very close to the resonance, the group dispersion is expected to be high and lead to a temporal mismatch between pump and probe pulse. Moreover, the full model includes all sub-cycle effects when the pulses overlap, which can't be accounted for in the 0D FLDM + Mie model.

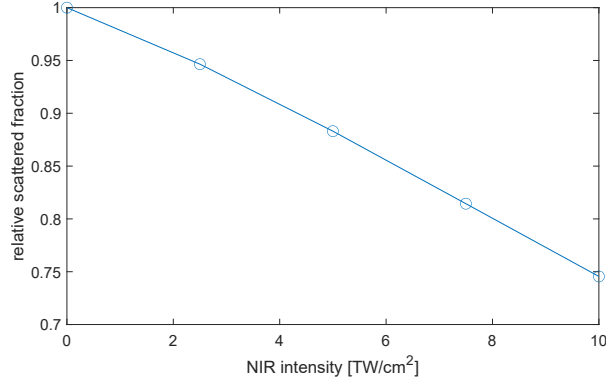


**Figure 4.7.:** Total scattered fraction from integrating scattering patterns calculated using the FLDM-FDTD model; normalized to the XUV only case.

An advantage of the effective optical parameter model is however, that we can attribute the changes in the scattering image to changes in the refractive index and investigate the role of the real and imaginary part separately. To this end, the Mie calculations were repeated, but with  $\delta$  or  $\beta$  being fixed at the value for no NIR pulse (i.e. the leftmost value in Fig. 4.5 (c)).

Cuts through scattering images for a constant real part are shown in Fig. 4.8 (a). They look qualitatively similar to the results where both  $\delta$  and  $\beta$  are changed (c.f. Fig. 4.6 (b)). The NIR intensity dependent decrease of scattering intensity is weaker for a constant  $\delta$  compared to the case where  $\delta$  changes. Nevertheless, the trend remains the same, as well as the increase in fringe contrast. This is reasonable, because  $\beta$  increases with increasing NIR intensity. As  $\beta$  is accountable for the absorption, an increase will, to first order, lead to less scattered light. The fringe contrast increases as the droplet becomes more and more opaque which leads to the real part of  $n$  becoming less important if the light is just absorbed instead of scattered (the limit being a totally opaque sphere).

If  $\beta$  is held constant and  $\delta$  increases slightly (this means that the real part of  $n$  ( $\text{Re}(n) = 1 - \delta$ ) actually slightly decreases), the evolution of the cuts through scattering patterns changes (shown in Fig. 4.8 (b)). As the absorption is not modified, the fringe contrast stays constant, confirming the interpretation above. Moreover, the ring distance increases slightly with increasing NIR intensity and the total scattered fraction decreases. As the real part of  $n$  is responsible for the scattering strength and decreases, the decrease of scattered fraction is reasonable. The structural change is understandable as well, as the change in phase velocity from a varying  $\delta$  will lead to different interference behavior in the far field.

Apparently, the effects from the changing  $\beta$  are more important for the total scattering image, as the trend in Fig. 4.8 (a) resembles the full picture from Fig. 4.6.

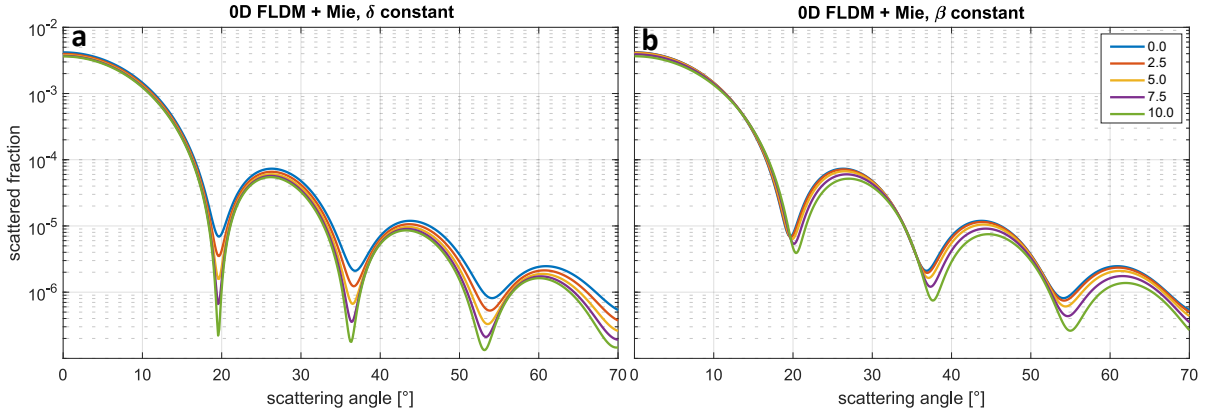


**Figure 4.8.:** NIR intensity dependent (as indicated in the legend in  $\text{TW}/\text{cm}^2$ ) cuts through scattering images using Mie theory, where in (a)  $\delta$  and in (b)  $\beta$  is fixed at the XUV only (i.e.  $I_{\text{NIR}} = 0 \text{ TW}/\text{cm}^2$ ) value.

The results show that the FLDM-FDTD model can describe the transient modifications of bound states very well and the resulting scattering patterns contain rich information on those modifications. While the full model also contains spatiotemporal modifications, like sub-cycle dynamics, group velocity dispersion for the XUV and refraction effects for the NIR pulse, these were not included in the simpler 0D FLDM ATA model. Nevertheless, this simple model together with analytical Mie calculations can help identify the effect of the NIR pulse on the optical properties of the scatterer and its implications for scattering patterns.

### 4.3. Omitted effects

Even with additional levels considered, there are multiple potentially relevant effects that were left out in the multilevel model which may eventually play a role in experiments.

#### Spontaneous emission

In our model we neglected spontaneous emission, which is related to the spontaneous emission time of the excited states. Especially for Scenario 2 (weak XUV + NIR), there will not be any effect of spontaneous emission as no significant population of excited states is happening. For the first scenario (strong XUV), spontaneous emission could potentially play a role as it sets a fundamental limit to the duration of one Rabi cycle. Spontaneous emission is incorporated in the model via the relaxation rate  $\gamma_r$  and related to the lifetime of the respective excited state  $T_1$ . At least for atomic helium, the Einstein coefficient for the  $1s^2$ - $1s2p$  transition is  $A_{ki} = 10.027 \text{ ns}^{-1}$  [85] which is on a longer timescale than the femtosecond dynamics during the observed scattering processes. Additionally, ultrafast relaxation dynamics in Helium nanodroplets accompanied by bubble formation has been reported [86], but this dynamics, despite being named 'ultrafast', still happens on the timescale of  $\sim 1$  picosecond.

#### Ionization

At higher intensities (scenario 1) one-photon ionization from the excited states and two-photon non-resonant ionization from the ground state can influence the bound-electron dynamics. This additional loss channel will lead to plasma generation. One consequence is less efficient Rabi-cycling similar to how the additional  $3p$  and  $4p$  level lowered the efficiency of the Rabi cycling between the ground state and the  $2p$  state (see section 4.2.1). Unlike the additional bound state, however, the continuum states can not interfere with the excited state (because they are spatially not longer the location of the atom). In scenario 2, no significant influence from photoionization is expected because of the low XUV intensity. The interaction with the NIR laser could potentially lead to tunnel ionization, but for an ionization potential of  $24.6 \text{ eV}$  the tunneling rate is very low and negligible for intensities up to  $10 \text{ TW/cm}^2$  [87].

#### Interatomic (or intermolecular) Coulombic decay (ICD)

While local electron decay processes are incorporated in the FLDM model via the relaxation rate  $T_1$  (however, without subsequent ionization like Auger-decay [88]), nonlocal phenomena like interatomic Coulombic decay were observed in doped helium nanodroplets [89] on the order of  $1$  picosecond. ICD is characterized by the de-excitation of a valence excited atom and the subsequent excitation and ionization of a neighboring atom by the energy of the decay. In contrast to the similar intraatomic/intramolecular

Auger decay, ICD is highly dependent on the interatomic distance and can dominate over local decay channels if their de-excitation is energetically not possible [90].

# 5. Origin of Strong-Field Induced Low-Order Harmonic Generation in Amorphous Solids

The research for the content of this chapter was done in a collaboration with the group of Prof. Dr. M. J. J. Vrakking at the MBI Berlin, namely with Alexandre Mermillod-Blondin and his doctoral student Peter Jürgens who conducted the experiment. The theoretical calculations, in which I took part in were done in close collaboration with Benjamin Liewehr. The results have been published in [BK3] and are the basis of the following chapter, where I focus more on the theoretical background of this work.

## 5.1. Harmonic generation in solids

Controlling the interaction of strong laser fields with matter is vital for many applications, ranging from high harmonic light sources [91, 92, 32] to laser-machining [93, 94, 95]. To gain insights into the underlying non-reversible electron excitation dynamics, one particular promising route is to examine the concomitant optical response signal. In solid dielectrics, nonlinear optical phenomena after excitation by an intense infrared laser field can emerge fully reversibly due to quasi-instantaneous Kerr-type interband polarization [51]. This virtual conduction-band population [96] is accompanied by a real sub-cycle interband excitation of the charge carriers from the valence into the conduction band via strong-field ionization (see step 1 in Fig. 5.1). The electrons in the conduction band are then accelerated by the oscillating laser-field (step 2) and can recombine with the hole left behind in the valence band (step 3). In analogy to atomic high-harmonic generation in gases [97, 98, 99], this recombination can lead to emission of high harmonics [100, 101]. In contrast, the harmonics created in the second step by the anharmonicity of the conduction and valence bands have no direct analog in atomic HHG [102].

The pivotal nonlinear response and the resulting harmonics emerging from the sub-cycle injection dynamics into the conduction band (step 1), however, has been considered in the gas phase by F. Brunel [103]. These Brunel harmonics are associated with the step-wise injection of electrons in the continuum by tunnel ionization. As the electron population is increased at each laser half-cycle, the electron population in the continuum

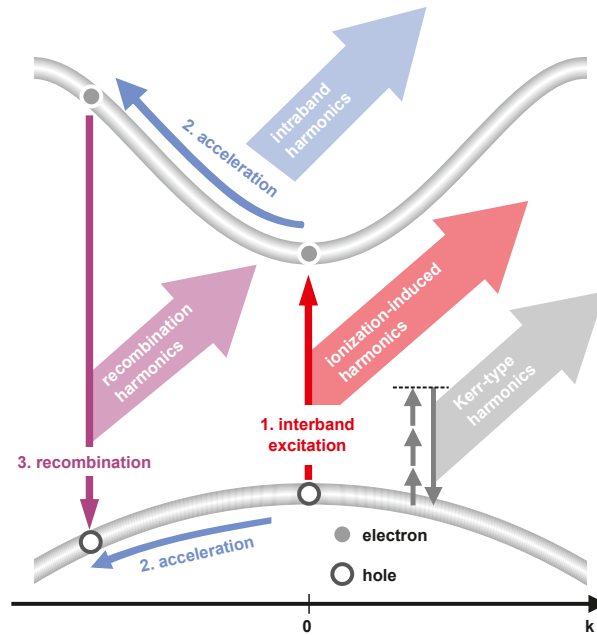


**Figure 5.1.:** Sketch of processes for harmonic generation in solids. First, the electron is promoted to the conduction band by strong-field ionization (1. interband excitation), accelerated in the conduction band together with the remaining hole in the valence band (2. intraband acceleration) and eventually both recombine in the last step (3. interband recombination). Each of these steps comes with distinct nonlinear response and consequently contribute to the total harmonic emission. They all compete with the perturbative Kerr-type response (gray arrows). From [BK3]

in temporally modulated. This temporal modulation during the acceleration by laser fields gives rise of Brunel harmonics. They show a steep fall-off with increasing harmonic order (no plateau), which is why they are also called *low-order harmonics*. The current injecting the electrons was however not considered as a source for harmonics and leaves the question of how relevant it is compared to the other previously mentioned nonlinearities near the damage threshold of the material.

The idea to methodically find an answer to this question is to use a strong mid-IR pump laser and a weak NIR probe to gain time resolution due to nonlinear wave mixing. Most importantly, the laser polarization will turn out to be key to measure the effective nonlinearity of the underlying process, giving us the possibility to show via simulations, how the harmonics from charge injection dominate over those from other mentioned mechanisms. Moreover due to the long wavelength of the incident light, we can use the tunneling picture to describe ionization into the conduction band. Our target is amorphous fused silica ( $\text{SiO}_2$ ), which has a wide bandgap and is transparent for the low-order harmonics of our laser.

## 5.2. Time-resolved measurement of low-order two-color harmonics

In the experiment performed by our partners a strong mid-infrared pump pulse ( $\lambda_{\text{pump}} = 2100 \text{ nm}$ ,  $\tau_{\text{pump}} = 140 \text{ fs}$ ) is overlapped with a weak near-infrared probe pulse ( $\lambda_{\text{probe}} = 800 \text{ nm}$ ,  $\tau_{\text{probe}} = 45 \text{ fs}$ ,  $I_{\text{probe}} = 0.015 \text{ TW/cm}^2$ ) in a  $500 \mu\text{m}$  thick amorphous  $\text{SiO}_2$  plate (a- $\text{SiO}_2$ ). Both beams were focused nearly collinearly, but still at an angle of  $\alpha_{\text{pump-probe}} = 5^\circ$ , at which only mixing orders that contain one single probe photon are detected (see Fig. 5.2 (a) and inset (b)).

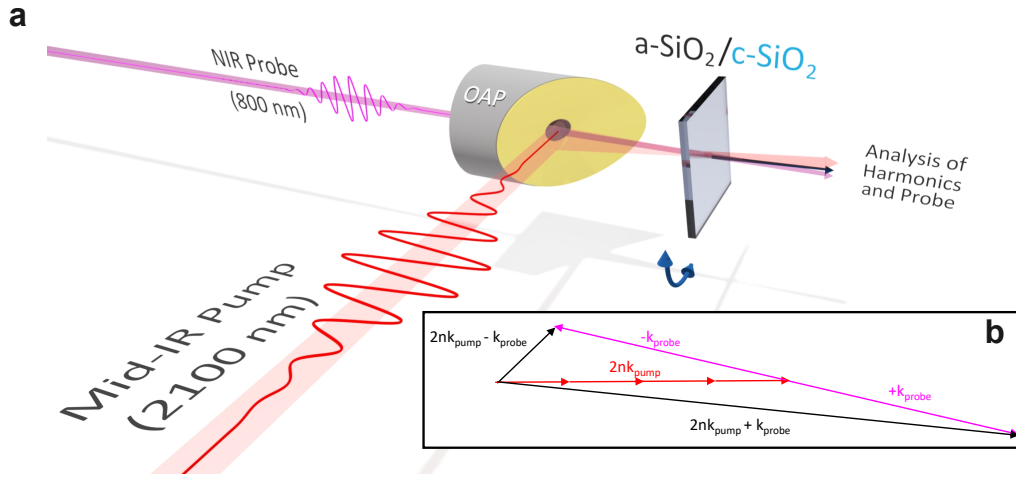


**Figure 5.2.:** Sketch of the experimental setup (a) for the measurement of low-order two-color harmonics. A strong mid-infrared pump laser pulse is focused together with a time-delayed weak near-infrared probe laser pulse into an  $\text{SiO}_2$  sample (both amorphous and crystalline). As the harmonic sum frequency signal is separated spatially from the difference frequency signal (b), the former is analyzed with an optical-to ultra-violet spectrometer while the probe itself is analyzed simultaneously in an NIR spectrometer. Figure adapted from [BK3]

Note that the wavelengths have been chosen such that wave-mixing signals in the harmonic spectrum are separated. The main varied experimental parameters are the pump intensity, the pump-probe delay and the polarization between pump and probe beam. Further details about the experimental subtleties can be found in [BK3].

The low-order harmonics are emitted in the visible and ultraviolet spectral range and the harmonic spectra are measured as function of the pump-probe delay (see Fig. 5.3). At temporal overlap, the harmonics are observed at wave-mixing frequencies of

$$\omega_n = 2n\omega_{\text{pump}} + \omega_{\text{probe}}, \quad (5.1)$$

where  $n$  denotes the (integer) wave-mixing order. Because of the inversion symmetry of the sample, no signal is observed with an even number of photons. The small angle between pump and probe beam leads each harmonic being emitted at different angles. The absence of wave-mixing signal containing difference frequencies in the measured

spectrum (see Fig. 5.2 inset (b)) is due to the large resulting angle at which sum and difference frequencies are emitted. In the sketch Fig. 5.2 (b), the sign of the wave vectors matches the sign of the contributed frequency to the wave-mixing. Multiple pump photons can contribute (red arrows), but only one probe photon (pink arrows). As the angle between the two incident beams is quite small (i.e.  $5^\circ$ ), the signal containing the sum frequency ( $2nk_{\text{pump}} + k_{\text{probe}}$ ) is very close to the optical axis of the pump beam, whereas the difference frequency generation ( $2nk_{\text{pump}} - k_{\text{probe}}$ ) is affected stronger and thus is emitted in a totally different angle (violet arrows). Moreover, the direction of the sum frequencies is only weakly dependent on the number of pump photons, i.e. adding a few more red arrows in the sketch would only change the resulting angles slightly, but not the overall trend. In the experiment only the sum frequency generated harmonics could be analyzed in the detector due to limited angular resolution.

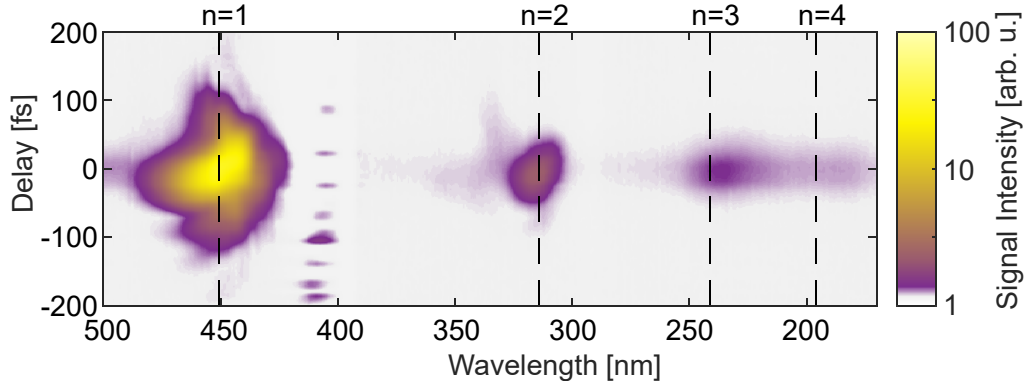


**Figure 5.3.:** Selected experimental delay-dependent harmonic spectrum with the first four harmonic orders ( $n = 1, 2, 3, 4$  indicated by dashed lines) for parallel pump/probe polarization configuration; pump intensity  $I_{\text{pump}} = 12 \text{ TW/cm}^2$ . Similar spectra have been measured for multiple pump intensities and also for perpendicular polarization configuration. From [BK3]

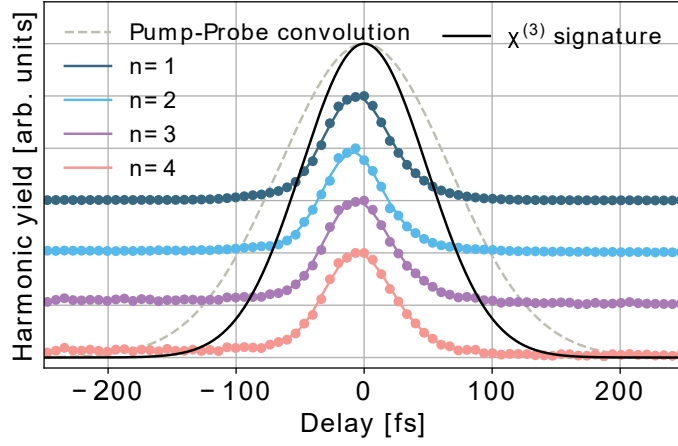


**Figure 5.4.:** Cuts along the delay axis through the delay dependent harmonic spectrum from Fig 5.3 (dashed lines) displayed as colored curves, offset for clarity. They all have the same temporal width of  $\approx 67$  fs. The black line represents the expected  $\chi^{(3)}$  response. From [BK3]

To identify the origin of the observed harmonics, we first have to rule out other conceivable mechanisms for low-order harmonic generation. The first wave-mixing mechanism to exclude is the perturbative Kerr-type interband polarization (gray arrow in Fig. 5.1), also often referred to as  $\chi^{(3)}$ -response with the polarization:

$$\mathbf{P}_{\text{Kerr}} = \varepsilon_0 \chi^{(3)} |\mathbf{E} \cdot \mathbf{E}| \mathbf{E}. \quad (5.2)$$

This mechanism would go hand in hand with the dominant  $n = 1$  contribution for  $I_{\text{pump}} = 12 \text{ TW/cm}^2$  in Fig. 5.3. However, when taking cuts along the delay axis through the harmonic peaks (dashed lines), we realize that their temporal profiles (see colored lines in Fig. 5.4) are all shorter than the signature we would expect from a  $\chi^{(3)}$  response (black curve). For wave-mixing processes of arbitrary order a shorter delay-dependent signal translates to higher nonlinear order of that process, with the probe pulse being the lower bound for the signal duration (details on this can be found in the supplementary information chapter 2 in [BK3]). This indicates, that the observed harmonics are not due to the  $\chi^{(3)}$  response of the medium. Additionally, all harmonics observed have actually the same delay dependence and with the previous argument, it follows that they originate from a common non-perturbative nonlinear process with a nonlinear order higher than three.

It was confirmed by plasma diagnostics, that indeed an electron-hole plasma is formed transiently near the damage threshold. The transmission loss of the sample was measured (Fig. 5.5) to be around only 6%, reaching its maximum at around 150 fs, indicating that the generated plasma is undercritical, ruling out coherent wake emission (which is usually only known from dense plasmas [104]) as a mechanism responsible for harmonic generation. This observation of undercritical plasma buildup below the damage threshold is in agreement with previous reports ([105]). Note, that the pump-intensity dependent, temporal asymmetry present in the absorption measurement in Fig. 5.5 would

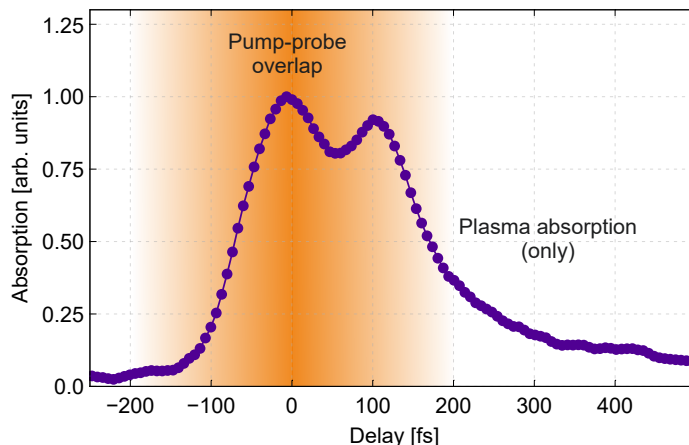


**Figure 5.5.:** Delay-dependent probe absorption for a pump intensity of  $I_{\text{pump}} = 12 \text{ TW/cm}^2$ . At pump-probe overlap, a maximum occurs due to probe depletion because of reversible two-beam coupling. For longer delays, these effects can be neglected, such that the remaining absorption can be attributed to absorption in the undercritical plasma. The absorption then decays on the order of 150 fs, leading to a temporal asymmetry. From [BK3]

also be present in the delay-dependent emitted harmonics, if electron-impact ionization and subsequent avalanching were their generating mechanism. Thus, the temporal symmetry in the harmonics (Fig. 5.4) indicates, that electron-impact ionization can not be responsible for harmonic generation either.

As a plasma buildup was measured, a possible mechanism to generate harmonics is the electron-hole recombination (step 3 in Fig. 5.1), being the most dominant nonlinear process in high-harmonic generation in gasses, resulting in harmonics having photon energies of at least the bandgap energy. In the case of our observed harmonic signal however, we recognize that the strongest harmonic is detected at 450 nm (i.e. 2.75 eV), way below the bandgap of 7.7 eV. That is why also electron-hole recombination can be ruled out as a dominant wave-mixing process.

To study the role of the motion of electrons and holes in anharmonic conduction and valance bands for the emission of high harmonics (step 2 in 5.1), the experiment was also done with crystalline  $\text{SiO}_2$ . Those intraband harmonics can be found in amorphous and in crystalline solids, but in the latter, they are strongly orientation dependent. To this end, the crystalline target was rotated along the beam propagation axis of the pump beam. At a low pump intensity  $I_{\text{pump}} = 4 \text{ TW/cm}^2$  (i.e. far below plasma formation), the  $n = 1$  harmonic signal is produced by the Kerr-mechanism. Fig. 5.6 (a) shows that the emitted harmonic signal is highly orientation dependent which is attributed to the structural anisotropy of the crystal. Cranking up the pump intensity to  $I_{\text{pump}} = 12 \text{ TW/cm}^2$ , which is close to the damage threshold of the sample, the  $n = 1$  signal becomes isotropic (Fig. 5.6 (b)), such that we can conclude that neither for the crystalline nor for the amorphous  $\text{SiO}_2$  sample the harmonics are generated by intraband currents. Having ruled out Kerr-nonlinearities, coherent wake emission, electron-impact

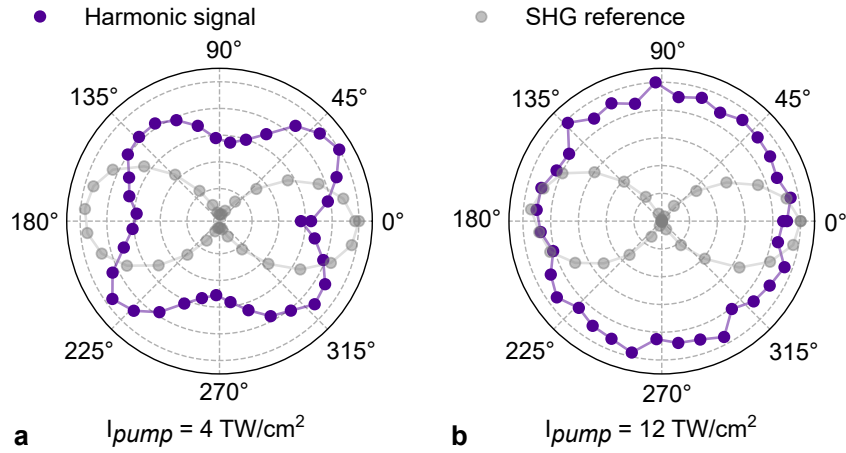


**Figure 5.6.:** The  $n = 1$  harmonic signal (purple dots and lines) for orthogonal pump-probe polarization in crystalline quartz ( $c\text{-SiO}_2$ ) as function of crystal orientation showing a four fold symmetry for (a)  $I_{\text{pump}} = 4 \text{ TW/cm}^2$  and an isotropy for (b)  $I_{\text{pump}} = 12 \text{ TW/cm}^2$ . The second harmonic generation signal of the probe (gray) is measured simultaneously and provides a reference for the crystal orientation. From [BK3]

ionization, interband currents and electron-hole recombination as relevant mechanisms for LOHG, the undercritical plasma buildup in the below-threshold regime via strong-field tunnel ionization seems to be the origin of the observed harmonics. To this end, we will next investigate the order of nonlinearity of the wave-mixing process, which will help us distinguish which mechanism in the plasma buildup is responsible for the harmonics.

### 5.3. Identification of the injection current as the dominant wave-mixing process

To identify which mechanism in the plasma buildup is responsible for the generated harmonics, we will introduce a method to classify the effective order of nonlinearity based on the parallel and perpendicular pump/probe polarization configurations.

#### 5.3.1. Effective order of nonlinearity

We start with the definition of the instantaneous nonlinear local polarization in terms of an effective  $m^{\text{th}}$  order nonlinear susceptibility  $\chi^{(m)}$

$$\mathbf{P}_{\text{NL}} = \varepsilon_0 \chi^{(m)} (\mathbf{E} \cdot \mathbf{E})^\mu \mathbf{E} \quad (5.3)$$

Remarkably, the order of nonlinearity  $m = 2\mu + 1$ , can be obtained from the two pump/probe polarization configurations without having to measure the pump intensity dependence of the harmonic signal. The latter method is especially cumbersome if the nonlinearity of the process changes with increasing pump intensity, making a scaling analysis less straight forward. To this end, we assume a strong electric pump field with the waveform  $\mathbf{E}_{\text{pump}}$  and a much weaker probe field  $\mathbf{E}_{\text{probe}}$  which together form the total incident field

$$\mathbf{E} = \mathbf{E}_{\text{pump}} + \mathbf{E}_{\text{probe}} = \frac{\hat{\mathbf{E}}_{\text{pump}}}{2} e^{i\omega_{\text{pump}}t} + \frac{\hat{\mathbf{E}}_{\text{probe}}}{2} e^{i\omega_{\text{probe}}t} + c.c. \quad (5.4)$$

where the exponentials describe the carrier waves and the amplitudes  $\hat{\mathbf{E}}_{\text{pump,probe}}$  also contain the polarization direction of the respective field. We insert this field into the nonlinear polarization (Eq. 5.3) and obtain a sum of many terms that describe the resulting mixing signals. Because the pump amplitude is much larger than the probe amplitude, we investigate only wave-mixing terms which are linear in the probe field. Also in the experiment, we could already see that no signal is observed with more than one probe frequency mixed in the final harmonic frequency. In the scenario where pump and probe are perpendicular polarized relative to another, all terms vanish where the probe field is contained in the scalar product. Consequently, only terms proportional to  $|\hat{\mathbf{E}}_{\text{pump}} \cdot \hat{\mathbf{E}}_{\text{pump}}|^\mu \hat{\mathbf{E}}_{\text{probe}}$  are non-zero, i.e. when the probe field appears in the last factor. In the case of parallel polarization however, the probe field can enter in any of the  $m$  positions, yielding an  $m$ -fold enhanced polarization amplitude. It follows that the intensity ratio of the mixing signal corresponds directly to the effective order of nonlinearity

$$m^2 = \frac{I_{\parallel}}{I_{\perp}}. \quad (5.5)$$

In the well-known case of a Kerr-nonlinearity ( $\chi^{(3)}$ ) this would translate to a ninefold amplification of the Kerr-type harmonics when pump and probe are polarized parallel as apposed to perpendicular.

The experiment was repeated in amorphous  $\text{SiO}_2$  for both polarization configurations and the pump intensity was scanned. The resulting effective order of nonlinearity is shown in Fig. 5.7 (violet data points). For low intensities, the nonlinear order is  $m = 3$  and matches the expected Kerr response. Near  $m = 5$  we see a plateau up to  $\approx 8 \text{ TW/cm}^2$  and then a steep lift-off to order  $m > 10$  near the damage threshold (indicated by the violet background). After this threshold is reached, we observe clear outliers at  $15 \text{ TW/cm}^2$ , which stem from permanent material damage (this was confirmed using an optical microscope). This lift-off from perturbative nonlinearity close to the damage threshold and the associated material damage are further hints at the plasma formation being responsible for the harmonic generation. As we ruled out all mechanisms for harmonic generation in section 5.2 besides ionization induced nonlinearity, we will employ a semi-classical ionization radiation model for the nonlinear source current and compare it to the experimental results.

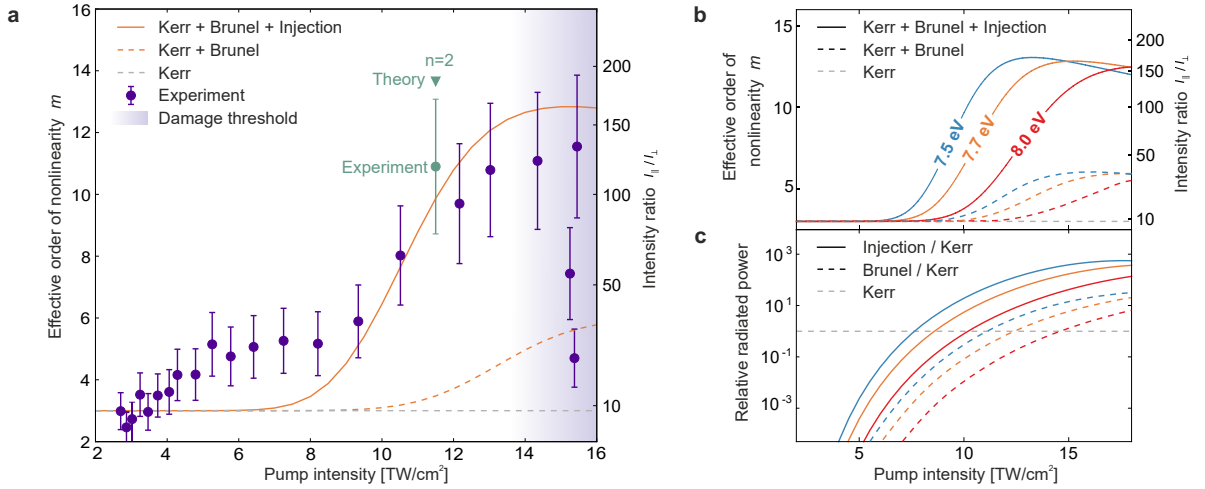


**Figure 5.7.:** (a) Effective order of nonlinearity  $m$  of the  $n = 1$  harmonic signal; both measured (purple dots) and numerically calculated (orange lines). Results from the ionization-radiation model were obtained incorporating separate harmonic mechanisms: Kerr only (gray dashed line), Kerr and Brunel (dashed orange line) and Kerr, Brunel and Injection (solid line). Additionally, for  $I_{\text{pump}} = 11 \text{ TW/cm}^2$ , the signal for  $n = 2$  has been calculated (green triangle) and measured (green dot). (b) Effect of bandgap energy on the numerically simulated effective nonlinear order  $m$ . (c) Relative radiated power contributing to the total signal from the injection current (solid lines) and the Brunel term (dashed colored lines), normalized to the Kerr-like nonlinearity (gray dashed line) at parallel pump-probe configuration. The colors in (b) and (c) are the same for the respective bandgap. From [BK3]

### 5.3.2. Ionization induced nonlinearity

In general, we can partition the polarization of a dielectric into a linear  $\mathbf{P}_L$  and a nonlinear part  $\mathbf{P}_{NL}$ , which we can further split into a fully reversible component that stems from the polarization of bound electrons following from virtual excitation (Kerr-type nonlinearity) and into a contribution from strong-field ionization (SFI)

$$\begin{aligned}\mathbf{P} &= \mathbf{P}_L + \mathbf{P}_{NL} \\ &= \mathbf{P}_L + \mathbf{P}_{\text{bound,Kerr}} + \mathbf{P}_{\text{SFI}}.\end{aligned}\tag{5.6}$$

The latter stems from the promotion of electrons into the conduction band. When we assume a parabolic conduction band, eliminating effects from band anharmonicities and Bloch oscillations due to reflections at zone boundaries, and neglect effective mass effects, we can formulate the current density stemming from electron population that was injected into the conduction band

$$\mathbf{J}_{\text{SFI}} = n_0 q_e [\langle \mathbf{v} \rangle \rho + \mathbf{x}_0 \dot{\rho}],\tag{5.7}$$

where  $\rho$  is density of conduction band electrons normalized to the molecular density  $n_0$ . The first term inside the square brackets describes current resulting from the average drift velocity  $\langle \mathbf{v} \rangle$  and the second term describes the so-called injection current, that is the current resulting from charge displacement when the electrons are injected. Note that this contribution is always important for energy conservation and not limited to a certain ionization regime. For long wavelengths, where the tunneling picture is applicable (like it is the case in this work) the displacement  $\mathbf{x}_0$  can actually be interpreted as the classical tunnel exit [106]. This displacement is the position, at which the electron exists the classical forbidden path through the potential barrier due to deformation of the atomic potential by the applied laser field. The length of the path reflecting the transport through the tunneling barrier depends on the ionization energy (or the band gap)  $E_g$  and the local electric field  $\mathbf{E}$

$$\mathbf{x}_0 = \frac{E_g}{q_e} \frac{\mathbf{E}}{|E|^2}.\tag{5.8}$$

This result is not specific to the tunneling regime and can be generally derived from the requirement of energy conservation in the radiation field and the injected electrons.

The radiation emerging from the injected electrons is proportional to to dipole acceleration, i.e. the first derivative of the strong field ionization current in Eq. 5.7

$$\frac{\partial}{\partial t} \mathbf{J}_{\text{SFI}} = n_0 q_e \left[ \frac{\partial}{\partial t} (\langle \mathbf{v} \rangle \rho) + \frac{\partial}{\partial t} (\mathbf{x}_0 \dot{\rho}) \right].\tag{5.9}$$

The derivative of the first term reads

$$\frac{\partial}{\partial t} (\langle \mathbf{v} \rangle \rho) = \langle \dot{\mathbf{v}} \rangle \rho + \mathbf{v}_0 \dot{\rho} \quad (5.10)$$

$$= \frac{q_e \mathbf{E}}{m_e} \rho + \mathbf{v}_0 \dot{\rho}. \quad (5.11)$$

The first term of this equation follows from an ensemble derivative (Ehrenfest theorem) and describes the acceleration of the already existing electron population. The second term accounts for the fact that the electrons do not emerge with the average velocity, but with an initial velocity  $\mathbf{v}_0$  different than the drift velocity. It depends on the ionization mechanism and is linked to the multiphoton excess energy. In the long wavelength limit (which is the case in our experiment), this term is negligible, so for further analysis we assume  $\mathbf{v}_0 = 0$ . The change of the conduction band electrons  $\dot{\rho} = \Gamma(|\mathbf{E}|)$  is dependent the subcycle injection rate. The last term in Eq. 5.9 describes the dipole acceleration resulting from the injection current discussed above. We arrive at the total dipole acceleration

$$\dot{\mathbf{J}}_{\text{SFI}} = q_e n_0 \left[ \frac{q_e \mathbf{E}}{m_e} \rho + \mathbf{v}_0 \dot{\rho} + \frac{\partial}{\partial t} (\mathbf{x}_0 \dot{\rho}) \right]. \quad (5.12)$$

The first two terms, i.e. the terms in Eq. 5.11 were already considered in the context of HHG in gases by Brunel [103]. He considered the long-wavelength limit as well, where the second term is negligible. In the first term however, the electron population  $\rho$  is highly dependent on the electric field strength, leading to steps in each half-cycle and therefore to an abrupt increase of the dipole acceleration, resulting in a nonlinear polarization and consequently in the emission of high harmonics (called *Brunel harmonics*). Surprisingly, despite its importance for energy conservation, the injection term describing the displacement due to the tunnel exit was not yet considered has a source of nonlinearity leading to harmonic emission.

To analyze the contribution of the injection and Brunel harmonics to the total harmonic signal, we solve the nonlinear dipole acceleration 5.12 numerically, using the Ammosov-Delone-Krainov (ADK) tunneling rate [87] for the actual electric laser field and a saturation term

$$\dot{\rho} = \Gamma(|\mathbf{E}|) = (1 - \rho) \Gamma_{\text{ADK}}(|\mathbf{E}|). \quad (5.13)$$

We also include the conventional Kerr-type polarization via Eq. 5.2 by taking the second derivative

$$\dot{\mathbf{J}}_{\text{Kerr}} = \chi^{(3)} \frac{\partial^2}{\partial t^2} (|\mathbf{E}|^2 \mathbf{E}), \quad (5.14)$$

with  $\chi^{(3)} = 1.9 \times 10^{-22} \text{ m}^2 \text{V}^{-2}$  (from [107, Ch. 7]). The molecular density of the  $\text{SiO}_2$  sample is  $n_0 = 2.2 \times 10^{22} \text{ cm}^{-3}$ . The total dipole acceleration density is integrated together with the conduction band density with a timestep of  $\Delta t = 5 \text{ fs}$ . As we do not

include any feedback from the resulting field to the material response, all three terms are independent of each other and the individual contributions can be analyzed separately. After Fourier transforming the resulting dipole acceleration, the harmonic peak of the spectral intensity is spectrally integrated for the desired harmonic order.

We calculated the effective order of nonlinearity by taking the resulting intensity ratios (just like in the experiment) and switched different contributions to the nonlinear current on or off and compare it to the experimental effective nonlinearity order in Fig. 5.7 (a). We find good agreement with the experimentally obtained effective nonlinearity order and also observe the rapid increase at  $\approx 8 \text{ TW/cm}^2$  when we include all three contributions (solid orange line). Note that the emergence of the ionization driven signal takes place way before the damage threshold. If we only consider the Brunel and Kerr contribution, the high effective nonlinearity is not even close to being achieved (dashed orange line). Additionally, the lift-off is shifted to higher pump intensities. For reference, also the pure Kerr-response is included and yields a nonlinearity order of three, which is of course expected for a  $\chi^{(3)}$  response.

The simulations verify in Fig. 5.7 (b) that the relative importance of the relevant terms does not depend on the exact bandgap; only the lift-off position changes. In Fig. 5.7 (c), we can see that this lift-off corresponds to the pump intensity at which the contribution from the injection current becomes as strong as the Kerr response. Also note that for the same bandgap, the injection contribution always dominates the Brunel contribution by at least one order of magnitude. Even for large variations of the bandgap energy, the Brunel term alone never dominates the injection current and can never explain the observed nonlinear order in our experiment (see Fig. 5.8). The robustness against bandgap variations shows that a-SiO<sub>2</sub> serves as a representative solid dielectric under the influence of strong fields. Due to the good agreement between theory and experiment together with the fact that the injection current always dominates the Brunel response we conclude that the injection dominated ionization-induced nonlinearities are the key source of the low-order harmonic wave-mixing signal for high intensities.

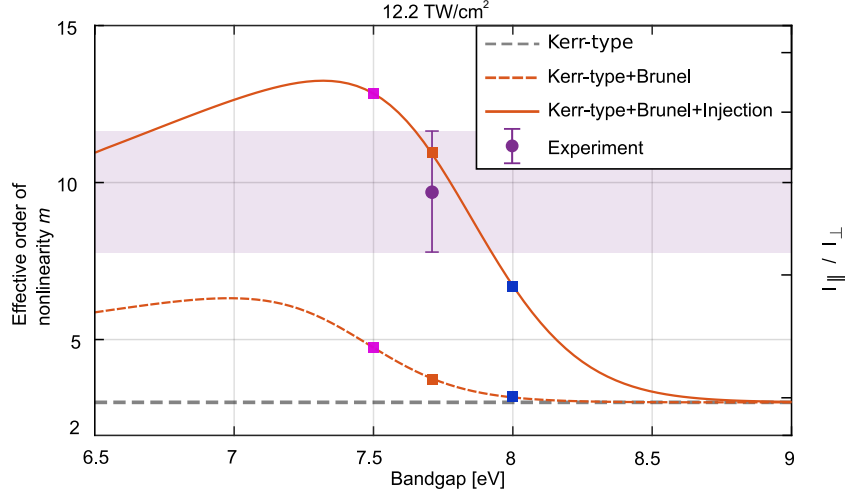


**Figure 5.8.:** Effective order of nonlinearity  $m$  as function of the bandgap for a pump intensity of  $I_{\text{pump}} = 12.2 \text{ TW/cm}^2$  when incorporating separate harmonic mechanisms: Kerr only (gray dashed line), Kerr and Brunel (dashed orange line) and Kerr, Brunel and Injection (solid line). The purple shaded area marks the experimentally measured effective nonlinearity at  $I_{\text{pump}} = 12 \text{ TW/cm}^2$  when taking the experimental uncertainties into account. The colored squares correspond to the bandgap values used in the pump intensity scan in Fig. 5.7 and mark the crossing point in the parameter space. From [BK3]

## 5.4. Conclusion

P. Jürgens et. al measured low-order harmonic generation and intraband and interband contributions could be ruled out experimentally. The analysis of the strong harmonic emission near the damage threshold by means of the effective nonlinearity via a numerical nonlinear local ionization radiation model showed that the tunneling injection current dominates low-order harmonic generation.

The technique to use a weak probe beam with a changeable polarization direction together with a strong pump beam is a very strong and robust tool to study the order of the dominant nonlinear process. It was especially helpful in our setup because we saw a strong dependence of the order with the pump intensity itself, which made a scan of the pump intensity and fitting the resulting harmonic yield not feasible and very inaccurate. From the experimental side, constant laser parameters and comparable plasma dynamics for each pump intensity, proved to be particularly robust. Our metrology is highly sensitive to the field dependent ionization rate and could thus be used for time-resolved characterization of ionization dynamics. Consequently the analysis of the plasma-formation below the damage threshold enables the analysis of strong-field induced material modifications and its comparison to electron impact ionization in the laser nano- and microprocessing of dielectrics.



# 6. Temporal Control of Cluster Ionization in Strong Fields

This project was done in collaboration with Bernd Schütte, who did the experiment, together with Arnaud Rouzée and Marc J. J. Vrakking from the Max-Born-Institut in Berlin. My theoretical calculations are the continuation of previous studies done by Mathias Arbeiter during his PhD time in the group of Prof. Thomas Fennel. To this end, I employed the thoroughly developed and reliable MD Cluster code by Mathias Arbeiter [108] to simulate the cluster dynamics. Because of the computational workload of MD simulations ( $O(N) = N^2$ ), the numerical calculations were performed on the HLRN-III (*Norddeutscher Verbund Für Hoch- und Höchstleistungsrechnen*) high-performance super computer.

## 6.1. Atomic clusters in strong fields

Ionization is the most fundamental process occurring during the interaction of ultrashort laser pulses with matter. At visible, ultraviolet and infrared wavelengths, the ionization of targets with a high ionization potential or a large bandgap requires a strong laser field. Numerous studies have been carried out investigating the strong-field ionization dynamics of atoms, molecules, nanoparticles and solids [109, 110, 111, 112]. In atoms, multiphoton and tunnel ionization have been identified as the two most important mechanisms. Compared to atoms, the ionization dynamics of solid-density dielectric targets are significantly more complex. Here the investigation of isolated clusters bears advantages over the study of bulk material: In comparison to a bulk dielectric, the energy exchange with the environment is strongly suppressed, providing a more direct access to the ionization dynamics of the system. Furthermore, while in a bulk dielectric an efficient energy exchange can occur between the laser-excited volume and the surrounding material, the small size of a cluster ensures that the entire particle interacts with the laser.

In single-pulse strong-field experiments on clusters, reaction products like ions [113, 114], neutral atoms [115], electrons [116, 117] and photons [118, 119, 120, 121] are measured to study the light-matter interaction. As the laser pulse lengths in those experiments are typically on the time scale of cluster expansion, the temporal dynamics of the underlying

processes leading to electron, ion and photon emission and absorption is not directly accessible. For instance, when a strong laser field interacts with a cluster, seed electron-hole pairs are initially generated by multiphoton and tunnel ionization. In a second step, heating and further ionization via various avalanching processes takes place, including electron impact avalanching and hole-assisted avalanching [122, 123, 124, 125, 126, 127, 128].

The response of a cluster to a strong laser field strongly depends on the efficiency of the first ionization step, i.e. multiphoton or tunnel ionization. As these ionization processes are highly nonlinear, the initial conditions followed by subsequent also nonlinear heating and avalanche processes make it difficult to observe the latter. It was shown recently that a both spatially and temporally well-controlled injection of seed electrons using an extreme-ultraviolet (XUV) pulse enables the control of avalanching and heating processes inside the cluster driven by a near-infrared (NIR) pulse [129]. In this study we use the ionization ignition concept to control the duration of the temporal window during which the NIR pulse can effectively further ionize the cluster. A moderately intense XUV pulse generates seed electron-hole pairs at well-defined times during an NIR pulse, whose intensity is insufficient to ionize the neutral cluster by itself. Ion charge state distributions from Xe and Ar clusters are recorded as a function of the time delay between the 20-fs long XUV pulse, obtained by means of high-harmonic-generation (HHG), and a 1.5-ps NIR pulse. Detailed information on the two-color ionization dynamics is obtained both experimentally and numerically. Extensive multiple atomic inner-shell ionization is observed under conditions, under which even single ionization of isolated atoms by the NIR pulse is negligible. We demonstrate that the main absorption process responsible for avalanching and heating is fluence-driven by showing that the induced dynamics by linearly and circularly polarized laser pulses are very similar.

## 6.2. Methods

### 6.2.1. Experimental setup

The experimental setup was previously described [130, 131, 129]. A Ti:sapphire laser system operating at a central wavelength of 800 nm was used to generate 35 fs pulses with an energy up to 30 mJ at a repetition rate of 1 kHz. About 85 % of the available energy was reflected by a beamsplitter and focused into a 15-cm-long gas cell that was statically filled with Kr to generate high harmonics [130] ranging from orders 11 to 21. This corresponds to photon energies between 17 and 32.5 eV, which are above the ionization potential of Kr (14 eV). A combination of an iris, a mirror with an antireflective coating at 800 nm, a Si mirror at Brewster's angle and a 100 nm thick Al filter were used to attenuate the NIR pulses co-propagating with the HHG pulses. The NIR beam that was transmitted by the beamsplitter was stretched to durations of 1.5 ps or 150 fs using glass blocks. The polarization of this beam could be changed from linear to circular by means of a  $\lambda/4$  waveplate. The XUV and NIR beams were recombined using a mirror with a 6 mm central hole, and were focused into the interaction zone of a velocity-map imaging spectrometer [132] operated in time-of-flight (TOF) mode using a 7.5 cm focal length  $B_4C$ -coated spherical mirror. Ar and Xe atoms and clusters were generated using a piezoelectric valve with a nozzle diameter of 1 mm operating at room temperature at a repetition rate of 10 Hz. The average cluster size of both Ar and Xe clusters was controlled by varying the backing pressure and estimated to be  $\langle N \rangle = 5000$  atoms according to the Hagenau scaling law [133]. A 0.2 mm diameter molecular beam skimmer was used to select the central part of the cluster beam.

### 6.2.2. Semiclassical molecular dynamics simulations

The semiclassical molecular dynamics simulations performed for this work are based on the MD-Cluster code by Mathias Arbeiter and are described in detail in his dissertation [108]. It is based on the classical quasi-electrostatic plasma dynamics and the classical interaction of the ions and plasma electrons with the laser. The classical equations of motion are

$$m_i \ddot{\mathbf{r}}_i = q_i \mathbf{E}_{\text{las}} - \nabla_{\mathbf{r}_i} \sum_{i \neq j} V_{ij}, \quad (6.1)$$

where  $m_i$  is the mass of the  $i^{\text{th}}$  particle,  $\mathbf{r}_i$  its spatial coordinates,  $q_i$  the charge and  $V_{ij}$  the interaction potential with another particle with index  $j$ . Each particle sees the same instantaneous electric laser field in dipole approximation  $E_{\text{las}}$  and all propagation effects of radiation are neglected. The EOM are propagated numerically using the velocity-Verlet algorithm [134]. To avoid an inaccurate description near the atomic core and unphysically deeply bound electron, the plasma particles are not described as point charges but are assumed to have Gaussian charge distribution (regularized Coulomb

interaction) with a width of  $s$ . This leads to the interaction potential between charged particles

$$V_{ij}(r_{ij}, q_i, q_j) = \frac{1}{4\pi\epsilon_0} \frac{q_i q_j}{r_{ij}} \operatorname{erf}\left(\frac{r_{ij}}{s}\right). \quad (6.2)$$

Neutral atoms interact via van-der-Waals interaction that is approximated using a Lennard-Jones Potential [135]. Importantly, icosahedral rare gas clusters show shell termination effects which lead to especially stable Clusters at so-called magic numbers ( $N=13, 55, 147, 309, 561, \dots$ ). In the simulations, those configurations are used to initialize the the starting position of the neutral atoms.

The non-classical part of the model is incorporated in the effective quantum mechanical treatment of inner ionization:

- **Tunnel ionization:** This ionization mechanism is included via the semi-classical ADK rate [87]. In this study, we are not in the field ionization regime, however.
- **Photo ionization:** The atomic cross sections, obtained from both experiments and theory [136, 137], are incorporated for dominant shells. Valance electrons, as well as inner shell electrons can be photo-ionized. For photoionization processes, essentially only the innermost subshell that is still accessible by the photon energy contributes. To account for higher charge states, the cross sections of the sub shells have been fit to quantum mechanically calculated cross sections according to [137]. Following inner shell ionization, Auger processes are also incorporated, where their ionization potentials were calculated quantum-mechanically [138].
- **Electron-impact ionization:** Free and quasi-free electrons can ionize other atoms via impact, if their kinetic energy is larger than the ionization potential. The electron-impact cross section, which is usually described by a parametric formula by Lotz [139, 140], is simplified using an analytical fit-model from [141] to account for plasma induced lowering of the ionization potential.

Moreover, electrons can recombine if their energy is below the local barrier between the the ions and its respective neighboring ion [142]. This relaxation process usually happens on the picosecond timescale, i.e. after the simulation is over, but is very relevant for the comparison with the experiment as recombination happens before the measurement of charge states. Hence, instead of propagating the MD simulation for several picoseconds, after the simulation, the recombination is calculated by evaluating the electron energy relative to its surroundings.

### 6.3. Temporal control of NIR cluster ionization

Fig. 6.1 (a) shows schematically how ionization of the cluster by the moderately strong NIR field is controlled using an XUV ignition pulse ( $I = 1 \times 10^{11}$  W/cm<sup>2</sup>, 20 fs) that generates a number of seed electron-hole pairs (up to 90 for Ar clusters and up to 60 for Xe clusters) by sequential ionization [143]. At negative time delays, where the peak of the NIR field precedes the peak of the XUV pulse, the NIR pulse ( $I = 1.5 \times 10^{13}$  W/cm<sup>2</sup>, 1.5 ps) can only effectively excite and ionize the cluster during a short time window in the falling edge of the NIR pulse. This time window increases towards positive time delays. An important advantage of the ionization ignition method is that focal volume averaging over different NIR intensities is largely avoided, since the XUV beam waist radius ( $d \approx 3$   $\mu\text{m}$ ) is much smaller than the NIR beam waist radius ( $d \approx 12$   $\mu\text{m}$ ). This facilitates comparisons of the experimental data to theory, compared to single-pulse strong-field ionization experiments [144].

Ion TOF spectra obtained from Xe clusters as a function of the XUV-NIR time delay are presented in Fig. 6.1 (b), and the corresponding ion yield distributions are displayed in Fig. 6.1 (c). This measurement provides detailed information on the two-color ionization as a function of the length of the interaction window: Ions in lower charge states are detected dominantly for delays where, following XUV ionization, the cluster interacts with only a small part of the NIR pulse. Higher charge states are only detected for delays where, after XUV ionization, the cluster interacts with a larger portion of the NIR pulse. Remarkably, extensive atomic inner-shell ionization with charge states reaching up to Xe<sup>15+</sup> is observed when the entire NIR pulse follows the XUV pulse, although both the XUV and NIR pulses by themselves lead to very small ionization. Noteworthy, the 15th ionization potential of Xe is 343 eV [145], which is more than two orders of magnitude larger than the ponderomotive potential of the NIR laser pulse ( $\approx 1$  eV). Such high ion charge states have previously been shown to be accompanied by strong X-ray emission [118, 146].

The average detected charge state resulting from two-color ionization of Xe and Ar clusters is compared in Fig. 6.1 (d). The average detected ionic charge exhibits a nonlinear increase for delays up to approximately  $-700$  fs, slows down near the temporal overlap of the XUV and NIR pulses, and saturates (i.e. delay-independent) for longer positive time delays. While the qualitative ionization dynamics are similar for both Xe and Ar clusters, the former become more highly ionized. The underlying reasons will be discussed below.

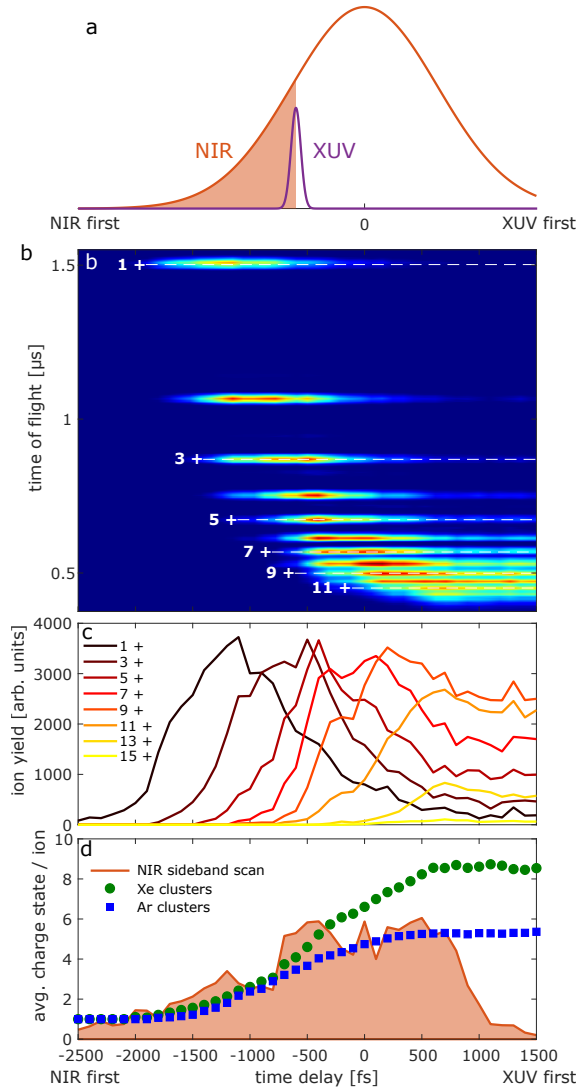


**Figure 6.1.:** Temporal control of NIR cluster ionization using an XUV pulse that generates seed electron-hole pairs at well-defined instances during the NIR pulse. (a) The XUV-NIR time delay defines the temporal length of the interaction window (orange shaded area), during which the NIR pulse can ionize the cluster. (b) Time-of-flight distributions reflecting the ionic charge state distributions obtained for Xe clusters ( $\langle N \rangle = 5000$  atoms) as a function of the delay between the XUV pulse ( $I = 1 \times 10^{11}$  W/cm<sup>2</sup>, 20 fs) and the NIR pulse ( $I = 1.5 \times 10^{13}$  W/cm<sup>2</sup>, 1.5 ps). (c) Delay-dependent yield of selected ion charge states. (d) Comparison of the average detected ion charge states for Xe (green circles) and Ar clusters (blue squares), with  $\langle N \rangle = 5000$  atoms each, allowing the identification of three delay ranges: (I) A near-exponential increase is observed at negative time delays up to about  $-700$  fs which (II) slows down around zero delay and (III) reaches saturation at positive time delays. The orange area shows the time-dependent NIR intensity, as obtained from an XUV-NIR cross-correlation scan where photoelectron sidebands were recorded in the ionization of atomic Ar. Measurement performed by Bernd Schütte.

To model the two-color ionization experiment, semiclassical molecular dynamics calculations [147] as described in subsection 6.2.2 were performed. For the Xe clusters we used a cluster size of  $N = 5083$  similar to the average experimental cluster size ( $\langle N \rangle = 5000$ ). As the numerical workload of molecular dynamics simulations scales with  $\sim N^2$ , a smaller cluster size was chosen for Ar ( $N = 561$ ). To make the chosen cluster sizes comparable, also smaller Xe clusters ( $N = 561$ ) were simulated.

The activation of previously atomically bound electrons, which overcome the potential of their parent atom, is referred to as inner ionization. Only a fraction of these electrons can escape the cluster potential (outer ionization) whereas most of the activated electrons remain bound to it. Weakly bound electrons are removed from the cluster potential by the static detector electric field during the cluster expansion [147]. To compare the simulated ionization to the outer ionization that was detected in the experiment, electron-ion recombination was accounted for in the calculations [142].

Fig. 6.2 (a) shows the inner charge state distribution of a  $\text{Xe}_{5083}$  cluster (which is not accessible experimentally). This exemplary single calculation was performed at a fixed XUV-NIR time delay of 2000 fs, meaning that after XUV ionization the cluster interacts with the entire NIR pulse. After the NIR pulse, the inner charge state does not change significantly anymore. Identifying re-localized electrons after sufficiently long time (here: 10 ps) leads to the estimation of the outer ionization (see gray arrow between Fig. 6.2 (a) and (b)). Fig. 6.2 (b) presents the calculated ion charge distributions after recombination as a function of the XUV-NIR time delay, showing the same features as in the experiment (cf. Fig. 6.1 (c)). We note that the appearance of individual charge states is observed over a shorter range of XUV-NIR time delays compared to the experimental result. This is attributed to the broad cluster size distribution ( $\langle N \rangle = 5000$  atoms) in the experiment. The delay-dependent charge distributions shown in Fig. 6.2 (b) show a qualitative resemblance to the obtained time-dependent charge distributions in Fig. 6.2 (a).

The discrepancies are due to the fact that electron-ion recombination and the emission of low-energy electrons take place on picosecond timescales [117] and are therefore not included in Fig. 6.2 (a). Furthermore, we like to stress, that the inner charge state over time and the outer charge state over pump-probe delay are two fundamentally different quantities. The evolution of the average ion charge state and the final average charge state of  $\text{Xe}_{5083}$  clusters presented in Fig. 6.2 (c) are similar to the experimental results presented in Fig. 6.1 (d). Fig. 6.2 (c) also reproduces the experimental finding that the ionization of Xe clusters is more efficient than the ionization of Ar clusters.

Analysis of the simulation results shows that the vast majority of ionization events (green dashed curve) occur via electron impact ionization. Only the initial electrons within the XUV pulse stem from photoionization. The electrons are heated via inverse Bremsstrahlung at the beginning of the NIR laser-cluster interaction, which becomes all the more efficient when the cluster expands, and when the laser frequency comes into resonance with the collective electronic dipole mode, the so-called Mie frequency [27].

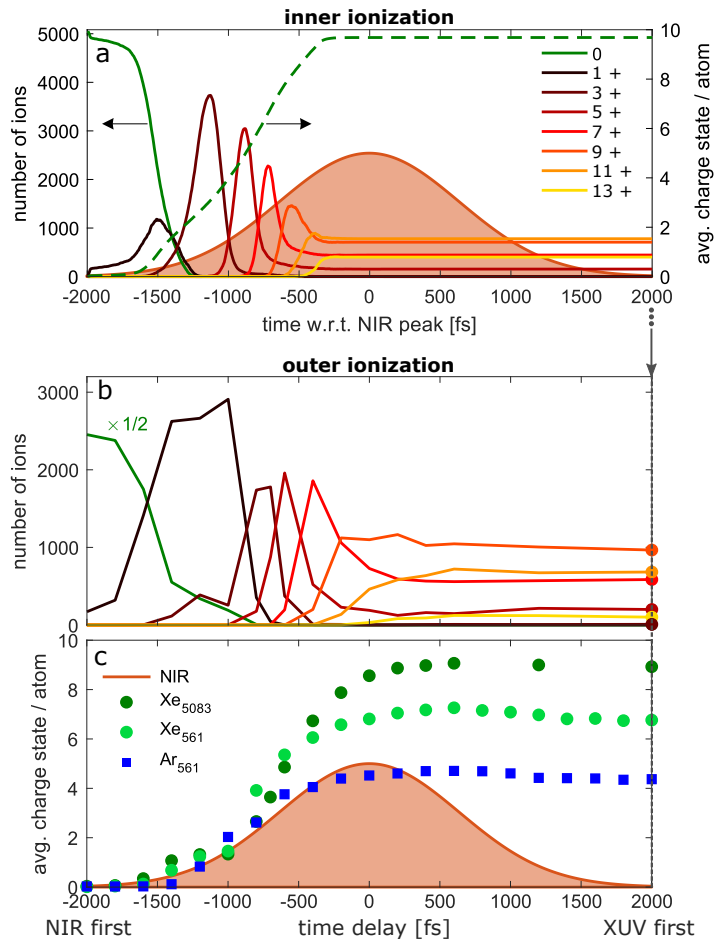


**Figure 6.2.:** (a) Numerically simulated inner ionization dynamics in a  $\text{Xe}_{5083}$  Cluster at a fixed XUV-NIR time delay of 2000 fs as function of the elapsed time with respect to the NIR peak. The evolution of the number of ions (red to yellow lines) and neutral atoms (green solid line) leads to an increase of the average inner charge state per ion (green dashed line). (b) Number of neutral atoms and ions in specific charge states after electron-ion recombination, corresponding to the outer ionization observed in the experiment following the exposure of  $\text{Xe}_{5083}$  clusters to the combination of an XUV pulse ( $I = 1.5 \times 10^{11} \text{ W/cm}^2$ , 20 fs) and an NIR pulse ( $I = 1.5 \times 10^{13} \text{ W/cm}^2$ , 1.5 ps), plotted as a function of the XUV-NIR time delay. The dots at 2000 fs mark the outer charge states resulting from the inner charge state evolution depicted in (a). (c) Outer ionization of  $\text{Ar}_{561}$ ,  $\text{Xe}_{561}$  and  $\text{Xe}_{5083}$  Clusters as function of delay between XUV ignition and NIR pulse (orange area).

## 6.4. Influence of atom mass, ionization potential and laser polarization on election impact avalanching

In order to study the effects of different atomic mass and IP independently, we performed simulations for clusters consisting of Ar or Xe atoms as well as for clusters consisting of artificial atoms that have the electronic structure of Ar and the mass of Xe or vice versa. Fig. 6.3 shows the evolution of the charge per atom resulting from inner ionization,  $q_{ii}$ , (solid curves) as well as the time-dependent Mie frequency (dashed curves) at a fixed XUV-NIR time delay of 2000 fs. The resonance condition  $\hbar\omega_{\text{Mie}} = \hbar\omega_{\text{NIR}} = 1.55$  eV (black line) is fulfilled twice because the Mie frequency is dependent on the ion charge density:  $\omega_{\text{Mie}} \propto \sqrt{\rho_{\text{ion}}}$ . The first resonance is driven by ionization as the charge density increases during ionization. In the resulting hot nanoplasma, electrons leak out of the cluster, leading to unscreened positive charges inside it and eventually to Coulomb expansion. The latter results in a decrease in charge density and consequently also the Mie frequency [129].

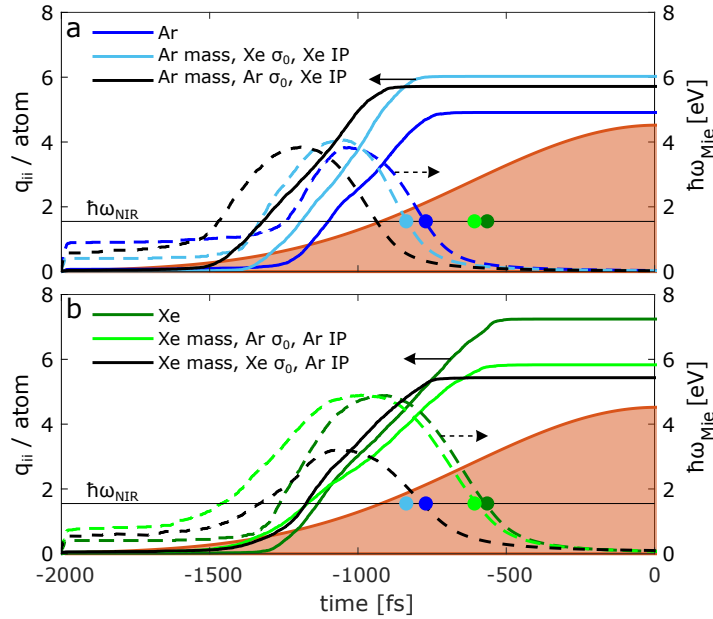


**Figure 6.3.:** Simulated time dependence of inner ionization per atom for (a) Ar clusters (blue) and for (b) Xe clusters (green). The light blue (a) and light green (b) curves represent clusters consisting of atoms having Ar mass with Xe ionization potential and vice versa. Each cluster consists of 561 atoms. The XUV-NIR time delay was 2000 fs, meaning that after ionization by the XUV pulse the cluster interacted with the entire NIR pulse. The dotted curves represent the corresponding evolutions of the energy of the Mie plasmon. The orange area is the NIR intensity ( $I = 1.5 \times 10^{13}$  W/cm<sup>2</sup>) envelope and the black line is the NIR photon energy. The colored dots represent the moment of the expansion-induced resonance for the corresponding clusters.

In Fig. 6.3 we observe that inner ionization predominantly takes place within the time window between the first (ionization-induced) and the second (expansion-induced) resonance. This time window is significantly longer for the heavier Xe cluster (dark green curves in (b)) compared to the cluster with Ar mass and Xe IPs (light blue curves in (a)), due to the slower expansion, explaining the higher degree of ionization in the former case. Moreover, the ionization degree depends on the efficiency of ionization. While a cluster with Xe mass and Ar IPs (light green curves in (b)) is ionized during an even longer time window than an actual Xe cluster, ionization of Xe atoms is more efficient (due to the lower IPs), resulting in a higher ionization. We conclude that atoms with a large mass and low IPs provide the most favorable conditions for a high ionization degree of clusters in the ionization ignition scheme using pulses of picosecond pulse length.

We employ the above scheme to study seeded electron impact avalanching for linear and circular polarization. In a single-pulse experiment, ionization of clusters by circularly polarized NIR pulses ( $I = 9 \times 10^{13} \text{ W/cm}^2$ ) results in a much lower ion yield compared to linearly polarized NIR pulses, see Fig. 6.4 (a). This discrepancy is attributed to the high nonlinearity of tunnel multiphoton ionization during the ignition step which is a field-driven process here. For the same intensity, the peak field strength of the circular polarized NIR pulse is a factor of  $1/\sqrt{2}$  lower than in the linear polarized case, leading to fewer seed electrons. In order to investigate the role of polarization during the heating process, we can take advantage of the ionization ignition method. The nonlinear nature of tunnel ionization is effectively switched off by injecting seed electron with an XUV pulse ( $I = 1 \times 10^{11} \text{ W/cm}^2$ , 20 fs) 100 fs before a weaker NIR pulse ( $I = 4 \times 10^{13} \text{ W/cm}^2$ ), making the measurement sensitive only to the heating process. For both polarization configurations, the observed TOF spectra are very similar (Fig. 6.4 (b)). Both experiment and simulation show ratios of the ion yields obtained with circular and linear polarization that are close to 1 (see the inset of Fig. 6.4 (b)). This shows that electron impact avalanching is independent of the NIR polarization and consequently a fluence-driven process, i.e. a process driven by the temperature of the hot electron gas in contrast to impact events induced by the periodical quiver motion of the electron cloud.

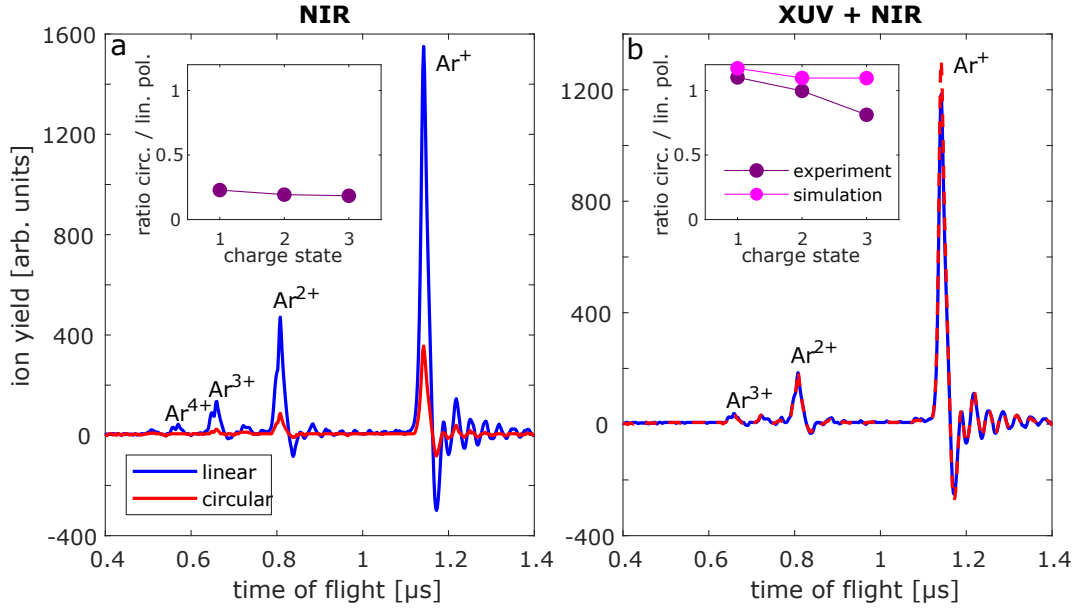


**Figure 6.4.:** Ionization of Ar clusters ( $\langle N \rangle = 5000$  atoms) by linearly and circularly polarized NIR pulses. (a) Comparison of ion TOF spectra obtained after ionization of Ar clusters using an NIR pulse only ( $I = 9 \times 10^{13}$  W/cm<sup>2</sup>) with linear polarization (blue curve) or circular polarization (red curve). The inset shows the experimentally obtained ratio of ion yields obtained with circular and linear NIR polarization. (b) Ion TOF spectra following ignition by an XUV pulse ( $I = 1 \times 10^{11}$  W/cm<sup>2</sup>, 20 fs) and heating by an NIR pulse ( $I = 4 \times 10^{13}$  W/cm<sup>2</sup>, pulse duration 150 fs, delayed by 100 fs) that is either linearly polarized (blue curve) or circularly polarized (red curve). The inset shows the ratios of the ion yields induced by circular and linear polarization in the experiment (violet curve) and in the simulation (pink curve). The simulated cluster size is  $N = 1415$ . Measurement performed by Bernd Schütte.

## 6.5. Conclusion

In summary, we have demonstrated temporal control over the ionization of dielectric clusters in strong laser fields by applying a moderately intense XUV pulse that ignites the ionization at well-defined times during the NIR pulse. This opens up the way to temporally and spatially control ionization and thus material ablation in dielectric liquids and bulk solids, greatly improving the precision in nanomachining and nanosurgery applications [93]. Our experimental and numerical results show qualitative agreement and found electron impact avalanching and resonant ionization to be the underlying mechanisms for the used pulse parameters, suggesting that large atomic mass and low IPs lead to high ionization degrees. The time resolution of our method is given by the XUV pulse duration and can be improved by applying intense few-femtosecond or attosecond pulses for ignition.

# 7. Conclusions and Outlook

## Summary

The main goal of this work was the investigation of the influence of bound-state quantum dynamics to coherent diffractive imaging. To this end, a semi-classical few-level density matrix model was derived and implemented into the framework of FDTD to solve Maxwell's equations, which are already widely used to simulate similar problems, for example the scattering of metal nanoparticles, where the metal was modeled using the Drude-Lorentz model [25]. A benefit of the implementation of the FLDM-model was the matching to the Drude-Lorentz parameters that provided an invaluable benchmark tool. As the propagation into the far field is not feasible on a numerical grid, a near field to far field transformation was implemented using free-space propagators. In a first prove-of-principle investigation, where only the ground state and the first 2p states were considered and matched to the DLM parameters, tremendous changes in the scattering images of resonantly excited helium nanodroplets were observed when the intensity was high enough to induce population dynamics. This led to saturation of the scattering images, change of fringe spacing, as well as a blurring of the ring structure, suggesting that nonlinear population dynamics leave a distinct spectral fingerprint in the scattering images.

A next step in this study was the investigation of the influence of multiple transitions. Due to the coupling between the few-level systems with the electromagnetic field, a numerical instability was identified and analyzed, when in a dense medium the levels are too close together and population inversion takes place. Unfortunately, this is a common configuration in multilevel schemes, for example when Rabi-cycling between the ground state and a higher p-state is happening and an s-state is energetically just below the higher p-state (e.g. in Helium). To this end, two physically relevant workaround scenarios were developed.

The first scenario is an extension of the single transition QCDI scenario, because also 3p and 4p levels were considered, circumventing the instability by turning off transitions between states that are close together. The incorporation of the  $1s^2$ - $1s3p$  transition led to an absorption at that transition frequency, creating a spectral imbalance in the scattered light spectrum. Additionally, the relative importance of the  $1s$ - $2p$  transition is lower when more levels contribute to the total dipole moment of the system.

In the second scenario, the transient modification of the optical parameters by an NIR

pulse and their effect on the scattering from a weak XUV pulse (located at 20.9 eV, just below the 1s-2p resonance) was investigated. Due to the weak XUV pulse, no population transfer is happening, which makes the numerical simulation stable. With increasing NIR intensity, the scattered fraction decreased because of the changing optical parameters due to a shift of the spectral line position. By employing a 0D FLDM calculation to obtain the effective refractive index  $n$  for a given NIR intensity, the role of the real and imaginary part of  $n$  could be investigated separately by calculating scattering images using Mie theory. This led to the conclusion that the imaginary part modifying the absorption was mainly responsible for the decrease in scattered intensity.

The next part of this work presented the research done on the origin of strong-field induced low-order harmonics in  $\text{SiO}_2$ . We proposed the methodology of the effective nonlinear order to identify the injection current, i.e. the current which is associated with the promotion of electrons from the valence to the conduction band, as the dominant mechanism for the generation of low-order harmonics. The measured effective nonlinearity was simulated using a robust semi-classical ionization radiation model. Moreover, the different contributions to the nonlinear source current could be turned on or off, confirming that the injection harmonics always dominate the Brunel contribution and during undercritical plasma buildup also the Kerr harmonics in the investigated wavelength regime.

The last part was dedicated to the study of the light-matter interaction of rare-gas (Xe, Ar) clusters with a strong picosecond NIR pulse and a short femtosecond XUV ignition pulse. By varying the delay between the two pulses, the onset of electron impact ionization avalanching and consequently plasma dynamics could be controlled, leading to higher ion charge states the earlier ignition starts during the NIR heating pulse. The MD simulation showed that the final observed charge states of the ions are not the same as the inner charge states during the ionization of the pulse. Even though the delay dependent charge states are not a direct movie of the cluster ionization, their temporal evolution are qualitatively similar. Additionally, the MD simulations revealed that the charge states for Xenon clusters were higher than for Argon due to lower ionization potential in Xe clusters and due to their larger mass, leading to a slower cluster expansion and therefore to a longer time the cluster can ionize before the second Mie resonance is met. By comparing the ion yield for linearly vs. circularly polarized NIR pulses, we observed a strong decrease, as tunnel ionization from the NIR pulse is a field driven process and circular pulses have a  $1/\sqrt{2}$  lower field strength, leading to fewer seed electrons. However, using an XUV ignition pulse before the NIR pulses resulted in very similar charge states for both linearly and circularly polarized NIR pulses, showing that the electron impact ionization avalanching is a fluence-driven process.

### Critical discussion and outlook

In addition to considerations for the light-matter interaction, more advanced propagation method can be used in FDTD. In this work, the incident electric field could only be a linear polarized plane wave. For applications where the laser focus is not much larger than the target (e.g. large nanoparticles, surfaces or bulk) a thorough description of the laser focus and its modes could be needed. The propagation waves presented in chapter 3 could be influenced by the finite size of the focus. Additionally, possible intensity variations based on the droplet's position within the focus can influence the nonlinearity when interacting with the XUV pulse. However, the light sources used in similar experiments on Helium nanodroplets (FERMI FEL[26], HHG source [32]), focused the XUV down to  $\approx 10\mu\text{m}$  spot size, which makes the laser spot size only relevant for larger targets than the ones presented in this work.

Concerning the FFLM-FDTD model itself, even though the numerical instability was identified and quantified, the workarounds (which provided interesting results nevertheless) are not that satisfactory from a physical point of view. Instead of working around the instability, a next goal should be what physically happens when the instability occurs, and why it is not observed in reality or put another way, what happens in a dense medium when two states that are energetically close together are populated? Further investigations of this topic could involve a full quantum mechanical description of two closely located atomic potentials to recreate the instability from the FLDM-FDTD model. One speculation is that the interaction of the two potentials would self-consistently correct the transition dipole matrix elements, resonance frequencies, and decoherence times.

Incorporating ionization into the model is another next logical step. By taking continuum states into account, population that is transferred there, could then be propagated by a particle model like molecular dynamics [148] or microscopic particle-in-cell (MIC-PIC [149]). In the latter method, the electromagnetic fields are also propagated using FDTD, and the local electromagnetic response is treated by a Drude-Lorentz model. The ionization probability is calculated by temporally integrating the imaginary part of the resulting dipole response. The analogue probability could be obtained by the population in the continuum states of a few-levels system, so the merging of both the the FLDM and MIC-PIC at least seems feasible and logical.

In short, the thorough combination of the propagation of both fields and particles together with their bound state population dynamics can open up exciting new routes for experiments on strong light-matter interaction and especially for coherent diffractive imaging.



# Appendix

## A. Definition: Fourier transformation

There are multiple ways to describe Fourier transformation. Mostly it does not matter, which formulation is used as long as transforming to Fourier space and back to real space again lead to the initial function again. It is only important when solving differential equations and derivatives. In optics, the Fourier transformation also physically represents a decomposition into plane waves ( $e^{ikx-i\omega t}$ ) meaning that the signs of spatial and temporal Fourier Transformation need to have opposite sign.

In this work I use the forms:

**Forward** (going to Fourier domain):

$$f(\omega) = \frac{1}{2\pi} \int f(t)e^{i\omega t} dt \quad (\text{A.1})$$

$$f(k) = \frac{1}{2\pi} \int f(x)e^{-ikx} dx \quad (\text{A.2})$$

**Backward** (coming from Fourier domain):

$$f(t) = \int f(\omega)e^{-i\omega t} d\omega \quad (\text{A.3})$$

$$f(x) = \int f(k)e^{ikx} dk \quad (\text{A.4})$$

such that derivatives in the time domain become algebraic in the frequency domain and vice versa

$$\partial_t \leftrightarrow -i\omega \quad (\text{A.5})$$

$$\partial_x \leftrightarrow +ik \quad (\text{A.6})$$

## B. Derivation of the EOM for the expectation value of the dipole moment of a two-level system

We want to derive the equation of motion for the  $x$ -component of the expectation value of the dipole moment. Departing from the assumptions made in subsection 2.2.3 about the two-level system we write out the matrices of the operators

$$\text{dipole operator:} \quad \hat{d}_x^S = \begin{pmatrix} 0 & \mu \\ \mu & 0 \end{pmatrix} \quad (\text{B.1})$$

$$\text{relaxation rate:} \quad \gamma = \begin{pmatrix} 0 & \gamma_d \\ \gamma_d & 0 \end{pmatrix}. \quad (\text{B.2})$$

The expectation value of the dipole moment is calculated using the trace of the product with the density matrix

$$\langle \hat{d}_x \rangle = \text{Tr}(\hat{d}_x \hat{\rho}) = \mu (\rho_{10}^S + \rho_{01}^S) \quad (\text{B.3})$$

and after transforming the density matrix to the interaction picture via Eq. 2.37 and recalling that  $\omega_{10} = -\omega_{01}$ :

$$\langle \hat{d}_x \rangle = \mu (\rho_{10}^I e^{-i\omega_{10}t} + \rho_{01}^I e^{i\omega_{10}t}) := \mu(A + B). \quad (\text{B.4})$$

The formal derivative reads

$$\langle \dot{\hat{d}}_x \rangle = \mu [\dot{\rho}_{10}^I e^{-i\omega_{10}t} - i\omega_{10}\rho_{10}^I e^{-i\omega_{10}t} + \dot{\rho}_{01}^I e^{i\omega_{10}t} + i\omega_{10}\rho_{01}^I e^{i\omega_{10}t}]. \quad (\text{B.5})$$

Inserting the evolution of the density matrix from the generalized von Neumann equation 2.66 into the dipole velocity we find

$$\begin{aligned} \langle \dot{\hat{d}}_x \rangle = & \mu \left( -\frac{i}{\hbar} [H_{\text{int},10}^I \rho_{00}^I - \rho_{11}^I H_{\text{int},10}^I] - \gamma_d \rho_{10}^I - i\omega_{10} \rho_{10}^I \right) e^{-i\omega_{10}t} \\ & + \mu \left( -\frac{i}{\hbar} [H_{\text{int},01}^I \rho_{11}^I - \rho_{00}^I H_{\text{int},01}^I] - \gamma_d \rho_{01}^I + i\omega_{10} \rho_{01}^I \right) e^{i\omega_{10}t} := \mu(\dot{A} + \dot{B}). \end{aligned} \quad (\text{B.6})$$

Transforming the interaction Hamiltonian to the Schrödinger picture  $H_{\text{int},01}^I = H_{\text{int},01}^S e^{-i\omega_{10}t}$  and  $H_{\text{int},10}^I = H_{\text{int},10}^S e^{i\omega_{10}t}$  and recalling that  $\hat{H} = \hat{H}^\dagger$  we find that the terms containing the interaction Hamiltonian vanish, resulting in

$$\langle \dot{\hat{d}}_x \rangle = i\omega_{10}\mu \underbrace{(-\rho_{10}^I e^{-i\omega_{10}t} + \rho_{01}^I e^{i\omega_{10}t})}_{B-A} - \underbrace{\mu\gamma_d (\rho_{10}^I e^{-i\omega_{10}t} + \rho_{01}^I e^{i\omega_{10}t})}_{\gamma_d \langle \hat{d}_x \rangle}. \quad (\text{B.7})$$

Taking the second derivative yields the dipole acceleration

$$\langle \ddot{\hat{d}}_x \rangle = i\omega_{10} (\dot{B} - \dot{A}) - \gamma_d \langle \dot{\hat{d}}_x \rangle. \quad (\text{B.8})$$

Directly inserting the previous results from Eq. B.6 yields

$$\begin{aligned} \langle \ddot{\hat{d}}_x \rangle &= i\omega_{10}\mu \left\{ \left[ \left( -\gamma_d \rho_{01}^I + i\omega_{10} \rho_{01}^I \right) e^{i\omega_{10}t} - \frac{i}{\hbar} \left( H_{\text{int},01}^S \rho_{11}^S - H_{\text{int},01}^S \rho_{00}^S \right) \right] \right. \\ &\quad \left. + \left[ \left( \gamma_d \rho_{10}^I + i\omega_{10} \rho_{10}^I \right) e^{-i\omega_{10}t} + \frac{i}{\hbar} \left( H_{\text{int},10}^S \rho_{00}^I - \rho_{11}^I H_{\text{int},10}^S \right) \right] \right\} - \gamma_d \langle \dot{\hat{d}}_x \rangle \end{aligned} \quad (\text{B.9})$$

$$\begin{aligned} &= i\omega_{10}\mu \left[ -\frac{2i}{\hbar} H_{\text{int},01}^S \left( \rho_{11}^I - \rho_{00}^I \right) \right] - \underbrace{\gamma_d i\omega_{10} \left[ \rho_{01}^I e^{i\omega_{10}t} - \rho_{10}^I e^{-i\omega_{10}t} \right]}_{\gamma_d \langle \dot{\hat{d}}_x \rangle + \gamma_d^2 \langle \hat{d}_x \rangle} \\ &\quad - \omega_{10}^2 \underbrace{\left( \rho_{01}^I e^{i\omega_{10}t} + \rho_{10}^I e^{-i\omega_{10}t} \right)}_{\langle \hat{d}_x \rangle} - \gamma_d \langle \dot{\hat{d}}_x \rangle, \end{aligned} \quad (\text{B.10})$$

where we identified the dipole moment and the dipole velocity, finally resulting in the equation of motion for the ideal two level system

$$\boxed{\langle \ddot{\hat{d}}_x \rangle = i\omega_{10}\mu \left[ -\frac{2i}{\hbar} H_{\text{int},01}^S \left( \rho_{11}^I - \rho_{00}^I \right) \right] - 2\gamma_d \langle \dot{\hat{d}}_x \rangle - \left[ \gamma_d^2 + \omega_{10}^2 \right] \langle \hat{d}_x \rangle.} \quad (\text{B.11})$$

## C. Detailed derivation of the near field to far field transformation

The goal of the following derivation is to describe the outgoing field generated by a given scatterer by a different set of sources that is easier to handle regarding the description of the far field. In particular, a given field passing a control surface. The goal is that (i) this 'equivalent' source creates the same external field and (ii) allows an easy evaluation of the far field by using only free-space propagators.

The derivation is based on [75] and [63] presented using our notation. We will depart from the formulation of field continuity relations for currents and magnetization on a surface. Afterwards the basic concept of the equivalent source theorem will be discussed. With the equivalent sources it is finally possible to define associated vector potentials. The latter can be used to evaluate the electromagnetic fields in the far field using free-space propagators based on a field sampled only on a closed control surface in the computational box.

### C.1. Field continuity relations for currents and magnetization on a surface

We depart from Maxwell's microscopic equations

$$\nabla \cdot \mathbf{E} = \frac{\rho}{\varepsilon_0} \quad (\text{C.1})$$

$$\nabla \cdot \mathbf{B} = 0 \quad (\text{C.2})$$

$$\nabla \times \mathbf{E} = -\dot{\mathbf{B}} \quad (\text{C.3})$$

$$\nabla \times \mathbf{B} = \mu_0 (\mathbf{j} + \varepsilon_0 \dot{\mathbf{E}}). \quad (\text{C.4})$$

And the continuity relation for current and charge density

$$\nabla \cdot \mathbf{j} + \dot{\rho} = 0. \quad (\text{C.5})$$

We split the current density into a charge-based current  $\mathbf{j}_C$  and a magnetization-based contribution  $\mathbf{j}_M$ , which mimic local atomic ring currents (there are no magnetic charges). Ring currents have to be divergence free, so we define

$$\mathbf{j}_M = \nabla \times \mathbf{M}, \quad (\text{C.6})$$

where the magnetization  $\mathbf{M}$  is also set divergence free (curl operation will erase them anyway). Because the magnetization current is now divergence free, charges can only be changed by the charge-based current via its sources. Also note that the charge-based current  $\mathbf{j}_C$  can still contain curl contributions which are associated with flowing charges but not with material magnetization as this part is shifted into  $\mathbf{j}_M$ .

The fourth Maxwell equation now reads

$$\nabla \times \mathbf{B} = \mu_0 \mathbf{j}_C + \mu_0 \dot{\mathbf{j}}_M + \varepsilon_0 \mu_0 \dot{\mathbf{E}} \quad (\text{C.7})$$

$$\nabla \times [\mathbf{B} - \mu_0 \mathbf{M}] = \mu_0 \mathbf{j}_C + \varepsilon_0 \mu_0 \dot{\mathbf{E}}, \quad (\text{C.8})$$

where we inserted the definition of  $\dot{\mathbf{j}}_M$ . The part in the brackets is the definition of the magnetizing field  $\mathbf{H} = \frac{1}{\mu_0} \mathbf{B} - \mathbf{M}$  and leads to Maxwell's modified curl equations, where we separated the charge based current and the Magnetization

$$\nabla \times \mathbf{H} = \mathbf{j}_C + \varepsilon_0 \dot{\mathbf{E}} \quad (\text{C.9})$$

$$\nabla \times \mathbf{E} = -\mu_0 \dot{\mathbf{H}} - \mu_0 \dot{\mathbf{M}}. \quad (\text{C.10})$$

The left side of the first equation (i.e. Eq. C.9) is free of sources, which implies for the right side that any sources of  $\mathbf{j}_C$  can only modify the displacement current (i.e. the electric field). Hence, sources of  $\dot{\mathbf{E}}$  can only stem from the divergence  $\nabla \cdot \mathbf{j}_C$  - in accordance with the continuity equation and the first Maxwell equation. Any source-free terms in  $\mathbf{j}_C$  at a surface will lead to jumps in the magnetizing field. This also applies to  $\dot{\mathbf{M}}$  and the electric field respectively. We will exploit this fact later to create desired field jumps at a surface. Without any charge-based currents  $\mathbf{j}_C$  or magnetization rate  $\dot{\mathbf{M}}$  the two curl equations will only lead to propagating wave-like solutions or to optical non-propagating evanescent solutions. As long as we do not switch on a divergence-free surface current (to avoid accumulation of charges), we can integrate Eq. C.9 to see the effect on the magnetic field, which will be shown in the following.

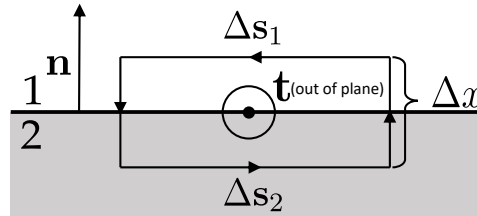


**Figure C.1.:** On a surface between materials 1 and 2, an integration over an area indicated by the normal vector  $\mathbf{t}$  is performed. The integration loop (when applying Stoke's theorem) is made infinitesimal small when  $\Delta x \rightarrow 0$ . Figure adapted from [150]

We consider a scenario as sketched in Fig. C.1, where we have a surface with a normal vector  $\mathbf{n}$  between two materials 1 and 2, and integrate a surface current density

$$\mathbf{j}_C = \delta((\mathbf{r} - \mathbf{r}_S) \cdot \mathbf{n}) \mathbf{J}_S, \quad (\text{C.11})$$

that is located at the surface position  $\mathbf{r}_S$  and perpendicular to the normal vector  $\mathbf{n}$  of the surface, where the unit of  $\mathbf{J}_S$  is current per unit length. The integration area  $d\mathbf{A} = dA \mathbf{t}$  is pointing out of the paper plane. Integrating Eq. C.9 over this area and applying Stokes' theorem yields an integration over the loop around the area

$$\iint_A d\mathbf{A} \cdot (\nabla \times \mathbf{H}) = \oint_{\partial A} d\mathbf{r} \cdot \mathbf{H}. \quad (\text{C.12})$$

When taking the limit ( $\Delta x \rightarrow 0$ ) the loop becomes negligibly small in the direction perpendicular to the surface and the contour integration becomes

$$\lim_{\Delta x \rightarrow 0} \oint_{\partial A} d\mathbf{r} \cdot \mathbf{H} = \mathbf{H}_1 \cdot \Delta \mathbf{s}_1 + \mathbf{H}_2 \cdot \Delta \mathbf{s}_2, \quad (\text{C.13})$$

where  $\mathbf{H}_1$  and  $\mathbf{H}_2$  are the magnetizing fields in material 1 and 2 respectively. Looking at the sketch again, we see that

$$\Delta \mathbf{s}_1 = (\mathbf{t} \times \mathbf{n}) \Delta s = -\Delta \mathbf{s}_2 \quad (\text{C.14})$$

and thus finally for the integrated left side of Eq. C.9

$$\mathbf{H}_1 \cdot \Delta \mathbf{s}_1 + \mathbf{H}_2 \cdot \Delta \mathbf{s}_2 = \Delta s (\mathbf{t} \times \mathbf{n}) \cdot (\mathbf{H}_1 - \mathbf{H}_2). \quad (\text{C.15})$$

When integrating the right side of Eq. C.9 the second term vanishes when taking the limit  $\Delta x \rightarrow 0$  because all non-singular (i.e. finite) contributions will vanish in this limit. The curl component of the electric field cannot be singular as this would lead to an even more singular magnetic field (see Maxwell's 3rd equation) and so on

$$\iint_A d\mathbf{A} \cdot \mathbf{j}_C + \varepsilon_0 \underbrace{\iint_A d\mathbf{A} \cdot \dot{\mathbf{E}}}_{=0 \text{ for } \Delta x \rightarrow 0} \quad (\text{C.16})$$

$$= \iint_A dA \mathbf{t} \cdot \mathbf{j}_C \quad (\text{C.17})$$

$$= \iint_A dA \mathbf{t} \cdot \mathbf{J}_S \delta((\mathbf{r} - \mathbf{r}_S) \cdot \mathbf{n}) \quad (\text{C.18})$$

$$= \mathbf{t} \cdot \mathbf{J}_S \Delta s. \quad (\text{C.19})$$

Because of the delta-function we only get contributions of the surface current directly at the surface.

Combining eqs. C.15 and C.19

$$\Delta s (\mathbf{t} \times \mathbf{n}) \cdot (\mathbf{H}_1 - \mathbf{H}_2) = \mathbf{t} \cdot \mathbf{J}_S \Delta s \quad (\text{C.20})$$

and exploiting the cyclic interchangeability of the triple product yields

$$\mathbf{t} \cdot (\mathbf{n} \times (\mathbf{H}_1 - \mathbf{H}_2)) = \mathbf{J}_S \cdot \mathbf{t}. \quad (\text{C.21})$$

As the integration loop and thus its normal vector  $\mathbf{t}$  is positioned arbitrary inside the surface perpendicular to the surface normal vector  $\mathbf{n}$ , there are two linearly independent directions for  $\mathbf{t}$ . The dot products on both sides of Eq. C.21 must be fulfilled for both directions, resulting in

$$\mathbf{n} \times (\mathbf{H}_1 - \mathbf{H}_2) = \mathbf{J}_S. \quad (\text{C.22})$$

When we assume that there is no medium this reads

$$\boxed{\mathbf{n} \times (\mathbf{B}_1 - \mathbf{B}_2) = \mu_0 \mathbf{J}_S} \quad (\text{C.23})$$

This means that a jump of the tangential magnetic field can be created by the surface current that is only flowing inside the surface and thus has no component along the surface normal.

The same considerations can be done for a finite magnetization rate  $\dot{\mathbf{M}}$  and integrate Eq. C.10 over a thin loop for which contributions from  $\dot{\mathbf{H}}$  vanish as well as contributions for  $\dot{\mathbf{E}}$  did. We consider a surface magnetization of the form which is fully tangential to the surface as in the case of the surface current

$$\dot{\mathbf{M}} = \delta((\mathbf{r} - \mathbf{r}_S) \cdot \mathbf{n}) \dot{\mathbf{M}}_S \quad (\text{C.24})$$

and arrive at a similar formulation for the electric field as for the magnetic field

$$\boxed{\mathbf{n} \times (\mathbf{E}_1 - \mathbf{E}_2) = -\mu_0 \dot{\mathbf{M}}_S} \quad (\text{C.25})$$

Consequently, the surface magnetization rate  $\dot{\mathbf{M}}_S$  can now be used to create a jump in the electric field.

## C.2. Equivalent source theorem

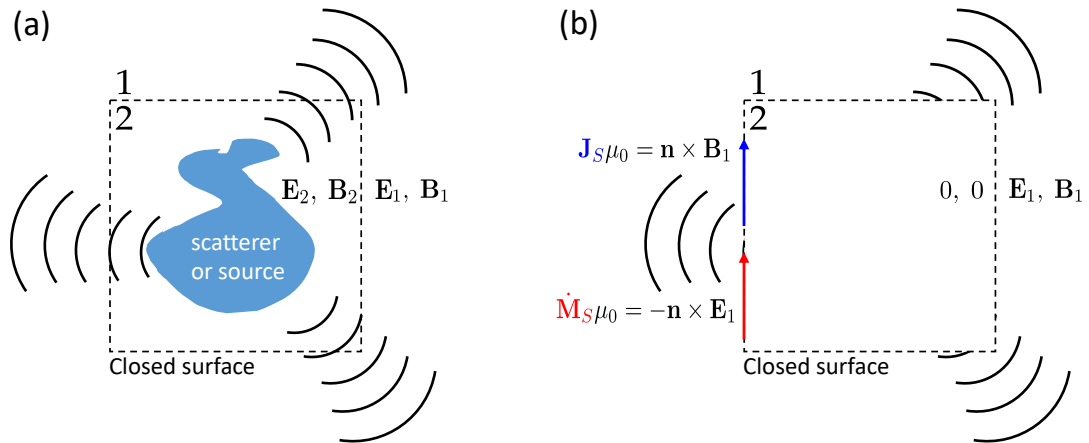


**Figure C.2.:** (adapted from [75]) Principle of the equivalent source theorem: (a) We consider a closed surface around a scatterer (or source) radiating the fields  $\mathbf{E}$  and  $\mathbf{B}$ . (b) We set the fields inside (2) the closed surface to zero, impose  $\dot{\mathbf{M}}_S$  and  $\mathbf{J}_S$  such that the fields outside (1) stay the same. The equivalent scenario does not contain any medium.

Combining the results from the previous subsection we can now use the surface magnetization rate and the surface current to define a so-called *equivalent source* [75] that can reproduce a given field pattern from a scatterer or source, see Fig. C.2 (a). The idea

is that we consider a closed surface where we set the fields inside (region 2)  $\mathbf{B}_2$  and  $\mathbf{E}_2$  zero. With eqs. C.23 and C.25 an appropriate surface current or magnetization rate can be constructed to generate the desired fields outside (region 1) such that the fields stay the same

$$\mathbf{n} \times \mathbf{B}_1 = \mu_0 \mathbf{J}_S \quad (\text{C.26})$$

$$\text{and } \mathbf{n} \times \mathbf{E}_1 = -\mu_0 \dot{\mathbf{M}}_S. \quad (\text{C.27})$$

If region 1 is free of material, we now do not have any medium, only sources. The fields outside are the same as in the original problem. Thus we can use the equivalent scenario to determine the far field using only free-space propagators from the equivalent source currents.

### C.3. Fields from electric and magnetic sources

The derivation on how to evaluate the fields from our given equivalent current and magnetization will be split in three parts. First, we will recall the expression for the electric and magnetic field from a given vector potential in the Lorenz gauge. Second, the vector potential can be spectrally decomposed to inspect each frequency separately. By reformulating the part of the vector potential that is associated with the magnetization, we arrive at a field  $\mathbf{F}$  which we call the *electric vector potential*. Finally, putting together the equivalent source currents and magnetizations with the vector potentials yield us the electric and magnetic fields, where we can take the limit to the far field.

#### Field formulation via potential in Lorenz gauge

We can use the vector potential  $\mathbf{A}$  and the scalar potential  $\Phi$  to describe the fields via [150]

$$\mathbf{E} = -\nabla\phi - \dot{\mathbf{A}} \quad \text{and} \quad \mathbf{B} = \nabla \times \mathbf{A}, \quad (\text{C.28})$$

with the gauge condition of the Lorenz gauge

$$\nabla \cdot \mathbf{A} + \varepsilon_0 \mu_0 \dot{\Phi} = 0 \quad (\text{C.29})$$

Maxwell's equations read

$$\square\Phi = -\frac{\rho}{\varepsilon_0} \quad \text{and} \quad \square\mathbf{A} = -\mu_0 \mathbf{j}. \quad (\text{C.30})$$

Using the gauge condition, the electromagnetic fields can be expressed by only the vector potential

$$\dot{\mathbf{E}} = \frac{1}{\mu_0 \varepsilon_0} \nabla(\nabla \cdot \mathbf{A}) - \ddot{\mathbf{A}} \quad \text{and} \quad \mathbf{B} = \nabla \times \mathbf{A}. \quad (\text{C.31})$$

The electric field is expressed up to a static initial  $\mathbf{E}$  field from a given initial charge distribution, which is not of importance as we are interested in radiating fields only. Consequently we need to find the vector potential from our current density distribution to find the fields.

### Solution of the potential equations for currents and magnetization using spectral decomposition

The general retarded solution for the vector potential resulting from given currents is [150]

$$\mathbf{A}(\mathbf{r}, t) = \frac{\mu_0}{4\pi} \int \frac{\mathbf{j}(\mathbf{r}', t_{\text{ret}})}{|\mathbf{r} - \mathbf{r}'|} d^3r' \quad \text{with} \quad t_{\text{ret}} = t - \frac{|\mathbf{r} - \mathbf{r}'|}{c}. \quad (\text{C.32})$$

If we now consider a spectral decomposition, we can inspect each frequency separately. For a given frequency, all fields can then be written as

$$\mathbf{Y}(\mathbf{r}, t) = \mathbf{Y}(\mathbf{r})e^{-i\omega t}, \quad (\text{C.33})$$

such that the corresponding vector potential becomes

$$\mathbf{A}(\mathbf{r}, t) = \frac{\mu_0}{4\pi} \int \frac{\mathbf{j}(\mathbf{r}')e^{-i\omega t + i\frac{\omega}{c}|\mathbf{r} - \mathbf{r}'|}}{|\mathbf{r} - \mathbf{r}'|} d^3r', \quad (\text{C.34})$$

where we can use  $k = \frac{\omega}{c}$  to formulate a general solution for the spectral component  $\omega$  as

$$\mathbf{A}(\mathbf{r}) = \frac{\mu_0}{4\pi} \int \frac{\mathbf{j}(\mathbf{r}')e^{ik|\mathbf{r} - \mathbf{r}'|}}{|\mathbf{r} - \mathbf{r}'|} d^3r'. \quad (\text{C.35})$$

This general solution is valid for any current and thus also for the surface current  $\mathbf{j}_C$  and the current  $\mathbf{j}_M$  underlying the magnetization. For the latter, however, it is convenient to consider the particular structure of the current for a convenient formulation of the result. We recall the definition C.6

$$\mathbf{j}_M = \nabla \times \mathbf{M} \quad (\text{C.36})$$

and insert this in the general solution, which yields

$$\mathbf{A}_M(\mathbf{r}) = \frac{\mu_0}{4\pi} \int \frac{[\nabla_{\mathbf{r}'} \times \mathbf{M}(\mathbf{r}')] e^{ik|\mathbf{r} - \mathbf{r}'|}}{|\mathbf{r} - \mathbf{r}'|} d^3r'. \quad (\text{C.37})$$

If the integrand vanishes at the boundaries we can pull out the rotation (for more details see Appendix D)

$$\int d^3r' (\nabla_{\mathbf{r}'} \times \mathbf{M}(\mathbf{r}')) \Phi(|\mathbf{r} - \mathbf{r}'|) = \nabla_{\mathbf{r}} \times \int d^3r' \mathbf{M}(\mathbf{r}') \Phi(|\mathbf{r} - \mathbf{r}'|) \quad (\text{C.38})$$

to express the magnetization-based vector potential as

$$\mathbf{A}_M(\mathbf{r}) = \nabla_{\mathbf{r}} \times \underbrace{\frac{\mu_0}{4\pi} \int \frac{\mathbf{M}(\mathbf{r}') e^{ik|\mathbf{r}-\mathbf{r}'|}}{|\mathbf{r} - \mathbf{r}'|} d^3r'}_{\mathbf{F}(\mathbf{r})}, \quad (\text{C.39})$$

where we can identify a field  $\mathbf{F}$  which is called the *electric vector potential*. Note that the resulting  $\mathbf{F}(\mathbf{r}, t)$  would be

$$\mathbf{F}(\mathbf{r}, t) = \frac{\mu_0}{4\pi} \int \frac{\mathbf{M}(\mathbf{r}') e^{i(k|\mathbf{r}-\mathbf{r}'| - \omega t)}}{|\mathbf{r} - \mathbf{r}'|} d^3r' \quad (\text{C.40})$$

and has the structure of a solution of a potential equation

$$\square \mathbf{F}(\mathbf{r}, t) = \left( \Delta - \frac{1}{c^2} \frac{\partial^2}{\partial t^2} \right) \mathbf{F}(\mathbf{r}, t) = -\mu_0 \mathbf{M}(\mathbf{r}, t) \quad (\text{C.41})$$

or in Fourier space (i.e. using our spectral decomposition for  $\omega$  and  $k = \omega/c$ )

$$\square \mathbf{F}(\mathbf{r}) = (\Delta + k^2) \mathbf{F}(\mathbf{r}) = -\mu_0 \mathbf{M}(\mathbf{r}). \quad (\text{C.42})$$

For the Fourier component  $\omega$  we get

$$\mathbf{F}(\mathbf{r}) = \frac{\mu_0}{4\pi} \int \frac{\mathbf{M}(\mathbf{r}') e^{ik|\mathbf{r}-\mathbf{r}'|}}{|\mathbf{r} - \mathbf{r}'|} d^3r' \quad (\text{C.43})$$

and can construct the vector potential associated with the magnetization as

$$\mathbf{A}_M = \nabla \times \mathbf{F}. \quad (\text{C.44})$$

### Field formulation using the equivalent sources

Finally, we need to put together the vector potentials from the current  $\mathbf{j}_C$  and the magnetization  $\mathbf{M}$  using our two solutions. We consider our surface current and magnetization to transform the volume integrals into surface integrals using Stokes' theorem

$$\mathbf{A}_j(\mathbf{r}) = \frac{\mu_0}{4\pi} \int_V \frac{\mathbf{j}_C(\mathbf{r}') e^{ik|\mathbf{r}-\mathbf{r}'|}}{|\mathbf{r}-\mathbf{r}'|} d^3r' = \frac{\mu_0}{4\pi} \iint_S \frac{\mathbf{J}_S(\mathbf{r}') e^{ik|\mathbf{r}-\mathbf{r}'|}}{|\mathbf{r}-\mathbf{r}'|} d\mathbf{f}' \quad (\text{C.45})$$

and

$$\mathbf{F}_M(\mathbf{r}) = \frac{\mu_0}{4\pi} \int \frac{\mathbf{M}(\mathbf{r}') e^{ik|\mathbf{r}-\mathbf{r}'|}}{|\mathbf{r}-\mathbf{r}'|} d^3r' = \frac{\mu_0}{4\pi} \iint_S \frac{\mathbf{M}_S(\mathbf{r}') e^{ik|\mathbf{r}-\mathbf{r}'|}}{|\mathbf{r}-\mathbf{r}'|} d\mathbf{f}'. \quad (\text{C.46})$$

We already see that from  $\dot{\mathbf{M}}_S$ , which we get directly from the equivalence analysis, we will be able to find  $\dot{\mathbf{F}}_M$ . Fields are constructed using

$$\dot{\mathbf{E}} = c^2 \nabla(\nabla \cdot \mathbf{A}) - \ddot{\mathbf{A}} \quad \text{and} \quad \mathbf{B} = \nabla \times \mathbf{A} \quad (\text{C.47})$$

with  $\mathbf{A} = \mathbf{A}_j + \nabla \times \mathbf{F}_M$  and using the spectral representation for derivatives w.r.t. time ( $\partial_t = -i\omega$ ). For the electric field we have

$$-i\omega \mathbf{E}(\mathbf{r}) = c^2 \nabla(\nabla \cdot \mathbf{A}_j) - (-i\omega)^2 \mathbf{A}_j - (-i\omega) \nabla \times \dot{\mathbf{F}}_M \quad (\text{C.48})$$

and after some rearrangement and using  $\omega = ck$

$$\mathbf{E}(\mathbf{r}) = i\omega \left( \frac{1}{k^2} \nabla(\nabla \cdot \mathbf{A}_j) + \mathbf{A}_j \right) - \nabla \times \dot{\mathbf{F}}_M. \quad (\text{C.49})$$

For the magnetic field we have

$$\mathbf{B}(\mathbf{r}) = \nabla \times \mathbf{A}_j + \nabla \times \nabla \times \mathbf{F}_M \quad (\text{C.50})$$

using  $\text{rot rot} = \text{grad div} - \Delta$  we get

$$\mathbf{B}(\mathbf{r}) = \nabla \times \mathbf{A}_j + \nabla(\nabla \cdot \mathbf{F}_M) - \Delta \mathbf{F}_M \quad (\text{C.51})$$

and using the potential equation for  $\mathbf{F}$  (Eq. C.42) and considering only evaluation points with  $\mathbf{M} = 0$  (which is the case outside of our equivalent source)

$$\mathbf{B}(\mathbf{r}) = \nabla \times \mathbf{A}_j + \nabla(\nabla \cdot \mathbf{F}_M) + k^2 \mathbf{F}_M, \quad (\text{C.52})$$

we now use  $\mathbf{F}_M = \frac{1}{-i\omega} \dot{\mathbf{F}}_M$  to rewrite this as

$$\mathbf{B}(\mathbf{r}) = \frac{i\omega}{c^2} \left( \frac{1}{k^2} \nabla(\nabla \cdot \dot{\mathbf{F}}_M) + \dot{\mathbf{F}}_M \right) + \nabla \times \mathbf{A}_j. \quad (\text{C.53})$$

We now derived expressions to calculate the electric and magnetic field from the vector potentials, which themselves stem from integrating the surface currents (and surface magnetizations). The next step will be to evaluate the far field using those relations.

#### C.4. Evaluation of the far field

To sum up the previous calculations, we have the current-based and electric vector potentials

$$\mathbf{A}_j(\mathbf{r}) = \frac{\mu_0}{4\pi} \iint_S \frac{\mathbf{J}_S(\mathbf{r}') e^{ik|\mathbf{r}-\mathbf{r}'|}}{|\mathbf{r}-\mathbf{r}'|} d\mathbf{f}' \quad \text{and} \quad \mathbf{F}_M(\mathbf{r}) = \frac{\mu_0}{4\pi} \iint_S \frac{\mathbf{M}_S(\mathbf{r}') e^{ik|\mathbf{r}-\mathbf{r}'|}}{|\mathbf{r}-\mathbf{r}'|} d\mathbf{f}' \quad (\text{C.54})$$

and must evaluate

$$\mathbf{E}(\mathbf{r}) = i\omega \left( \frac{1}{k^2} \nabla(\nabla \cdot \mathbf{A}_j) + \mathbf{A}_j \right) - \nabla \times \dot{\mathbf{F}}_M \quad (\text{C.55})$$

$$\mathbf{B}(\mathbf{r}) = \frac{i\omega}{c^2} \left( \frac{1}{k^2} \nabla(\nabla \cdot \dot{\mathbf{F}}_M) + \dot{\mathbf{F}}_M \right) + \nabla \times \mathbf{A}_j, \quad (\text{C.56})$$

which is cumbersome in full generality. As we are interested only in the far field, we can simplify the potentials Eq. C.54.

$$|\mathbf{r} - \mathbf{r}'| = \sqrt{r^2 - 2r r' \cos \gamma_{r,r'} + r'^2} = r \sqrt{1 - \frac{2r'}{r} \cos \gamma_{r,r'} + \frac{r'^2}{r^2}}, \quad (\text{C.57})$$

where  $r = |\mathbf{r}|$  is the absolute value of the position vector and  $\gamma_{r,r'}$  the angle between  $\mathbf{r}$  and  $\mathbf{r}'$ .

Taylor expansion w.r.t.  $\mathbf{r}'$  up to first order (e.g. for the case  $r' \ll r$  and  $\sqrt{1+x} \approx 1 + \frac{x}{2}$ ) yields

$$|\mathbf{r} - \mathbf{r}'| \approx r \left( 1 - \frac{r'}{r} \cos \gamma_{r,r'} + \frac{r'^2}{r^2} \right) \quad (\text{C.58})$$

$$= r - r' \cos \gamma_{r,r'}, \quad (\text{C.59})$$

in the denominator (signal scaling), we only need to include the leading term, which will completely dominate the signal scaling. In the integrand we use both terms and get (for the example of  $\mathbf{A}_j$ )

$$\mathbf{A}_j(\mathbf{r}) = \frac{\mu_0}{4\pi} \frac{e^{ikr}}{r} \underbrace{\iint_S \mathbf{J}_S(\mathbf{r}') e^{-ikr' \cos \gamma_{r,r'}} d\mathbf{f}'}_{\mathbf{L}(\mathbf{r})}, \quad (\text{C.60})$$

the structure resulting from  $\mathbf{F}_M$  is analogous.

$$\mathbf{F}_M(\mathbf{r}) = \frac{\mu_0}{4\pi} \frac{e^{ikr}}{r} \underbrace{\iint_S \mathbf{M}_S(\mathbf{r}') e^{-ikr' \cos \gamma_{r,r'}} d\mathbf{f}'}_{\mathbf{N}(\mathbf{r})}. \quad (\text{C.61})$$

Note that the dependence of the integral regarding  $\mathbf{r}$  results only from the cosine in the exponent, which can be conveniently expressed as

$$\cos \gamma_{r,r'} = \mathbf{e}_{r'} \cdot \mathbf{e}_r = \mathbf{e}_{r'} \cdot \mathbf{e}_r(\vartheta, \varphi). \quad (\text{C.62})$$

As a result we get

$$\mathbf{L}(\mathbf{r}) = \mathbf{L}(\vartheta, \varphi) \quad \text{and} \quad \mathbf{N}(\mathbf{r}) = \mathbf{N}(\vartheta, \varphi), \quad (\text{C.63})$$

where the angles  $\vartheta, \varphi$  characterize the direction of the observation point. From the structure of the nabla operator in spherical coordinates

$$\nabla = \underbrace{\begin{pmatrix} \sin \vartheta \cos \varphi \\ \sin \vartheta \sin \varphi \\ \cos \vartheta \end{pmatrix}}_{\mathbf{e}_r} \frac{\partial}{\partial r} + \underbrace{\begin{pmatrix} \frac{\cos \vartheta \cos \varphi}{r} \\ \frac{\cos \vartheta \sin \varphi}{r} \\ -\frac{\sin \vartheta}{r} \end{pmatrix}}_{\frac{\mathbf{e}_\vartheta}{r}} \frac{\partial}{\partial \vartheta} + \underbrace{\begin{pmatrix} -\frac{\sin \varphi}{r \sin \vartheta} \\ \frac{\cos \varphi}{r \sin \vartheta} \\ 0 \end{pmatrix}}_{\frac{\mathbf{e}_\varphi}{r \sin \vartheta}} \frac{\partial}{\partial \varphi}, \quad (\text{C.64})$$

we further see that, when applied to the above expressions for  $\mathbf{A}_j$  and  $\mathbf{F}_M$ , only the first term (radial part) can create terms with  $1/r$  - the other ones yields contributions that decay at least with  $1/r^2$ . The leading term is

$$\nabla \cdot \mathbf{A}_j = \frac{\mu_0}{4\pi} \frac{ik e^{ikr}}{r} \mathbf{e}_r \cdot \mathbf{L}(\vartheta, \varphi). \quad (\text{C.65})$$

The gradient of this again leads to leading terms associated only with  $\mathbf{e}_r$

$$\nabla (\nabla \cdot \mathbf{A}_j) = \mathbf{e}_r \frac{\mu_0}{4\pi} \frac{-k^2 e^{ikr}}{r} \mathbf{e}_r \cdot \mathbf{L}(\vartheta, \varphi) = -k^2 \mathbf{e}_r (\mathbf{e}_r \cdot \mathbf{A}_j), \quad (\text{C.66})$$

which is just the scaled radial component of  $\mathbf{A}_j$ . As a result, contributions of the form

$$\left( \frac{1}{k^2} \nabla (\nabla \cdot \mathbf{A}_j) + \mathbf{A}_j \right) \quad (\text{C.67})$$

have no radial contributions as the first term subtracts them out. Hence, we only need to consider the angular components. For the remaining contribution  $\nabla \times \mathbf{F}_M$  an analogous argument can be made - only the derivatives w.r.t. the radial coordinate are

non-negligible (which excludes the radial coordinate itself in a vector product). We get

$$\nabla \times \mathbf{F}_M = \mathbf{e}_\varphi \frac{\partial}{\partial r} [\mathbf{e}_\vartheta \cdot \mathbf{F}_M] - \mathbf{e}_\vartheta \frac{\partial}{\partial r} [\mathbf{e}_\varphi \cdot \mathbf{F}_M] \quad (\text{C.68})$$

$$\begin{aligned} &= \frac{\mu_0}{4\pi} \frac{ik}{r} e^{ikr} (\mathbf{e}_\varphi \mathbf{e}_\vartheta \cdot \mathbf{N}(\vartheta, \varphi) - \mathbf{e}_\vartheta \mathbf{e}_\varphi \cdot \mathbf{N}(\vartheta, \varphi)) \\ &= \mathbf{e}_\varphi ikF_{M,\vartheta} - \mathbf{e}_\vartheta ikF_{M,\varphi}, \end{aligned} \quad (\text{C.69})$$

hence we finally have

$$E_\vartheta = i\omega A_{j,\vartheta} + ik\dot{F}_{M,\varphi} = ik \frac{\mu_0}{4\pi} \frac{e^{ikr}}{r} (cL_\vartheta + \dot{N}_\varphi) \quad (\text{C.70})$$

$$E_\varphi = i\omega A_{j,\varphi} - ik\dot{F}_{M,\vartheta} = ik \frac{\mu_0}{4\pi} \frac{e^{ikr}}{r} (cL_\varphi - \dot{N}_\vartheta). \quad (\text{C.71})$$

The magnetic field follows analogously as

$$B_\vartheta = \frac{i\omega}{c^2} \dot{F}_{M,\vartheta} - ikA_{j,\varphi} = -ik \frac{\mu_0}{4\pi} \frac{e^{ikr}}{r} \left( L_\varphi - \frac{\dot{N}_\vartheta}{c} \right) = -\frac{E_\varphi}{c} \quad (\text{C.72})$$

$$B_\varphi = \frac{i\omega}{c^2} \dot{F}_{M,\varphi} + ikA_{j,\vartheta} = ik \frac{\mu_0}{4\pi} \frac{e^{ikr}}{r} \left( L_\vartheta + \frac{\dot{N}_\varphi}{c} \right) = \frac{E_\vartheta}{c}, \quad (\text{C.73})$$

where the correct relation between  $\mathbf{E}$  and  $\mathbf{B}$  according to  $\mathbf{B} = \mathbf{k} \times \mathbf{E}$  verifies consistence. For a given sample point in the far field with direction  $\vartheta, \varphi$  and corresponding unit vectors  $\mathbf{e}_{\vartheta/\varphi/r}$  the fields  $L$  and  $\dot{N}$  follow as

$$L_{\vartheta/\varphi}(\vartheta, \varphi) = \iint_S [\mathbf{e}_{\vartheta/\varphi} \cdot \mathbf{J}_S(\mathbf{r}')] e^{-ikr' \mathbf{e}_r \cdot \mathbf{e}_{r'}} d\mathbf{f}' \quad (\text{C.74})$$

$$\dot{N}_{\vartheta/\varphi}(\vartheta, \varphi) = \iint_S [\mathbf{e}_{\vartheta/\varphi} \cdot \dot{\mathbf{M}}_S(\mathbf{r}')] e^{-ikr' \mathbf{e}_r \cdot \mathbf{e}_{r'}} d\mathbf{f}'. \quad (\text{C.75})$$

It becomes apparent that for the calculation of the electromagnetic fields, the surface current  $\mathbf{J}_S$  and the surface magnetization rate  $\dot{\mathbf{M}}_S$  (and not the magnetization current density  $\mathbf{j}_M$ ) are required, which are given directly by the equivalent source (Eqs. C.26 and C.27). The scattering intensity follows from the electric and magnetic fields as the time-averaged Poynting vector. Note, that the evaluation of the fields is done spectrally selective, which results in spectrally selected intensities in the far-field.

$$\langle \mathbf{S} \rangle = \frac{1}{\mu_0} \text{Re} \left( \frac{1}{2} \mathbf{E} \times \mathbf{B} \right) \quad (\text{C.76})$$

$$= \frac{1}{\mu_0} \left( \frac{1}{2} \text{Re} (E_\vartheta B_\varphi^*) - \frac{1}{2} \text{Re} (E_\varphi B_\vartheta^*) \right) \quad (\text{C.77})$$

$$= \frac{1}{2\mu_0 c} (|E_\vartheta|^2 + |E_\varphi|^2) \quad (\text{C.78})$$

$$= \frac{\mu_0 k^2}{32\pi^2 r^2 c} (|cL_\vartheta + \dot{N}_\varphi|^2 + |cL_\varphi - \dot{N}_\vartheta|^2) \equiv P_{\text{scat}}(\vartheta, \varphi), \quad (\text{C.79})$$

where  $P_{\text{scat}}(\vartheta, \varphi)$  is the scattered power at a given scattering direction.

## D. Additional calculation for the magnetization-based vector potential

Our goal is to pull out the rotation from the integral to get a similar expression for the vector potential for the magnetization based current  $\mathbf{j}_M = \nabla \times \mathbf{M}$  as we have for the surface current  $\mathbf{j}_C$ . To this end, we have to get rid of the rotation acting on the primed variables inside the integral in Eq. C.37. We start with a more general formulation of that equation

$$\int d^3r' (\nabla_{\mathbf{r}'} \times \mathbf{M}(\mathbf{r}')) \Phi(|\mathbf{r} - \mathbf{r}'|) \quad (\text{D.1})$$

and make use of the vector identity

$$(\nabla \times \mathbf{M})\Phi = \nabla \times (\Phi\mathbf{A}) - (\nabla\Phi) \times \mathbf{M}. \quad (\text{D.2})$$

Inserting these equations into each other yields

$$\int d^3r' \left[ \nabla_{\mathbf{r}'} \times (\mathbf{M}(\mathbf{r}')\Phi(|\mathbf{r} - \mathbf{r}'|)) - \underbrace{(\nabla_{\mathbf{r}'}\Phi(|\mathbf{r} - \mathbf{r}'|)) \times \mathbf{M}(\mathbf{r}')}_{= -\nabla_{\mathbf{r}}\Phi(|\mathbf{r} - \mathbf{r}'|)} \right], \quad (\text{D.3})$$

where we used the chain rule in the second part of the brackets.

For the first part, we can use a special case of the divergence theorem

$$\int d^3r' \nabla_{\mathbf{r}'} \times (\mathbf{M}(\mathbf{r}')\Phi(|\mathbf{r} - \mathbf{r}'|)) \quad (\text{D.4})$$

$$= \iint_S (\mathbf{M}(\mathbf{r}')\Phi(|\mathbf{r} - \mathbf{r}'|)) \times d\mathbf{f}' \quad (\text{where } \mathbf{f}' \text{ is the surface of the volume}). \quad (\text{D.5})$$

As  $\Phi(|\mathbf{r} - \mathbf{r}'|)$  decays as  $\propto \frac{1}{|\mathbf{r} - \mathbf{r}'|}$  and  $\mathbf{M}$  is finite, this integral vanishes.

Continuing with Eq. D.3, we use the same vector identity as above again

$$\int d^3r' (\nabla_{\mathbf{r}}\Phi(|\mathbf{r} - \mathbf{r}'|)) \times \mathbf{M}(\mathbf{r}') \quad (\text{D.6})$$

$$= \nabla_{\mathbf{r}} \times \int d^3r' \Phi(|\mathbf{r} - \mathbf{r}'|) \mathbf{M}(\mathbf{r}') - \int d^3r' \Phi(|\mathbf{r} - \mathbf{r}'|) \underbrace{(\nabla_{\mathbf{r}} \times \mathbf{M}(\mathbf{r}'))}_{=0}, \quad (\text{D.7})$$

where the last term vanishes as the magnetization only depends on the primed spatial vector  $\mathbf{r}'$ . The end result of this additional calculation is the  $\nabla$  operator being pulled out of the integral and now acting on  $\mathbf{r}$  instead of  $\mathbf{r}'$ .

## E. Atomic polarizability vs. susceptibility

In subsection 4.1.2, the local field at a test atom was derived as

$$E_{\text{loc}} = E_M + E_{\text{Lorentz}} \quad (\text{E.1})$$

$$= -\frac{N_P}{\varepsilon_0}P + E_{\text{ex}} + \frac{1}{3\varepsilon_0}P. \quad (\text{E.2})$$

The microscopic response of the single dipole with the dipole moment  $d$  to the local electric field is referred to as the atomic polarizability  $\alpha$

$$\alpha(\omega) = \frac{d(\omega)}{E_{\text{loc}}(\omega)}. \quad (\text{E.3})$$

The electric field in Maxwell's equations is the average over the local varying fields, or macroscopic field  $E_M$ . The macroscopic response of the dipole density  $P(\omega) = n_0 d(\omega)$  ( $n_0$  : particle number density) to the macroscopic field is called susceptibility  $\chi$

$$\chi(\omega) = \frac{P(\omega)}{\varepsilon_0 E_M(\omega)}. \quad (\text{E.4})$$

It is connected to the permittivity  $\varepsilon_r(\omega) = 1 + \chi(\omega)$  and consequently to the refractive index  $n^2 = \varepsilon_r$ . Combining equations E.3 and E.4 with the definition of the polarization yields

$$n_0 \alpha E_{\text{loc}} = \chi \varepsilon_0 E_M \quad (\text{E.5})$$

$$n_0 \alpha (E_M + E_{\text{Lorentz}}) = \chi \varepsilon_0 E_M$$

$$n_0 \alpha \left( E_M + \frac{1}{3\varepsilon_0} P \right) = \chi \varepsilon_0 E_M$$

$$n_0 \alpha \left( 1 + \frac{1}{3} \chi \right) = \chi \varepsilon_0$$

$$\chi = \frac{3n_0 \alpha}{3\varepsilon_0 - n_0 \alpha}, \quad (\text{E.6})$$

which is the Clausius-Mossotti-equation [79], that relates the atomic polarizability (microscopic response) to the susceptibility (macroscopic response).

# Bibliography

- [1] R. E. Franklin and R. G. Gosling, *Molecular configuration in sodium thymonucleate*, [Nature](#) **171**, 740–741 (1953).
- [2] J. D. Watson and F. H. Crick, *Molecular structure of nucleic acids: a structure for deoxyribose nucleic acid*, [Nature](#) **171**, 737–738 (1953).
- [3] J. Feldhaus, J. Arthur and J. B. Hastings, *X-ray free-electron lasers*, [J. Phys. B: At. Mol. Opt. Phys.](#) **38**, S799–S819 (2005).
- [4] W. a. Ackermann, G. Asova, V. Ayvazyan, A. Azima, N. Baboi, J. Bähr, V. Balandin, B. Beutner, A. Brandt, A. Bolzmann et al., *Operation of a free-electron laser from the extreme ultraviolet to the water window*, [Nature Photonics](#) **1**, 336–342 (2007).
- [5] P. Emma, R. Akre, J. Arthur, R. Bionta, C. Bostedt, J. Bozek, A. Brachmann, P. Bucksbaum, R. Coffee, F.-J. Decker et al., *First lasing and operation of an ångstrom-wavelength free-electron laser*, [Nature Photonics](#) **4**, 641–647 (2010).
- [6] H. Wabnitz, *Multiple ionization of atom clusters by intense soft X-rays from a free- electron laser*, [Nature \(London\)](#) **420**, 482–485 (2002).
- [7] C. Bostedt, S. Boutet, D. M. Fritz, Z. Huang, H. J. Lee, H. T. Lemke, A. Robert, W. F. Schlotter, J. J. Turner and G. J. Williams, *Linac coherent light source: The first five years*, [Reviews of Modern Physics](#) **88**, 015007 (2016).
- [8] E. Allaria, D. Castronovo, P. Cinquegrana, P. Craievich, M. Dal Forno, M. Danailov, G. D’Auria, A. Demidovich, G. De Ninno, S. Di Mitri et al., *Two-stage seeded soft-X-ray free-electron laser*, [Nature Photonics](#) **7**, 913–918 (2013).
- [9] H. Ostrom, H. Oberg, H. Xin, J. LaRue, M. Beye, M. Dell’Angela, J. Gladh, M. L. Ng, J. A. Sellberg, S. Kaya, G. Mercurio, D. Nordlund, M. Hantschmann, F. Hieke, D. Kuhn, W. F. Schlotter, G. L. Dakovski, J. J. Turner, M. P. Minitti, A. Mitra, S. P. Moeller, A. Fohlisch, M. Wolf, W. Wurth, M. Persson, J. K. Nørskov, F. Abild-Pedersen, H. Ogasawara, L. G. M. Pettersson and A. Nilsson, *Probing the transition state region in catalytic CO oxidation on Ru*, [Science](#) **347**, 978–982 (2015).
- [10] K. Gaffney and H. N. Chapman, *Imaging atomic structure and dynamics with ultrafast X-ray scattering*, [Science](#) **316**, 1444–1448 (2007).

- [11] R. Neutze, R. Wouts, D. van der Spoel, E. Weckert and J. Hajdu, *Potential for biomolecular imaging with femtosecond X-ray pulses*, *Nature* **406**, 752–757 (2000).
- [12] H. N. Chapman, P. Fromme, A. Barty, T. A. White, R. A. Kirian, A. Aquila, M. S. Hunter, J. Schulz, D. P. DePonte, U. Weierstall, R. B. Doak, F. R. N. C. Maia, A. V. Martin, I. Schlichting, L. Lomb, N. Coppola, R. L. Shoeman, S. W. Epp, R. Hartmann, D. Rolles, A. Rudenko, L. Foucar, N. Kimmel, G. Weidenspointner, P. Holl, M. Liang, M. Barthelmess, C. Caleman, S. Boutet, M. J. Bogan, J. Krzywinski, C. Bostedt, S. Bajt, L. Gumprecht, B. Rudek, B. Erk, C. Schmidt, A. Hömke, C. Reich, D. Pietschner, L. Strüder, G. Hauser, H. Gorke, J. Ullrich, S. Herrmann, G. Schaller, F. Schopper, H. Soltau, K.-U. Kühnel, M. Messerschmidt, J. D. Bozek, S. P. Hau-Riege, M. Frank, C. Y. Hampton, R. G. Sierra, D. Starodub, G. J. Williams, J. Hajdu, N. Timneanu, M. M. Seibert, J. Andreasson, A. Rucker, O. Jönsson, M. Svenda, S. Stern, K. Nass, R. Andritschke, C.-D. Schröter, F. Krasniqi, M. Bott, K. E. Schmidt, X. Wang, I. Grotjohann, J. M. Holton, T. R. M. Barends, R. Neutze, S. Marchesini, R. Fromme, S. Schorb, D. Rupp, M. Adolph, T. Gorkhover, I. Andersson, H. Hirsemann, G. Potdevin, H. Graafsma, B. Nilsson and J. C. H. Spence, *Femtosecond X-ray protein nanocrystallography*, *Nature* **470**, 73–77 (2011).
- [13] C. Bostedt, E. Eremina, D. Rupp, M. Adolph, H. Thomas, M. Hoener, A. R. de Castro, J. Tiggesbäumker, K.-H. Meiwes-Broer, T. Laarmann et al., *Ultrafast x-ray scattering of xenon nanoparticles: imaging transient states of matter*, *Physical review letters* **108**, 093401 (2012).
- [14] T. Gorkhover, M. Adolph, D. Rupp, S. Schorb, S. W. Epp, B. Erk, L. Foucar, R. Hartmann, N. Kimmel, K.-U. Kühnel, D. Rolles, B. Rudek, A. Rudenko, R. Andritschke, A. Aquila, J. D. Bozek, N. Coppola, T. Erke, F. Filsinger, H. Gorke, H. Graafsma, L. Gumprecht, G. Hauser, S. Herrmann, H. Hirsemann, A. Hömke, P. Holl, C. Kaiser, F. Krasniqi, J.-H. Meyer, M. Matysek, M. Messerschmidt, D. Miessner, B. Nilsson, D. Pietschner, G. Potdevin, C. Reich, G. Schaller, C. Schmidt, F. Schopper, C. D. Schröter, J. Schulz, H. Soltau, G. Weidenspointner, I. Schlichting, L. Strüder, J. Ullrich, T. Möller and C. Bostedt, *Nanoplasma Dynamics of Single Large Xenon Clusters Irradiated with Superintense X-Ray Pulses from the Linac Coherent Light Source Free-Electron Laser*, *Phys. Rev. Lett.* **108**, (2012).
- [15] S. Lipson, H. Lipson and D. Tannhauser, *Optical Physics*, Cambridge University Press (1995), ISBN: 9780521436311.
- [16] S. K. Sinha, E. B. Sirota, S. Garoff and H. B. Stanley, *X-ray and neutron scattering from rough surfaces*, *Phys. Rev. B* **38**, 2297–2311 (1988).
- [17] R. W. Gerchberg, *A practical algorithm for the determination of plane from image and diffraction pictures*, *Optik* **35**, 237–246 (1972).

- [18] J. R. Fienup, *Reconstruction of an object from the modulus of its Fourier transform*, [Optics letters](#) **3**, 27–29 (1978).
- [19] J. R. Fienup, *Phase retrieval algorithms: a comparison*, [Appl. Opt.](#) **21**, 2758–2769 (1982).
- [20] Y. Shechtman, Y. C. Eldar, O. Cohen, H. N. Chapman, J. Miao and M. Segev, *Phase retrieval with application to optical imaging: a contemporary overview*, [IEEE signal processing magazine](#) **32**, 87–109 (2015).
- [21] M. M. Seibert, T. Ekeberg, F. R. Maia, M. Svenda, J. Andreasson, O. Jönsson, D. Odić, B. Iwan, A. Rocker, D. Westphal et al., *Single mimivirus particles intercepted and imaged with an X-ray laser*, [Nature](#) **470**, 78–81 (2011).
- [22] L. F. Gomez, K. R. Ferguson, J. P. Cryan, C. Bacellar, R. M. P. Tanyag, C. Jones, S. Schorb, D. Anielski, A. Belkacem, C. Bernando, R. Boll, J. Bozek, S. Carron, G. Chen, T. Delmas, L. Englert, S. W. Epp, B. Erk, L. Foucar, R. Hartmann, A. Hexemer, M. Huth, J. Kwok, S. R. Leone, J. H. S. Ma, F. R. N. C. Maia, E. Malmerberg, S. Marchesini, D. M. Neumark, B. Poon, J. Prell, D. Rolles, B. Rudek, A. Rudenko, M. Seifrid, K. R. Siefertmann, F. P. Sturm, M. Swiggers, J. Ullrich, F. Weise, P. Zwart, C. Bostedt, O. Gessner and A. F. Vilesov, *Shapes and vorticities of superfluid helium nanodroplets*, [Science](#) **345**, 906–909 (2014).
- [23] A. J. Feinberg, F. Laimer, R. M. P. Tanyag, B. Senfftleben, Y. Ovcharenko, S. Dold, M. Gatchell, S. M. O’Connell-Lopez, S. Erukala, C. A. Saladrigas et al., *X-ray diffractive imaging of highly ionized helium nanodroplets*, [Physical Review Research](#) **4**, L022063 (2022).
- [24] T. Gorkhover, A. Ulmer, K. Ferguson, M. Bucher, F. R. Maia, J. Bielecki, T. Ekeberg, M. F. Hantke, B. J. Daurer, C. Nettelblad et al., *Femtosecond X-ray Fourier holography imaging of free-flying nanoparticles*, [Nature Photonics](#) **12**, 150–153 (2018).
- [25] I. Barke, H. Hartmann, D. Rupp, L. Flückiger, M. Sauppe, M. Adolph, S. Schorb, C. Bostedt, R. Treusch, C. Peltz, S. Bartling, T. Fennel, K.-H. Meiwes-Broer and T. Möller, *The 3D-architecture of individual free silver nanoparticles captured by X-ray scattering*, [Nature Communications](#) **6**, 6187 (2015).
- [26] B. Langbehn, K. Sander, Y. Ovcharenko, C. Peltz, A. Clark, M. Coreno, R. Cucini, M. Drabbels, P. Finetti, M. Di Fraia et al., *Three-dimensional shapes of spinning helium nanodroplets*, [Physical review letters](#) **121**, 255301 (2018).
- [27] G. Mie, *Beiträge zur Optik trüber Medien, speziell kolloidaler Metallösungen*, [Ann. Phys.](#) **330**, 377–445 (1908).
- [28] E. M. Purcell and C. R. Pennypacker, *Scattering and Absorption of Light by Nonspherical Dielectric Grains*, [ApJ](#) **186**, 705 (1973).

- [29] K. Sander, C. Peltz, C. Varin, S. Scheel, T. Brabec and T. Fennel, *Influence of wavelength and pulse duration on single-shot x-ray diffraction patterns from nonspherical nanoparticles*, [J. Phys. B: At. Mol. Opt. Phys.](#) **48**, 204004 (2015).
- [30] K. S. Yee et al., *Numerical solution of initial boundary value problems involving Maxwell's equations in isotropic media*, [IEEE Trans. Antennas Propag](#) **14**, 302–307 (1966).
- [31] T. Stielow and S. Scheel, *Reconstruction of nanoscale particles from single-shot wide-angle free-electron-laser diffraction patterns with physics-informed neural networks*, [Physical Review E](#) **103**, 053312 (2021).
- [32] D. Rupp, N. Monserud, B. Langbehn, M. Sauppe, J. Zimmermann, Y. Ovcharenko, T. Möller, F. Frassetto, L. Poletto, A. Trabattoni et al., *Coherent diffractive imaging of single helium nanodroplets with a high harmonic generation source*, [Nature communications](#) **8**, 493 (2017).
- [33] S. H. Autler and C. H. Townes, *Stark effect in rapidly varying fields*, [Physical Review](#) **100**, 703 (1955).
- [34] B. R. Mollow, *Power Spectrum of Light Scattered by Two-Level Systems*, [Phys. Rev.](#) **188**, 1969–1975 (1969).
- [35] S. E. Harris, J. Field and A. Imamoglu, *Nonlinear optical processes using electromagnetically induced transparency*, [Physical Review Letters](#) **64**, 1107 (1990).
- [36] P. J. Ho, B. J. Daurer, M. F. Hantke, J. Bielecki, A. Al Haddad, M. Bucher, G. Doumy, K. R. Ferguson, L. Flückiger, T. Gorkhover et al., *The role of transient resonances for ultra-fast imaging of single sucrose nanoclusters*, [Nature communications](#) **11**, 167 (2020).
- [37] C. Peltz, C. Varin, T. Brabec and T. Fennel, *Time-Resolved X-Ray Imaging of Anisotropic Nanoplasma Expansion*, [Phys. Rev. Lett.](#) **113**, (2014).
- [38] R. Schneider, T. Mehringer, G. Mercurio, L. Wenthaus, A. Classen, G. Brenner, O. Gorobtsov, A. Benz, D. Bhatti, L. Bocklage et al., *Quantum imaging with incoherently scattered light from a free-electron laser*, [Nature Physics](#) **14**, 126–129 (2018).
- [39] A. Classen, K. Ayyer, H. N. Chapman, R. Röhlberger and J. von Zanthier, *Incoherent diffractive imaging via intensity correlations of hard x rays*, [Physical review letters](#) **119**, 053401 (2017).
- [40] A. Benediktovitch, V. P. Majety and N. Rohringer, *Quantum theory of superfluorescence based on two-point correlation functions*, [Physical Review A](#) **99**, 013839 (2019).
- [41] S. Chen, M. Wu, M. B. Gaarde and K. J. Schafer, *Quantum interference in attosecond transient absorption of laser-dressed helium atoms*, [Physical Review A](#)

- [87](#), 033408 (2013).
- [42] M. Wu, S. Chen, S. Camp, K. J. Schafer and M. B. Gaarde, *Theory of strong-field attosecond transient absorption*, [Journal of Physics B: Atomic, Molecular and Optical Physics](#) **49**, 062003 (2016).
- [43] A. Aspect, G. Roger, S. Reynaud, J. Dalibard and C. Cohen-Tannoudji, *Time correlations between the two sidebands of the resonance fluorescence triplet*, [Physical Review Letters](#) **45**, 617 (1980).
- [44] F. Schuda, C. Stroud Jr and M. Hercher, *Observation of the resonant Stark effect at optical frequencies*, [Journal of Physics B: Atomic and Molecular Physics](#) **7**, L198 (1974).
- [45] F. Wu, R. Grove and S. Ezekiel, *Investigation of the spectrum of resonance fluorescence induced by a monochromatic field*, [Physical Review Letters](#) **35**, 1426 (1975).
- [46] R. Grove, F. Wu and S. Ezekiel, *Measurement of the spectrum of resonance fluorescence from a two-level atom in an intense monochromatic field*, [Physical Review A](#) **15**, 227 (1977).
- [47] W. Hartig, W. Rasmussen, R. Schieder and H. Walther, *Study of the frequency distribution of the fluorescent light induced by monochromatic radiation*, [Zeitschrift für Physik A Atoms and Nuclei](#) **278**, 205–210 (1976).
- [48] A. N. Pfeiffer and S. R. Leone, *Transmission of an isolated attosecond pulse in a strong-field dressed atom*, [Physical Review A](#) **85**, 053422 (2012).
- [49] M. Wu, S. Chen, M. B. Gaarde and K. J. Schafer, *Time-domain perspective on Autler-Townes splitting in attosecond transient absorption of laser-dressed helium atoms*, [Physical Review A](#) **88**, 043416 (2013).
- [50] S. Chen, M. J. Bell, A. R. Beck, H. Mashiko, M. Wu, A. N. Pfeiffer, M. B. Gaarde, D. M. Neumark, S. R. Leone and K. J. Schafer, *Light-induced states in attosecond transient absorption spectra of laser-dressed helium*, [Physical Review A](#) **86**, 063408 (2012).
- [51] R. Boyd and D. Prato, *Nonlinear Optics*, Elsevier Science (2008), ISBN: 9780080485966.
- [52] P. Zeeman, *Ueber einen Einfluss der Magnetisirung auf die Natur des von einer Substanz emittirten Lichtes*, Verhandlungen der Physikalischen Gesellschaft zu Berlin , (1896).
- [53] H. Haken and H. C. Wolf, *Atom-und Quantenphysik: Einführung in die experimentellen und theoretischen Grundlagen*, Springer-Verlag (2013), ISBN: 978-3-540-02621-1.

- [54] T. Hezel, C. Burkhardt, M. Ciocca and J. Leventhal, *Classical view of the Stark effect in hydrogen atoms*, [American Journal of Physics](#) **60**, 324–328 (1992).
- [55] R. V. Krems, *Molecules in electromagnetic fields: from ultracold physics to controlled chemistry*, John Wiley & Sons (2018), ISBN: 9781119382638.
- [56] W. Demtröder, *Experimentalphysik 3: Atome, Moleküle und Festkörper*, Springer-Verlag (2016), ISBN: 9783662490938.
- [57] W. Pauli, *Über das Wasserstoffspektrum vom Standpunkt der neuen Quantenmechanik*, [Z. Phys.](#) **36**, 358–361 (1926).
- [58] S. D. Hogan, *Rydberg-Stark deceleration of atoms and molecules*, [EPJ Techniques and Instrumentation](#) **3**, 1–50 (2016).
- [59] B. J. Sussman, *Five ways to the nonresonant dynamic Stark effect*, [American Journal of Physics](#) **79**, 477–484 (2011).
- [60] D. H. Kang, J. Kim, H.-R. Noh and S. K. Kim, *Observation of the ponderomotive effect in non-valence bound states of polyatomic molecular anions*, [Nature Communications](#) **12**, 7098 (2021).
- [61] L. Jönsson, *Energy shifts due to the ponderomotive potential*, [JOSA B](#) **4**, 1422–1425 (1987).
- [62] E. Jaynes and F. Cummings, *Comparison of quantum and semiclassical radiation theories with application to the beam maser*, [Proceedings of the IEEE](#) **51**, 89–109 (1963).
- [63] A. Taflove and S. Hagness, *Computational Electrodynamics: The Finite-difference Time-domain Method*, Artech House (2005), ISBN: 9781580538329.
- [64] B. Kruse, *Voll elektromagnetische Beschreibung der Nah- und Fernfelder laserangeregter Nanostrukturen*, Master’s thesis, Universität Rostock (2016).
- [65] S. Gedney, *An anisotropic perfectly matched layer-absorbing medium for the truncation of FDTD lattices*, [IEEE Trans. Antennas Propagat.](#) **44**, 1630–1639 (1996).
- [66] H. Lorentz, *The motion of electrons in metallic bodies I*, **7**, 438–453 (1905).
- [67] G. A. Reider, *Photonik*, Springer Vienna (2012), ISBN: 978-3-7091-1521-3.
- [68] A. D. Rakić, A. B. Djurisić, J. M. Elazar and M. L. Majewski, *Optical properties of metallic films for vertical-cavity optoelectronic devices*, [Appl. Opt.](#) **37**, 5271 (1998).
- [69] A. Lucas, J. Vigneron, S. Donnelly and J. Rife, *Theoretical interpretation of the vacuum ultraviolet reflectance of liquid helium and of the absorption spectra of helium microbubbles in aluminum*, [Physical Review B](#) **28**, 2485 (1983).

- [70] C. Surko, G. Dick, F. Reif and W. Walker, *Spectroscopic study of liquid helium in the vacuum ultraviolet*, [Physical Review Letters](#) **23**, 842 (1969).
- [71] C. Varin, G. Bart, T. Fennel and T. Brabec, *Nonlinear Lorentz model for the description of nonlinear optical dispersion in nanophotonics simulations*, [Optical Materials Express](#) **9**, 771–778 (2019).
- [72] J. J. Sakurai, *Modern quantum mechanics*, Addison-Wesley Pub. Co. (1994), ISBN: 978-0-201-53929-5.
- [73] H. Bruus and K. Flensberg, *Many-Body Quantum Theory in Condensed Matter Physics: An Introduction*, OUP Oxford (2004), ISBN: 9780191057472.
- [74] H.-P. Breuer and F. Petruccione, *The theory of open quantum systems*, Oxford University Press, USA (2007), ISBN: 9780199213900.
- [75] J. B. Schneider, *Understanding the Finite-Difference Time-Domain Method*, [www.eecs.wsu.edu/~schneidj/ufdtd](http://www.eecs.wsu.edu/~schneidj/ufdtd) , (2010).
- [76] E. Süli and D. Mayers, *An Introduction to Numerical Analysis*, Cambridge University Press (2003), ISBN: 9780521007948.
- [77] M. Born, *Zur Quantenmechanik der Stoßvorgänge*, [Zeitschrift für Physik](#) **38**, 803–827 (1926).
- [78] H. Föll, *Electronic Materials*, [Lecture Hyperscript](#) , (2019).
- [79] R. J. Clausius, *Die mechanische Wärmetheorie: Die mechanische Behandlung der Electricität*, Vieweg (1879), ISBN: 9783663198918.
- [80] A. Weiss, *Oscillator strengths for the helium isoelectronic sequence*, [Journal of Research of the National Bureau of Standards. Section A, Physics and Chemistry](#) **71**, 163 (1967).
- [81] D. R. Bates and A. Damgaard, *The calculation of the absolute strengths of spectral lines*, [Philosophical Transactions of the Royal Society of London. Series A, Mathematical and Physical Sciences](#) **242**, 101–122 (1949).
- [82] N. B. Delone and V. P. Krainov, *AC Stark shift of atomic energy levels*, [Physics-Uspexhi](#) **42**, 669 (1999).
- [83] A.-P. Jauho and K. Johnsen, *Dynamical franz-keldysh effect*, [Physical review letters](#) **76**, 4576 (1996).
- [84] C. Ott, A. Kaldun, P. Raith, K. Meyer, M. Laux, J. Evers, C. H. Keitel, C. H. Greene and T. Pfeifer, *Lorentz meets Fano in spectral line shapes: a universal phase and its laser control*, [Science](#) **340**, 716–720 (2013).
- [85] J. E. Sansonetti and W. C. Martin, *Handbook of basic atomic spectroscopic data*, [Journal of physical and chemical reference data](#) **34**, 1559–2259 (2005).

- [86] M. Mudrich, A. C. LaForge, A. Ciavardini, P. O’Keeffe, C. Callegari, M. Coreno, A. Demidovich, M. Devetta, M. D. Fraia, M. Drabbels, P. Finetti, O. Gessner, C. Grazioli, A. Hernando, D. M. Neumark, Y. Ovcharenko, P. Piseri, O. Plekan, K. C. Prince, R. Richter, M. P. Ziemkiewicz, T. Möller, J. Eloranta, M. Pi, M. Barranco and F. Stienkemeier, *Ultrafast relaxation of photoexcited superfluid He nanodroplets*, [Nature Communications](#) **11**, (2020).
- [87] M. V. Ammosov, N. B. Delone and V. P. Krainov, *Tunnel ionization of complex atoms and of atomic ions in an alternating electromagnetic field*, [Soviet Journal of Experimental and Theoretical Physics](#) **64**, 1191 (1986).
- [88] P. Auger, *Sur l’effet photoélectrique composé*, [Journal de Physique et le Radium](#) **6**, 205–208 (1925).
- [89] J. D. Asmussen, R. Michiels, U. Bangert, N. Sisourat, M. Binz, L. Bruder, M. Danailov, M. D. Fraia, R. Feifel, L. Giannessi, O. Plekan, K. C. Prince, R. J. Squibb, D. Uhl, A. Wituschek, M. Zangrando, C. Callegari, F. Stienkemeier and M. Mudrich, *Time-Resolved Ultrafast Interatomic Coulombic Decay in Superexcited Sodium-Doped Helium Nanodroplets*, [The Journal of Physical Chemistry Letters](#) **13**, 4470–4478 (2022).
- [90] T. Jahnke, U. Hergenhahn, B. Winter, R. Dörner, U. Fröhling, P. V. Demekhin, K. Gokhberg, L. S. Cederbaum, A. Ehresmann, A. Knie and A. Dreuw, *Interatomic and Intermolecular Coulombic Decay*, [Chemical Reviews](#) **120**, 11295–11369 (2020).
- [91] B. Schütte, M. Arbeiter, T. Fennel, M. J. Vrakking and A. Rouzée, *Rare-gas clusters in intense extreme-ultraviolet pulses from a high-order harmonic source*, [Physical review letters](#) **112**, 073003 (2014).
- [92] F. Frassetto, A. Trabattoni, S. Anumula, G. Sansone, F. Calegari, M. Nisoli and L. Poletto, *High-throughput beamline for attosecond pulses based on toroidal mirrors with microfocusing capabilities*, [Review of Scientific Instruments](#) **85**, (2014).
- [93] R. R. Gattass and E. Mazur, *Femtosecond laser micromachining in transparent materials*, [Nat. Photon.](#) **2**, 219–225 (2008).
- [94] F. J. Furch, W. D. Engel, T. Witting, A. Perez-Leija, M. J. Vrakking and A. Mermillod-Blondin, *Single-step fabrication of surface waveguides in fused silica with few-cycle laser pulses*, [Optics Letters](#) **44**, 4267–4270 (2019).
- [95] K. Sugioka and Y. Cheng, *Ultrafast lasers—reliable tools for advanced materials processing*, [Light: Science & Applications](#) **3**, e149–e149 (2014).
- [96] A. Sommer, E. Bothschafter, S. Sato, C. Jakubeit, T. Latka, O. Razskazovskaya, H. Fattahi, M. Jobst, W. Schweinberger, V. Shirvanyan et al., *Attosecond nonlinear polarization and light–matter energy transfer in solids*, [Nature](#) **534**, 86–90 (2016).
- [97] A. McPherson, G. Gibson, H. Jara, U. Johann, T. S. Luk, I. McIntyre, K. Boyer and C. K. Rhodes, *Studies of multiphoton production of vacuum-ultraviolet radi-*

- ation in the rare gases*, [JOSA B](#) **4**, 595–601 (1987).
- [98] M. Ferray, A. L’Huillier, X. Li, L. Lompre, G. Mainfray and C. Manus, *Multiple-harmonic conversion of 1064 nm radiation in rare gases*, [Journal of Physics B: Atomic, Molecular and Optical Physics](#) **21**, L31 (1988).
- [99] P. B. Corkum, *Plasma perspective on strong field multiphoton ionization*, [Physical review letters](#) **71**, 1994 (1993).
- [100] G. Vampa, T. Hammond, N. Thiré, B. Schmidt, F. Légaré, C. McDonald, T. Brabec and P. Corkum, *Linking high harmonics from gases and solids*, [Nature](#) **522**, 462 (2015).
- [101] Z. Wang, H. Park, Y. H. Lai, J. Xu, C. I. Baga, F. Yang, P. Agostini and L. F. DiMauro, *The roles of photo-carrier doping and driving wavelength in high harmonic generation from a semiconductor*, [Nature communications](#) **8**, 1686 (2017).
- [102] S. Ghimire, A. D. DiChiara, E. Sistrunk, P. Agostini, L. F. DiMauro and D. A. Reis, *Observation of high-order harmonic generation in a bulk crystal*, [Nat. Phys.](#) **7**, 138 (2011).
- [103] F. Brunel, *Not-so-resonant, resonant absorption*, [Phys. Rev. Lett.](#) **59**, 52–55 (1987).
- [104] F. Quéré, C. Thaury, P. Monot, S. Dobosz, P. Martin, J.-P. Geindre and P. Audebert, *Coherent wake emission of high-order harmonics from overdense plasmas*, [Physical review letters](#) **96**, 125004 (2006).
- [105] L. Sudrie, A. Couairon, M. Franco, B. Lamouroux, B. Prade, S. Tzortzakis and A. Mysyrowicz, *Femtosecond laser-induced damage and filamentary propagation in fused silica*, [Physical Review Letters](#) **89**, 186601 (2002).
- [106] M. Geissler, G. Tempea, A. Scrinzi, M. Schnürer, F. Krausz and T. Brabec, *Light propagation in field-ionizing media: extreme nonlinear optics*, [Physical review letters](#) **83**, 2930 (1999).
- [107] G. Agrawal, *Nonlinear Fiber Optics*, Academic Press (2013), ISBN: 978-0-12-397023-7.
- [108] M. Arbeiter, *Mikroskopische Beschreibung der ultraschnellen Anregungs- und Relaxationsdynamik von Edelgasclustern in intensiven VUV-, XUV- und Röntgenlaserpulsen*, PhD thesis, [Universität Rostock](#) (2015).
- [109] T. Brabec, *Strong Field Laser Physics*, Springer, New York (2008), ISBN: 978-0-387-34755-4.
- [110] U. Saalman, C. Siedschlag and J. M. Rost, *Mechanisms of cluster ionization in strong laser pulses*, [J. Phys. B](#) **39**, R39–R77 (2006).

- [111] T. Fennel, K.-H. Meiwes-Broer, J. Tiggesbäumker, P.-G. Reinhard, P. M. Dinh and E. Suraud, *Laser-driven nonlinear cluster dynamics*, [Rev. Mod. Phys. \*\*82\*\*, 1793–1842 \(2010\)](#).
- [112] S. Ghimire, G. Ndabashimiye, A. D. DiChiara, E. Sistrunk, M. I. Stockman, P. Agostini, L. F. DiMauro and D. A. Reis, *Strong-field and attosecond physics in solids*, [J. Phys. B \*\*47\*\*, 204030 \(2014\)](#).
- [113] E. M. Snyder, S. A. Buzza and A. W. Castleman, Jr., *Intense Field-Matter Interactions: Multiple Ionization of Clusters*, [Phys. Rev. Lett. \*\*77\*\*, 3347–3350 \(1996\)](#).
- [114] T. Ditmire, J. W. G. Tisch, E. Springate, M. B. Mason, N. Hay, R. A. Smith, J. Marangos and M. H. R. Hutchinson, *High-energy ions produced in explosions of superheated atomic clusters*, [Nature \(London\) \*\*386\*\*, 54–56 \(1997\)](#).
- [115] R. Rajeev, T. Madhu Trivikram, K. P. M. Rishad, V. Narayanan, E. Krishnakumar and M. Krishnamurthy, *A compact laser-driven plasma accelerator for megaelectronvolt-energy neutral atoms*, [Nat. Phys. \*\*9\*\*, 185–190 \(2013\)](#).
- [116] Y. L. Shao, T. Ditmire, J. W. G. Tisch, E. Springate, J. P. Marangos and M. H. R. Hutchinson, *Multi-keV Electron Generation in the Interaction of Intense Laser Pulses with Xe Clusters*, [Phys. Rev. Lett. \*\*77\*\*, 3343–3346 \(1996\)](#).
- [117] B. Schütte, C. Peltz, D. R. Austin, C. Strüber, P. Ye, A. Rouzée, M. J. J. Vrakking, N. Golubev, A. I. Kuleff, T. Fennel and J. P. Marangos, *Low-Energy Electron Emission in the Strong-Field Ionization of Rare Gas Clusters*, [Phys. Rev. Lett. \*\*121\*\*, 063202 \(2018\)](#).
- [118] A. McPherson, B. Thompson, A. Borisov, K. Boyer and C. Rhodes, *Multiphoton-induced X-ray emission at 4-5 keV from Xe atoms with multiple core vacancies*, [Nature \(London\) \*\*370\*\*, 631–634 \(1994\)](#).
- [119] T. Ditmire, R. A. Smith, J. W. G. Tisch and M. H. R. Hutchinson, *High Intensity Laser Absorption by Gases of Atomic Clusters*, [Phys. Rev. Lett. \*\*78\*\*, 3121–3124 \(1997\)](#).
- [120] T. D. Donnelly, T. Ditmire, K. Neuman, M. D. Perry and R. W. Falcone, *High-Order Harmonic Generation in Atom Clusters*, [Phys. Rev. Lett. \*\*76\*\*, 2472–2475 \(1996\)](#).
- [121] D. Faccialà, S. Pabst, B. D. Bruner, A. G. Ciriolo, S. De Silvestri, M. Devetta, M. Negro, H. Soifer, S. Stagira, N. Dudovich and C. Vozzi, *Probe of Multielectron Dynamics in Xenon by Caustics in High-Order Harmonic Generation*, [Phys. Rev. Lett. \*\*117\*\*, 093902 \(2016\)](#).
- [122] B. C. Stuart, M. D. Feit, A. M. Rubenchik, B. W. Shore and M. D. Perry, *Laser-Induced Damage in Dielectrics with Nanosecond to Subpicosecond Pulses*, [Phys. Rev. Lett. \*\*74\*\*, 2248–2251 \(1995\)](#).

- [123] C. Rose-Petruck, K. J. Schafer, K. R. Wilson and C. P. J. Barty, *Ultrafast electron dynamics and inner-shell ionization in laser driven clusters*, *Phys. Rev. A* **55**, 1182–1190 (1997).
- [124] S. X. Hu and Z. Z. Xu, *Dynamics of an intense laser-driven multiwell system: A model of ionized clusters*, *Phys. Rev. A* **56**, 3916–3922 (1997).
- [125] M. Lenzner, J. Krüger, S. Sartania, Z. Cheng, C. Spielmann, G. Mourou, W. Kautek and F. Krausz, *Femtosecond Optical Breakdown in Dielectrics*, *Phys. Rev. Lett.* **80**, 4076–4079 (1998).
- [126] C. Siedschlag and J. M. Rost, *Electron Release of Rare-Gas Atomic Clusters under an Intense Laser Pulse*, *Phys. Rev. Lett.* **89**, 173401 (2002).
- [127] L. N. Gaier, M. Lein, M. I. Stockman, P. L. Knight, P. B. Corkum, M. Y. Ivanov and G. L. Yudin, *Ultrafast multiphoton forest fires and fractals in clusters and dielectrics*, *J. Phys. B* **37**, L57–L67 (2004).
- [128] P. P. Rajeev, M. Gertsvolf, P. B. Corkum and D. M. Rayner, *Field Dependent Avalanche Ionization Rates in Dielectrics*, *Phys. Rev. Lett.* **102**, 083001 (2009).
- [129] B. Schütte, M. Arbeiter, A. Mermillod-Blondin, M. J. J. Vrakking, A. Rouzée and T. Fennel, *Ionization Avalanching in Clusters Ignited by Extreme-Ultraviolet Driven Seed Electrons*, *Phys. Rev. Lett.* **116**, 033001 (2016).
- [130] B. Schütte, M. Arbeiter, T. Fennel, M. J. J. Vrakking and A. Rouzée, *Rare-Gas Clusters in Intense Extreme-Ultraviolet Pulses from a High-Order Harmonic Source*, *Phys. Rev. Lett.* **112**, 073003 (2014).
- [131] B. Schütte, F. Campi, M. Arbeiter, T. Fennel, M. J. J. Vrakking and A. Rouzée, *Tracing Electron-Ion Recombination in Nanoplasmas Produced by Extreme-Ultraviolet Irradiation of Rare-Gas Clusters*, *Phys. Rev. Lett.* **112**, 253401 (2014).
- [132] A. T. J. B. Eppink and D. H. Parker, *Velocity map imaging of ions and electrons using electrostatic lenses: Application in photoelectron and photofragment ion imaging of molecular oxygen*, *Review of Scientific Instruments* **68**, 3477–3484 (1997).
- [133] O. F. Hagena and W. Obert, *Cluster Formation in Expanding Supersonic Jets: Effect of Pressure, Temperature, Nozzle Size, and Test Gas*, *J. Chem. Phys.* **56**, 1793–1802 (1972).
- [134] L. Verlet, *Computer" experiments" on classical fluids. I. Thermodynamical properties of Lennard-Jones molecules*, *Physical review* **159**, 98 (1967).
- [135] J. E. Lennard-Jones, *Cohesion*, *Proceedings of the Physical Society* **43**, 461 (1931).
- [136] W. J. Veigele, *Photon cross sections from 0.1 keV to 1 MeV for elements Z= 1 to Z= 94*, *Atomic Data and Nuclear Data Tables* **5**, 51–111 (1973).

- [137] D. Verner, D. Yakovlev, I. Band and M. Trzhaskovskaya, *Subshell photoionization cross sections and ionization energies of atoms and ions from He to Zn*, *Atomic Data and Nuclear Data Tables* **55**, 233–280 (1993).
- [138] A. Ankudinov, S. Zabinsky and J. Rehr, *Single configuration Dirac-Fock atom code*, *Computer physics communications* **98**, 359–364 (1996).
- [139] W. Lotz, *An empirical formula for the electron-impact ionization cross-section*, *Zeitschrift für Physik* **206**, 205–211 (1967).
- [140] W. Lotz, *Electron-impact ionization cross-sections for atoms up to  $Z=108$* , *Zeitschrift für Physik A Hadrons and nuclei* **232**, 101–107 (1970).
- [141] T. Fennel, L. Ramunno and T. Brabec, *Highly Charged Ions from Laser-Cluster Interactions: Local-Field-Enhanced Impact Ionization and Frustrated Electron-Ion Recombination*, *Phys. Rev. Lett.* **99**, 233401 (2007).
- [142] M. Arbeiter, C. Peltz and T. Fennel, *Electron-relocalization dynamics in xenon clusters in intense soft-x-ray fields*, *Phys. Rev. A* **89**, 043428 (2014).
- [143] C. Bostedt, H. Thomas, M. Hoener, E. Eremina, T. Fennel, K.-H. Meiwes-Broer, H. Wabnitz, M. Kuhlmann, E. Plönjes, K. Tiedtke, R. Treusch, J. Feldhaus, A. R. B. de Castro and T. Möller, *Multistep Ionization of Argon Clusters in Intense Femtosecond Extreme Ultraviolet Pulses*, *Phys. Rev. Lett.* **100**, 133401 (2008).
- [144] D. Komar, L. Kazak, M. Almassarani, K.-H. Meiwes-Broer and J. Tiggesbäumker, *Highly Charged Rydberg Ions from the Coulomb Explosion of Clusters*, *Phys. Rev. Lett.* **120**, 133207 (2018).
- [145] A. Kramida, Yu. Ralchenko, J. Reader and NIST ASD Team, *NIST Atomic Spectra Database (version 5.10)*, Available: <https://physics.nist.gov/asd> [Thu Oct 12 2023]. National Institute of Standards and Technology, Gaithersburg, MD. , (2022).
- [146] T. Ditmire, T. Donnelly, R. W. Falcone and M. D. Perry, *Strong X-Ray Emission from High-Temperature Plasmas Produced by Intense Irradiation of Clusters*, *Phys. Rev. Lett.* **75**, 3122–3125 (1995).
- [147] T. Fennel, T. Döppner, J. Passig, C. H. Schaal, J. Tiggesbäumker and K.-H. Meiwes-Broer, *Plasmon-Enhanced Electron Acceleration in Intense Laser Metal-Cluster Interactions*, *Phys. Rev. Lett.* **98**, 143401 (2007).
- [148] M. Arbeiter and T. Fennel, *Ionization heating in rare-gas clusters under intense XUV laser pulses*, *Physical Review A* **82**, 013201 (2010).
- [149] C. Varin, C. Peltz, T. Brabec and T. Fennel, *Attosecond plasma wave dynamics in laser-driven cluster nanoplasmas*, *Physical review letters* **108**, 175007 (2012).

- [150] W. Nolting, *Theoretical Physics 3, Electrodynamics*, Springer (2016), ISBN: [978-3-319-40168-3](#).



# Academic Curriculum Vitae

Not included in the online version.



# Statement of Authorship

According to §4 of the doctoral regulations of the Faculty of Mathematics and Natural Sciences of the University of Rostock:

I make the following statement:

1. The opportunity for the present doctoral project has not been commercially arranged for me. In particular, I have not engaged the services of any organization that seeks supervisors for the preparation of dissertations in return for payment, or that performs for me, in whole or in part, the duties incumbent upon me with regard to examination performance.
2. I hereby declare in lieu of an oath that I have written this thesis independently and without outside help. For this purpose, I have not used any aids and sources other than those indicated by me. Passages taken verbatim and in terms of content from the works are marked accordingly. marked as such.

Rostock, 19. February 2024



# Selbständigkeitserklärung

Gemäß §4 der Promotionsordnung der Mathematisch-Naturwissenschaftlichen Fakultät der Universität Rostock:

Ich gebe folgende Erklärung ab:

1. Die Gelegenheit zum vorliegenden Promotionsvorhaben ist mir nicht kommerziell vermittelt worden. Insbesondere habe ich keine Organisation eingeschaltet, die gegen Entgelt Betreuerinnen/Betreuer für die Anfertigung von Dissertationen sucht oder die mir obliegenden Pflichten hinsichtlich der Prüfungsleistungen für mich ganz oder teilweise erledigt.
2. Ich versichere hiermit an Eides statt, dass ich die vorliegende Arbeit selbstständig angefertigt und ohne fremde Hilfe verfasst habe. Dazu habe ich keine außer den von mir angegebenen Hilfsmitteln und Quellen verwendet und die den benutzten Werken inhaltlich und wörtlich entnommenen Stellen habe ich als solche kenntlich gemacht.

Rostock, 19. Februar 2024



# Acknowledgement – Danksagung

An dieser Stelle möchte ich zunächst meinem Doktorvater Thomas Fennel für die Möglichkeit danken, dass ich so aktuelle und spannende Themen in meiner Promotionszeit bearbeiten konnte. Außerdem hatte ich dadurch die Möglichkeit, meine Forschung auf vielen Konferenzen und Workshops vorzustellen und damit zahlreiche Kontakte zu anderen Wissenschaftler\*innen knüpfen zu können.

Hervorzuheben sind dabei auch die vielen Kooperationen mit Experimentalphysiker\*innen, sei es die Zusammenarbeit mit Alexandre Mermillod-Blondin und Peter Jürgens oder mit der Arbeitsgruppe von Daniela Rupp. Besonders für die Möglichkeit, an FELs bei zahlreichen Strahlzeiten als Theoretiker mitzuarbeiten, bin ich sehr dankbar, weil an diesen Großanlagen Neues zu entdecken, ist genau das, was es ausmacht, Physiker zu sein.

Besonderer Dank gilt Christian Peltz, der mir sehr viel beigebracht hat und immer besonders kritisch war, dadurch aber auch besonders hilfreich. Außerdem möchte ich meinem langjährigen Kollegen Benjamin Liewehr für die schönen Stunden zusammen im Büro danken, die gute Zusammenarbeit und dafür, dass er ein wandelndes Physiklexikon ist. Natürlich möchte ich auch der gesamten Arbeitsgruppe Starkfeld-Nanophysik für die angenehme Atmosphäre und gegenseitige Unterstützung danken.

Abschließend möchte ich mich bei meiner Familie für die fortwährende Unterstützung bedanken und insbesondere bei meiner Ehefrau und meiner Tochter, die mir die dringend nötige Motivation für den Endspurt in der Promotionszeit gegeben haben.